A&A 643, A83 (2020)
https://doi.org/10.1051/0004-6361/201936726

Astronomy & Astrophysics

The *Gaia*-ESO Survey: Spectroscopic-asteroseismic analysis of K2 stars in *Gaia*-ESO[⋆,⋆⋆]

The K2 Galactic Caps Project

C. C. Worley[1], P. Jofré[2], B. Rendle[3], A. Miglio[3], L. Magrini[4], D. Feuillet[5,12], A. Gavel[6], R. Smiljanic[7], K. Lind[5,6,21], A. Korn[6], G. Gilmore[1], S. Randich[4], A. Hourihane[1], A. Gonneau[1], P. Francois[8], J. Lewis[1], G. Sacco[4], A. Bragaglia[11], U. Heiter[6], S. Feltzing[12], T. Bensby[12], M. Irwin[1], E. Gonzalez Solares[1], D. Murphy[1], A. Bayo[19,22], L. Sbordone[17], T. Zwitter[18], A. C. Lanzafame[10], N. Walton[1], S. Zaggia[9], E. J. Alfaro[13], L. Morbidelli[4], S. Sousa[14], L. Monaco[15], G. Carraro[16], and C. Lardo[20]

(Affiliations can be found after the references)

Received 18 September 2019 / Accepted 18 June 2020

ABSTRACT

Context. The extensive stellar spectroscopic datasets that are available for studies in Galactic Archeaology thanks to, for example, the *Gaia*-ESO Survey, now benefit from having a significant number of targets that overlap with asteroseismology projects such as *Kepler*, K2, and CoRoT. Combining the measurements from spectroscopy and asteroseismology allows us to attain greater accuracy with regard to the stellar parameters needed to characterise the stellar populations of the Milky Way.

Aims. The aim of this *Gaia*-ESO Survey special project is to produce a catalogue of self-consistent stellar parameters by combining measurements from high-resolution spectroscopy and precision asteroseismology.

Methods. We carried out an iterative analysis of 90 K2@*Gaia*-ESO red giants. The spectroscopic values of $T_{\rm eff}$ were used as input in the seismic analysis to obtain $\log g$ values. The seismic estimates of $\log g$ were then used to re-determine the spectroscopic values of $T_{\rm eff}$ and [Fe/H]. Only one iteration was required to obtain parameters that are in good agreement for both methods and, thus, to obtain the final stellar parameters. A detailed analysis of outliers was carried out to ensure a robust determination of the parameters. The results were then combined with *Gaia* DR2 data to compare the seismic $\log g$ with a parallax-based $\log g$ and to investigate instances of variations in the velocity and possible binaries within the dataset.

Results. This analysis produced a high-quality catalogue of stellar parameters for 90 red giant stars from K2@*Gaia*-ESO that were determined through iterations between spectroscopy and asteroseismology. We compared the seismic gravities with those based on *Gaia* parallaxes to find an offset which is similar to other studies that have used asteroseismology. Our catalogue also includes spectroscopic chemical abundances and radial velocities, as well as indicators for possible binary detections.

Key words. catalogs – stars: fundamental parameters – stars: abundances – techniques: spectroscopic – asteroseismology

1. Introduction

The characterisation of the Milky Way stellar populations in studies of Galactic Archaeology has been greatly advanced with the recently acquired wealth of high-quality spectroscopic data that are now available for hundreds of thousands of stars in our Galaxy. The recent Data Release 2 for the European Space Agency (ESA) space mission, *Gaia*, has led to the publication of highly accurate astrometry for over a billion stars in the Milky Way (Gaia Collaboration 2018).

In anticipation of this astrometric mecca, a suite of stellar spectroscopic surveys of high-resolution, such as *Gaia*-ESO (Gilmore et al. 2012), APOGEE (Majewski et al. 2017), and GALAH (De Silva et al. 2015) were created, initiating a new era of large databases containing the spectra and scientific measurements for hundreds of thousands of stars. The next wave of surveys, such as WEAVE (Dalton et al. 2012), 4MOST (de Jong et al. 2019), MOONS (Cirasuolo & MOONS Consortium 2016), and MSE (Szeto et al. 2018) will expand the coverage of these databases into the millions.

However, the robustness of the stellar parameters determined for these large spectroscopic datasets depends, in particular, on the accuracy of the parameters of just a few small samples of reference stars (see discussion in e.g. Jofré et al. 2019). A stellar reference set commonly used for the validation and verification of automated stellar parameterisation pipelines is the *Gaia* FGK Benchmark Stars (Jofré et al. 2014; Heiter et al. 2015). These are very bright stars but they number only 36 (Jofré et al. 2018, for the latest list) and so, they sparsely sample the FGK stellar parameter space. Reference sets are also drawn from stellar spectral libraries, in particular the ELODIE library (Prugniel & Soubiran 2001), compilations of high quality (but inhomogeneous) literature values such as PASTEL (Soubiran et al. 2016), and stars that are well-known members of open clusters or globular clusters.

These relatively small reference sets are being used to define the parameter scale zero-point upon which the large scale analyses are then based (e.g., Pancino et al. 2017; Kunder et al. 2017). They are therefore crucial for determining the accurate absolute

⋆ Full Tables B.1 and B.2 are only available at the CDS via anonymous ftp to cdsarc.u-strasbg.fr (130.79.128.5) or via http://cdsarc.u-strasbg.fr/viz-bin/cat/J/A+A/643/A83

⋆⋆ Based on observations collected at the European Southern Observatory under ESO programme 188.B-3002.

values of the reported stellar parameters (effective temperature $T_{\rm eff}$, surface gravity $\log g$, metallicity [Fe/H], microturbulence ξ) for these large-scale surveys. They are also essential for effective comparison of the survey datasets with stellar and galactic evolution models as this is key to making a straightforward comparison and combination of data from multiple surveys analysed by different pipelines. In the future, parameters for these reference sets derived within *Gaia*-ESO and other surveys can be compared to results drawn from more sophisticated models of stellar atmospheres that may include advances in non-LTE, 3D, and dynamical atmospheres, for example.

However, the relatively small number of reference stars stands as a problem given the required stellar parameter space is not well-sampled for a comprehensive analysis by the automated pipelines. Greater coverage is needed all the way from cool pre-main sequence stars to hot OB stars. New stellar reference sets of independently determined stellar parameters are required to keep up with the demands of upcoming large scale surveys. The work presented here seeks to define a new sample of reference stars generated by combining the stellar parameters of $T_{\rm eff}$ and [Fe/H] from spectroscopy with $\log g$ from asteroseismology.

Today, the availability of datasets with a wide sky coverage has resulted in many overlapping targets between research fields and presents, thus, an opportunity to make simultaneous use of the collective strengths of multiple types of analyses. This is the case here, among the thousands of targets with high-resolution and high-quality stellar spectra, where there is also asteroseismic information for some thanks to the dedicated monitoring of their oscillations by *Kepler* (Borucki et al. 2010), CoRoT (Baglin et al. 2006) and, recently, by K2 (Howell et al. 2014). These asteroseismic measurements of the interior of stars combined with the spectroscopic "exterior" measurements of the same stars and the direct measurement of the parallax of each star, are part of the unfolding revolution in Galactic Archaeology (Miglio et al. 2017). To take advantage of and further develop this multi-analysis approach, the *Gaia*-ESO Survey observed several hundreds of stars in the K2 Campaign 3 (C3) field, located towards the South Galactic pole.

The *Gaia*-ESO Survey is an ESO Large Public Spectroscopic survey designed to target over 100 000 in the key stellar populations of the Milky Way (Gilmore et al. 2012). It has made use of a large range of analysis methods and thus developed key homogenisation procedures to bring all the results together in a robust single star catalogue, the final data release of which is currently underway. *Gaia*-ESO observed stars using the medium-resolution spectrograph GIRAFFE ($R \sim 20\,000$) and the high-resolution spectrograph UVES ($R \sim 47\,000$) on the VLT.

K2 is a re-purposing of the *Kepler* satellite for which the science goals are focussed on the detection of the variations in the light curves of stars in 19 fields along the ecliptic to look for transiting exo-planets. At the time this special project began, 90 giant stars with oscillations detected by K2 were identified within the sample of *Gaia*-ESO stars observed in C3 with medium- and high- resolution spectroscopy. This sample is referred to hereafter as K2@*Gaia*-ESO.

In this paper, which is part of the series of the K2 Galactic Caps Project (see also Rendle et al. 2019, hereafter Paper I) and is, in particular, a collaboration with *Gaia*-ESO, we describe the process of obtaining accurate atmospheric parameters that are consistent with the results of asteroseismology. We use our results to explore age dependencies with abundance ratios and examine potential binary stars in our sample. This sample will further provide a good opportunity for the study of any possible offsets between standard spectroscopic parameters and future sets of parameters derived from more sophisticated models of stellar atmospheres (e.g. non-LTE, 3D, dynamical atmospheres).

In Sect. 2, we describe in more detail the data we use for this work. In Sect. 3, we describe the process we used to determine atmospheric parameters iteratively between spectroscopy and asteroseismology. In Sect. 4, we present our chemical abundance results. The comparison to $\log g$ based on *Gaia* parallaxes is presented in Sect. 5. Our findings regarding binary stars are described in Sect. 6 and the final discussion and conclusions are presented in Sect. 7.

2. The *Gaia*-ESO Survey sample of K2 stars

Targets within the K2 C3 field were prepared as part of the *Gaia*-ESO observing programme. This resulted in 496 observations that were available for analysis. The initial set of targets were observed in May and June 2016 and, thus, added into the internal Data Release (iDR) 5 data analysis cycle of *Gaia*-ESO that had begun at the start of May 2016. The rest of the fields were observed in October 2016 and are part of iDR6.

In total there were 231 targets observed using UVES 580 (blue and red arms) and 265 targets observed using the HR10 and HR21 setups of GIRAFFE. Of these, 182 UVES targets and 133 GIRAFFE targets had been included as part of the iDR5 analysis.

2.1. Cross-match to K2

The K2 C3 stars that are part of the *Gaia*-ESO survey were observed by K2 after they were observed by *Gaia*-ESO. Therefore, it was not known at the time when *Gaia*-ESO was observing them how many would ultimately have asteroseismic detections. At the start of this spectroscopic analysis, 90 of the 496 targets were identified as having K2 asteroseismic detections; 28 of these were observed with GIRAFFE, 62 were observed with UVES. It is possible that more of the full sample will have asteroseismic detections as the K2 analysis advances, but we leave this consideration to future works.

Figure 1a shows the HR diagram of the *Gaia*-ESO iDR5 FGK stars ($S/N > 30$) and the 224 K2 targets (out of 496) observed by *Gaia*-ESO that were analysed in iDR5 with this signal-to-noise ratio (S/N) cut. A PARSEC stellar track of Solar metallicity and age is also shown (Bressan et al. 2012). Figure 1b shows the final stellar parameters of the 90 K2@*Gaia*-ESO sample analysed in this work with the [Fe/H] colourmap. Details of the seismic analysis for these targets can be found in Paper I.

2.2. Preliminary spectroscopic parameters

It was important to initiate the iterations between the spectroscopic and seismic analyses from the best starting point possible in $T_{\rm eff}$. As not all of the K2@*Gaia*-ESO targets were observed in time to be included in iDR5, it was necessary to compile the rest of the *preliminary* stellar parameter set from a variety of other sources including: a photometric $T_{\rm eff}$; parameters associated with the synthetic template used in the radial velocity determination in the reduction pipelines; and parameters derived using an available *Gaia*-ESO node analysis. These values are provided for just the 90 K2@*Gaia*-ESO stars with asteroseismic detections in Table C.1 along with the *Gaia*-ESO CNAME, EPIC identifier and the instrument with which the spectrum was observed for *Gaia*-ESO.

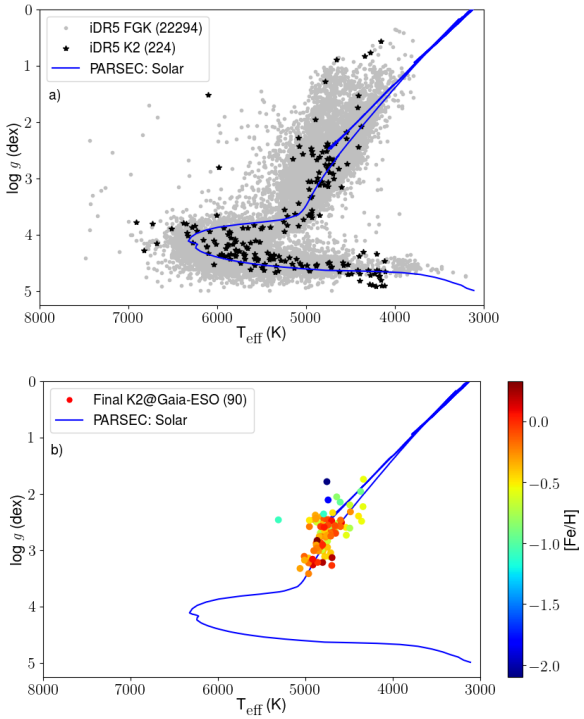

Fig. 1. *a*: HR Diagram of iDR5 FGK stars (grey points), K2 C3 stars analysed in *Gaia*-ESO iDR5 (black stars) and PARSEC Solar track. *b*: Kiel diagram of the final set of K2@*Gaia*-ESO stars for which we obtained spectroscopic parameters as analysed in this paper, with PARSEC Solar track.

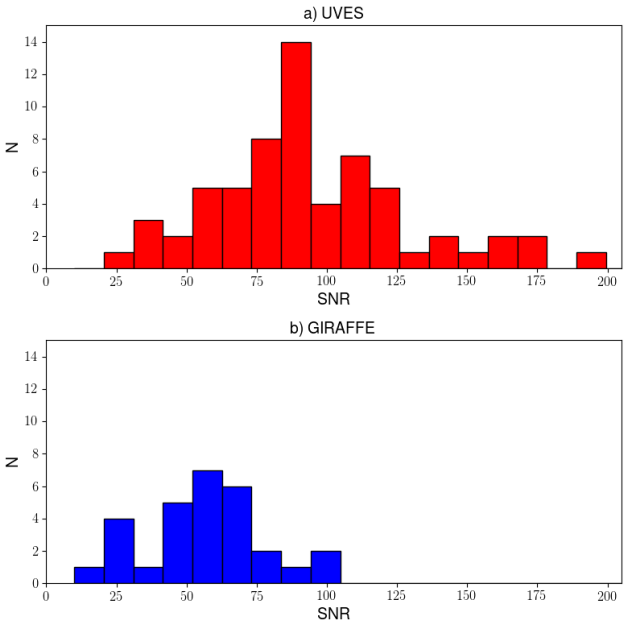

Fig. 2. S/N distribution for the K2 stars observed with (*a*) UVES and (*b*) GIRAFFE.

For both samples, the infrared flux method (IRFM) calibrations of Ramírez & Meléndez (2005) were used to estimate a photometric $T_{\rm eff}$ using the APASS V magnitude and the 2MASS Ks magnitude. The [Fe/H] from the iDR5 recommended parameters were used as input to the IRFM calibration equations where possible. Otherwise the [Fe/H] from the GIRAFFE radial velocity determination (Gilmore et al., in prep.) were used for GIRAFFE, and the [Fe/H] from the *Gaia*-ESO Nice Node iDR5 analysis (see Smiljanic et al. 2014; Worley et al. 2016, for description) were used for UVES.

2.3. Outliers

The sample was then investigated for outliers and discrepancies within this range of parameters, which are discussed below.

2.3.1. Signal-to-noise

The signal-to-noise ratio (S/N) is a good indicator of the quality of the observed spectra. The distribution of the S/N for the UVES and GIRAFFE samples for the 90 K2 stars are shown in Fig. 2. The majority of the spectra have S/N above 50. Those spectra with the lowest S/N may potentially suffer from insufficient signal causing deviations in the derived stellar parameters. This is considered in Sect. 3.4 in light of the stellar parameters determined by the two analysis teams.

2.3.2. IRFM not applicable

There were three cases for which the magnitudes of the stars did not lie within the range of acceptable values to which the IRFM calibration relations can be applied. They are CNAMEs: 22072768−1440392, 22092416−0610474, and 22105015−1119135. The *preliminary* parameters were, however, complete for each and were thus used without an assessment against an IRFM $T_{\rm eff}$. Otherwise the median difference between the IRFM and *preliminary* $T_{\rm eff}$ is 20 ± 75 K, showing good agreement in general.

2.3.3. No iDR5 [Fe/H]

For the target with CNAME 22034179−0815421 and EPIC ID K2_206298620, no recommended [Fe/H] was reported for iDR5, although $T_{\rm eff}$ and $\log g$ were provided. The radial velocity determination provided an associated [Fe/H] of −2.55, however the $T_{\rm eff}$ associated with the radial velocity determination was greater than the iDR5 $T_{\rm eff}$ by ∼300 K and the $\log g$ was lower by ∼0.3. The IRFM $T_{\rm eff}$ was in better agreement with the iDR5 $T_{\rm eff}$. An inspection of the spectrum using iSpec (Blanco-Cuaresma et al. 2014) was carried out, based on a comparison with synthetic spectra generated at both the iDR5 parameters and at the radial velocity determination parameters. In both cases, the [Fe/H] was re-derived, obtaining −2.08 and −1.80, respectively. Based on this and the agreement with the IRFM $T_{\rm eff}$, the *preliminary* parameter estimate for this star was supplemented by [Fe/H] = −2.08 derived from the iDR5 parameters using iSpec.

Based on the *preliminary* set being complete in $T_{\rm eff}$ and in reasonable agreement with the available photometric $T_{\rm eff}$, the *preliminary* $T_{\rm eff}$ from spectroscopy were used to derive the *preliminary* $\log g$ from seismology using the seismic analysis described in Paper I carried out by the Birmingham team (hereafter referred to as BHAM).

2.4. Initial spectroscopic parameters

The set of *preliminary* $T_{\rm eff}$ and [Fe/H] compiled in Table C.1 are comprehensive but were unavoidably inconsistent in their source because not all of them were processed previously by the *Gaia*-ESO Survey. Thus, for the 90 stars found to have asteroseismic

detections an initial analysis using just iSpec was carried out solely on these stars. For this analysis, the surface gravity was fixed to the *preliminary* seismic $\log g$ that was based on the *preliminary* $T_{\rm eff}$. This now homogeneous set from iSpec was used to explore any further inconsistencies between the iSpec spectroscopic and *preliminary* seismic results and fill in missing values as in Sect. 2.3. The iSpec spectroscopic, $T_{\rm eff}$, was used to determine an associated seismic $\log g$. These comprise the *initial* set of parameters used as the starting point for the following iterative process between the two *Gaia*-ESO spectroscopic analyses and the seismic analysis. These *initial* parameters are listed in Table C.1.

3. Iterative determination of parameters

The goal of this process was to iterate between the spectroscopic effective temperature ($T_{\rm eff,Spec}$) and the seismic surface gravity ($\log g_{\rm Seis}$) to converge on a final set of independently-confirmed stellar parameters. The seismic $\log g$ was determined considering the parameters determined from seismology, namely the frequency of maximum power ($\nu_{\rm max}$) from the p-mode pulsation analysis and the spectroscopic parameter, $T_{\rm eff}$. We follow the scaling relation of:

$$\log g = \log g_{\odot} + \log(\nu_{\rm max}/\nu_{\rm max,\odot}) + \frac{1}{2}\log(T_{\rm eff}/T_{\rm eff,\odot}), \quad (1)$$

as in Morel & Miglio (2012). Details of how this analysis works can be further found in Morel et al. (2014) for a sample of CoRoT targets and in Pinsonneault et al. (2018) for stars observed with *Kepler* and APOGEE. As discussed there, the seismic analysis of the p-modes is model-independent and so, the main source of uncertainty stems from the input temperature. Therefore, as the $T_{\rm eff,Spec}$ determination improves, the $\log g_{\rm Seis}$ determination also improves.

We point to the discussion of Morel et al. (2014) that a change of 100 K in $T_{\rm eff}$ only affects $\log g$ by about 0.005. Therefore, significant improvement in $\log g$ by, say, a change of the order of 0.1, requires a change in $T_{\rm eff}$ that is much larger than typical uncertainties of $T_{\rm eff}$. Nonetheless, by fixing $\log g$ to a value that is primarily only affected by $\nu_{\rm max}$ allows us to set a spectroscopic $T_{\rm eff}$ scale that is consistent with the seismic $\log(g)$ and leads to improvement in other stellar quantities such as chemical composition, masses and ultimately ages (see also discussion in Paper I).

Two *Gaia*-ESO analysis nodes, EPINARBO and Lumba (see Smiljanic et al. 2014, for further details of these and other nodes), carried out the spectroscopic analysis of the GIRAFFE and UVES spectra of the K2 stars in the iterative procedure. The analysis methods are based on equivalent widths for EPINARBO and spectrum synthesis for Lumba (see Sects. 3.2 and 3.3). Following the requirements of the *Gaia*-ESO Survey, both methods use MARCS stellar atmosphere models (Gustafsson et al. 2008) and the *Gaia*-ESO linelist (Heiter et al. 2020). These two nodes were selected because they represent two of the most widely used methods for parameter determination in stellar spectroscopy (equivalent widths and syntheses, see Jofré et al. 2019). Figure 3 illustrates the iterative process between spectroscopic and seismic parameter determinations that was followed in this analysis.

In summary, the initial spectroscopic parameters ($T_{\rm eff,iniSpec}$, $[{\rm Fe/H}]_{\rm iniSpec}$) were used to determine the initial seismic $\log g_{\rm iniSeis}$. This set of $T_{\rm eff,iniSpec}$, $[{\rm Fe/H}]_{\rm iniSpec}$ and $\log g_{\rm iniSeis}$ were given to both spectroscopic nodes. EPINARBO and Lumba were asked to fix the $\log g$ of their analysis to $\log g_{\rm iniSeis}$ and could otherwise use $T_{\rm eff,iniSpec}$ and $[{\rm Fe/H}]_{\rm iniSpec}$ as priors in the re-determination of those values if needed.

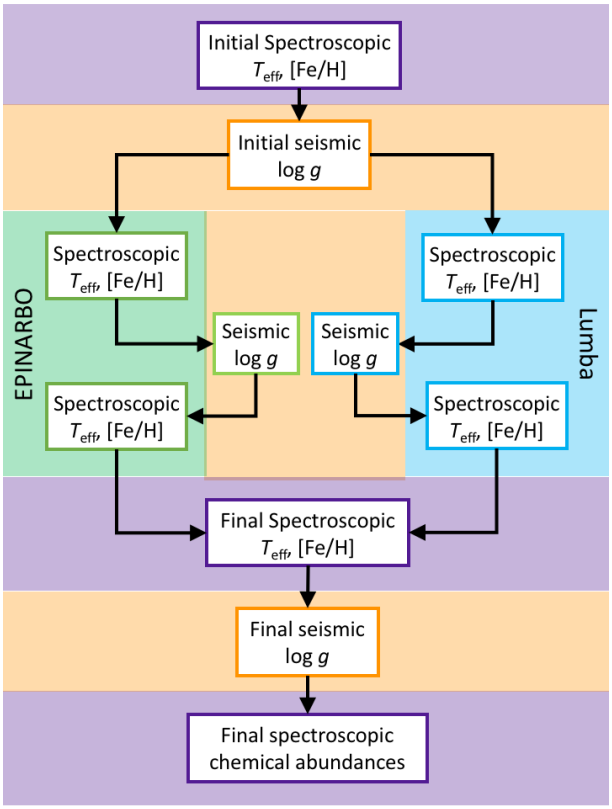

Fig. 3. Flow diagram of iterations between spectroscopic and seismic parameter determination.

EPINARBO and Lumba each then returned a new set of parameters, $T_{\rm eff,Spec1}$ and $[{\rm Fe/H}]_{\rm Spec1}$. Based on the $T_{\rm eff,Spec1}$ values, BHAM then calculated new $\log g_{\rm Seis1}$ values for each node. With their respective sets of $\log g_{\rm Seis1}$ values EPINARBO and Lumba once again determined the parameters based on the fixed $\log g_{\rm Seis1}$ to each provide $T_{\rm eff,Spec2}$ and $[{\rm Fe/H}]_{\rm Spec2}$.

The two sets of $T_{\rm eff,Spec2}$ and $[{\rm Fe/H}]_{\rm Spec2}$ were then combined to define the final set of spectroscopic parameters $T_{\rm eff,finSpec}$ and $[{\rm Fe/H}]_{\rm finSpec}$. Based on $T_{\rm eff,finSpec}$ BHAM calculated the final seismic $\log g_{\rm finSeis}$.

These three values: $T_{\rm eff,finSpec}$, $[{\rm Fe/H}]_{\rm finSpec}$, and $\log g_{\rm finSeis}$ comprise the final stellar parameters of the K2@*Gaia*-ESO sample. In the final phase EPINARBO and Lumba were then asked to derive chemical abundances for each star based on these stellar parameters.

This was the defined procedure and goal of the K2@*Gaia*-ESO special project. However the homogenisation and combination of the results into a single final set of parameters per star required a detailed investigation of individual results. This was to ensure that each result was well-understood in an informed manner, which allows for reproducibility. We note that a careful homogenisation of the different node results has been a crucial focus of the *Gaia*-ESO Survey (Hourihane et al., in prep.; Worley et al., in prep.).

3.1. Homogenisation strategy

There were six sets of $T_{\rm eff}$, six sets of [Fe/H] and four sets of $\log g$ produced in the iterative process. Within these sets are the high-resolution (UVES: 62 targets) and medium-resolution

(GIRAFFE: 28 targets) subsamples. The high- and medium-resolution results were homogenised separately, as the lower resolution and smaller wavelength range of the GIRAFFE observations required more detailed quality assessment. The individual node results and the analysis undertaken to homogenise them are explained in the subsequent sections.

3.2. EPINARBO analysis

The EPINARBO analysis measures the equivalent widths (EW) with the DOOp code (Cantat-Gaudin et al. 2014), which automatically measures equivalent widths with DAOSPEC (Stetson & Pancino 2008). It then derives the stellar parameters and abundances with FAMA (Magrini et al. 2014), which calls spectrum synthesis code MOOG (Sneden et al. 2012). The initial microturbulence parameter (ξ) was computed with the *Gaia*-ESO relation for stars with different $T_{\rm eff}$ and $\log g$ (Smiljanic et al. 2014).

For the K2@*Gaia*-ESO analysis, the surface gravity was fixed to the provided seismic value and EPINARBO iterated to converge on the equilibrium $T_{\rm eff}$, [Fe/H] and ξ. The stars for which the analysis found a lack of sufficient Fe I and Fe II lines were flagged by EPINARBO and, in particular, it was noted that the blended lines in the medium-resolution GIRAFFE spectra were not ideal for EW methods.

Figure 4 shows the progression of the EPINARBO results iteration. Figures 4a–c compare the initial parameters ($T_{\rm eff,iniSpec}$, $\log g_{\rm iniSeis}$, $[{\rm Fe/H}]_{\rm iniSpec}$) to each iterated set of parameters (red: $T_{\rm eff,Spec1}$, $\log g_{\rm Seis1}$, $[{\rm Fe/H}]_{\rm Spec1}$; blue: $T_{\rm eff,Spec2}$, $\log g_{\rm Seis2}$, $[{\rm Fe/H}]_{\rm Spec2}$) for the UVES analysis. Figures 4d–f are the same but for GIRAFFE.

The median and median absolute difference (MAD) of the difference between iteration sets for each parameter and each iteration are also shown. There is little variation from Spec1 to Spec2 for both UVES and GIRAFFE. GIRAFFE shows more scatter in the results while the UVES results seem more stable. The plots of seismic $\log g$ are included for completeness showing that any large variation in $T_{\rm eff}$ between iterations does not result in much variation in the $\log g$. This agrees with the findings of Morel et al. (2014). See Sect. 3.4 for more discussion on this.

3.3. Lumba analysis

The Lumba analysis (Gavel et al. 2020) performs spectrum synthesis using Spectroscopy Made Easy (SME: Valenti & Piskunov 1996; Piskunov & Valenti 2017). For the K2@*Gaia*-ESO analysis, the surface gravity was fixed to the provided seismic value and Lumba iterated to converge on the equilibrium $T_{\rm eff}$, [Fe/H], and ξ (Smiljanic et al. 2014).

Figure 5 shows the iterative process for the Lumba UVES and GIRAFFE analyses as for Fig. 4. There are some distinct outliers for each instrument set, however, the Lumba results are generally very stable between iterations as expected (Morel et al. 2014).

3.4. Comparison of node parameters

Within the *Gaia*-ESO Survey, all of the nodes perform a fully spectroscopic analysis of the *Gaia*-ESO spectra. While the determination of unconstrained spectroscopic $T_{\rm eff}$, $\log g$, and [Fe/H] was not the goal of this study, it is interesting to compare the unconstrained spectroscopic parameters to those determined by iteration between spectroscopy and astereoseismology. For the purposes of this paper, the unconstrained spectroscopic $T_{\rm eff}$, $\log g$, and [Fe/H] determined by each node are referred to as Spec0.

Figure 6 directly compares the EPINARBO and Lumba parameters derived for Spec0 (top row) and for the final iteration, Spec2 (bottom row), for GIRAFFE (blue), and UVES (red), respectively. Based on Figs. 4 and 5, there was little movement between iterations for each node. Therefore inspecting the final parameters (Spec2) from each node was deemed sufficient. The median and MAD for each parameter between the two nodes are also given. The greater spread of the difference in the GIRAFFE parameters compared to the UVES parameters is clearly seen. The UVES results are in good agreement between the nodes for both Spec0 and Spec2.

As stated in Sect. 3.2, EPINARBO reported that the EW method found inconsistencies in Fe I and Fe II abundances for the GIRAFFE spectra due to the blending of spectral features at that resolution and, indeed, a total of nine stars are not included at all for GIRAFFE Spec0 as the EW method did not converge on a result. The particular stars with converged results but that were flagged by EPINARBO are highlighted in all panels in Fig. 6 as data points with a yellow circle as those rejected by EPINARBO in Spec0, and data points with central white dots (GIRAFFE), or white triangles (UVES) as those rejected by EPINARBO in Spec2. The use of the EPINARBO flagged stars for assessing the quality of the results is explained in detail in Sect. 3.4.2.

For Spec0 even those that are not rejected have a wide spread, while for Spec2 the stars that are not rejected are tightly distributed and in good agreement with the Lumba results. Certainly this comparison shows that for the GIRAFFE spectra (lower resolution and smaller wavelength range that UVES) fixing the $\log g$ using astereoseismology has allowed the spectroscopic $T_{\rm eff}$ to be better constrained and, thus, there is better agreement between the methods and more of the sample is available for abundance analysis. The high-resolution and greater wavelength range of the UVES sample produces good agreement between the nodes results for both Spec0 and Spec2.

The differences in node parameters in Fig. 6 are shown against S/N. There is no obvious indication that as the S/N decreases, the differences between the node parameters increase. Indeed, for the UVES sample, the spread in the differences is fairly consistent and minimal across the S/N range for both Spec0 and Spec2. For the GIRAFFE sample, there is a large scatter generally for this smaller sample of 28 stars. As there was no obvious trend with S/N, the differences between the node parameters were used directly in the assessment of the quality of the results.

Considering the Spec2 results in particular, which are the set from which the final stellar parameters will be determined, there is, overall, an offset in [Fe/H] between the nodes for both the UVES and GIRAFFE analyses ($\Delta[{\rm Fe/H}] \simeq -0.15$). There is an offset in $T_{\rm eff}$ ($\Delta T_{\rm eff} \simeq -80$ K). This is discussed further in Sect. 3.4.7.

The $\log g$ in all cases are those from the seismic analysis, based on the respective spectroscopic $T_{\rm eff}$. There are some high discrepancies found between the nodes ($\Delta T_{\rm eff} > 500$ K, $\Delta[{\rm Fe/H}] > 0.5$) for certain stars, most particularly in the GIRAFFE analysis reflected in the high value of the MAD ($\mathrm{MAD}_{T_{\rm eff}} > 308$ K, $\mathrm{MAD}_{[{\rm Fe/H}]} > 0.15$) compared to the tighter agreement for the UVES analyses ($\mathrm{MAD}_{T_{\rm eff}} > 60$ K, $\mathrm{MAD}_{[{\rm Fe/H}]} > 0.07$). The largest disagreement in $T_{\rm eff}$ equates to a very small shift in seismic $\log g$ ($\Delta T_{\rm eff} \approx -2200$ K corresponds to $\Delta \log g \approx -0.09$).

Figure 7 shows the difference between the two sets of node results for the final seismic $\log g$ against the difference in final

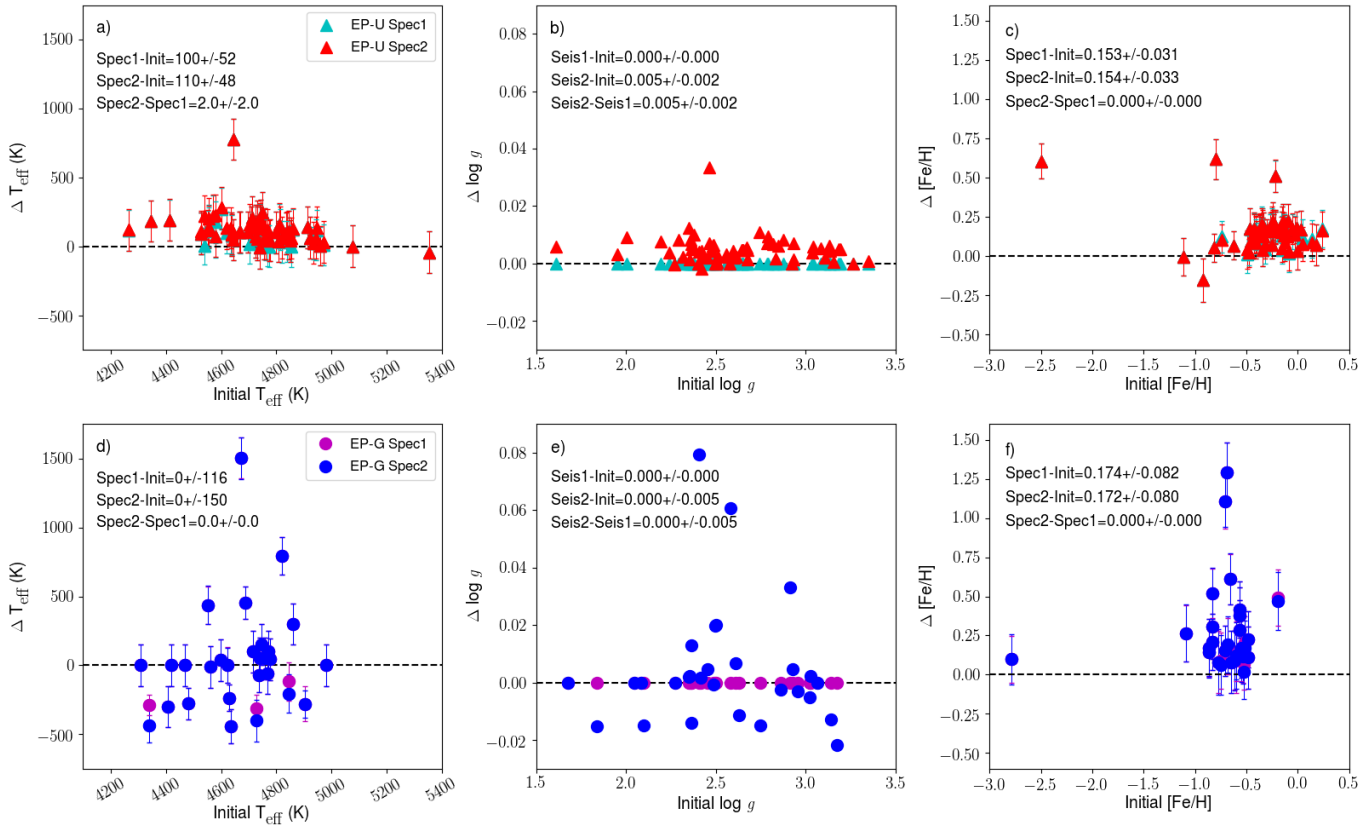

Fig. 4. Stellar parameter iterations for EPINARBO (*a–c*) UVES sample; (*d–f*) GIRAFFE sample. For $T_{\rm eff}$, $\log g$ and [Fe/H], comparison of initial parameters against Spec1 and Spec2. The median of differences and MAD values are specified.

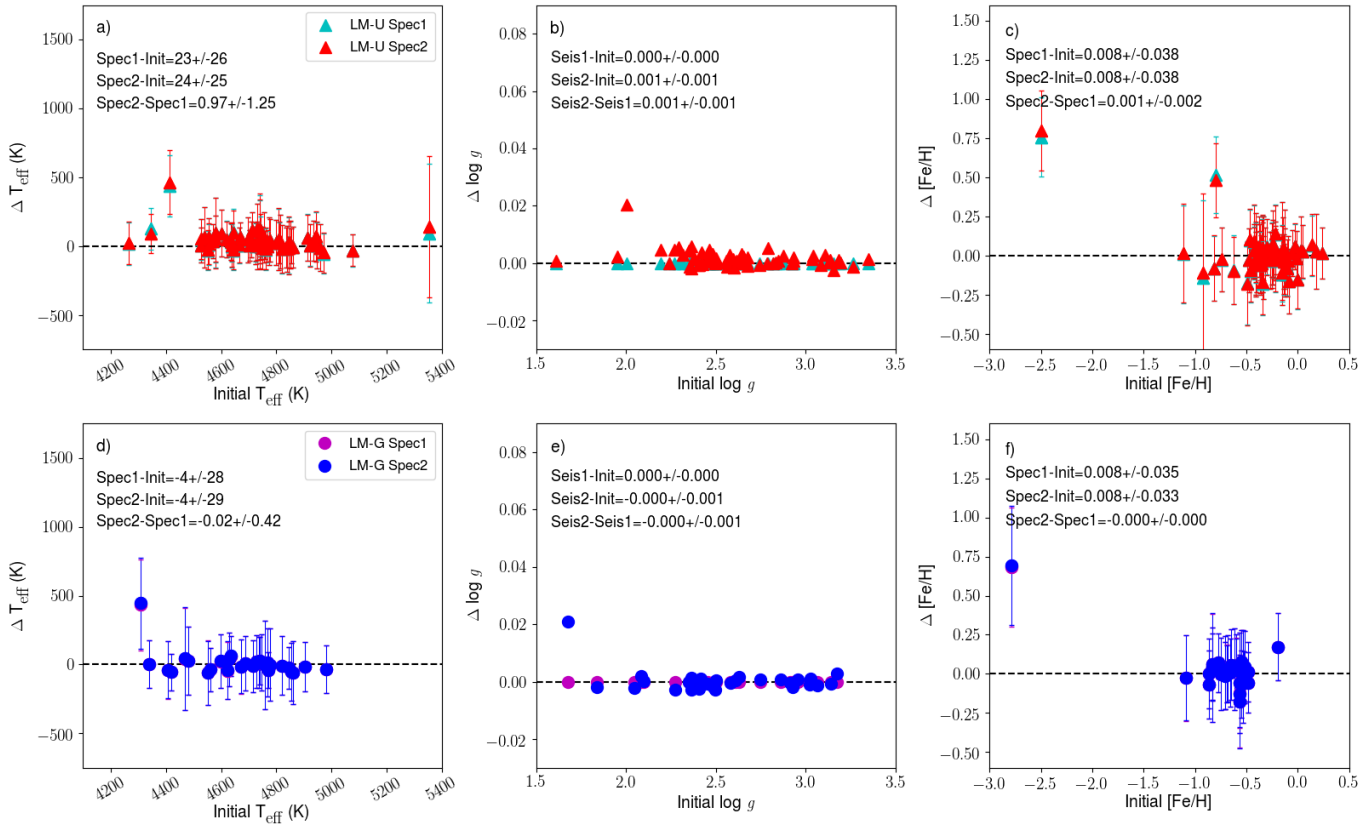

Fig. 5. Stellar parameter iterations for Lumba (*a–c*) UVES sample; (*d–f*) GIRAFFE sample. For $T_{\rm eff}$, $\log g$ and [Fe/H], comparison of initial parameters against Spec1 and Spec2. The median of differences and MAD values are specified.

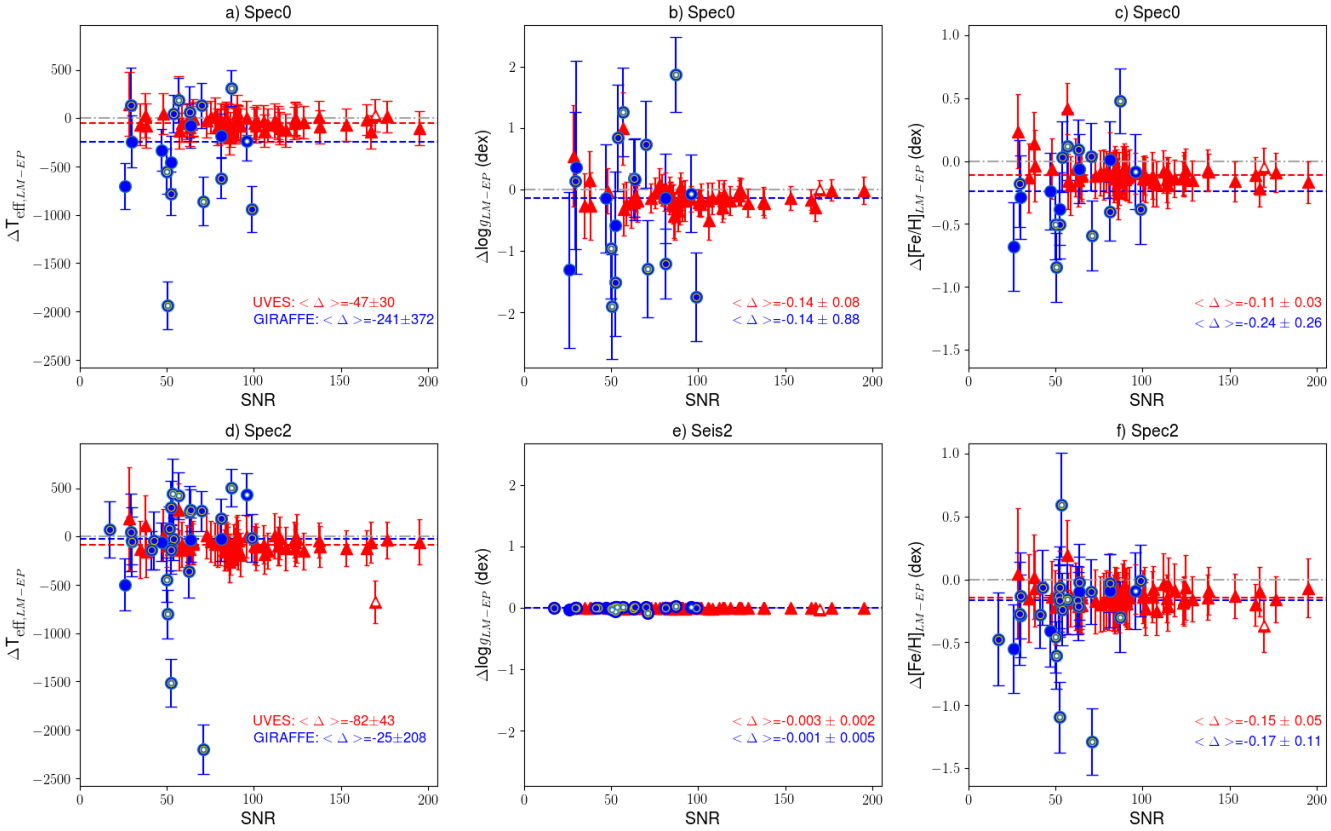

Fig. 6. Comparison between the EPINARBO and Lumba parameters against signal-to-noise (S/N) determined for Spec0 in the *top row* and Spec2 in the *bottom row*. *Left to right*: the panels compare spectroscopic $T_{\rm eff}$, spectrocopic/seismic $\log g$, and spectroscopic [Fe/H], in turn, for UVES (red) and GIRAFFE (blue) spectra. Yellow circles are stars rejected by EPINARBO for inconsistent Fe I and Fe II abundances in Spec0. Central white circles (GIRAFFE) or white triangle (UVES) are stars rejected by EPINARBO for inconsistent Fe I and Fe II abundances in Spec2. The median and MAD of the difference is given for each.

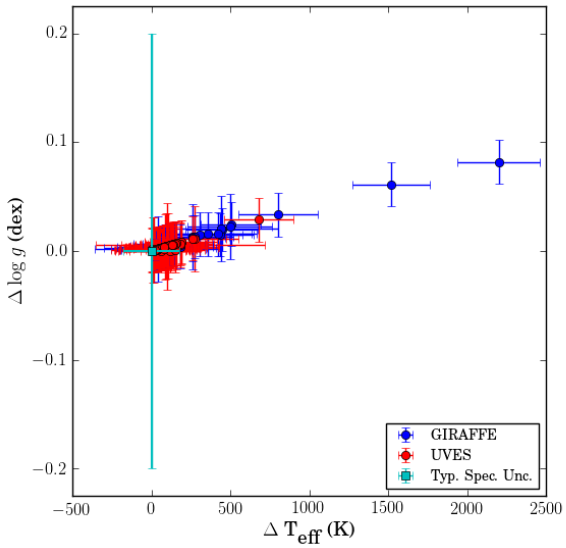

Fig. 7. Node difference in final seismic $\log g$ against the difference in final $T_{\rm eff}$ for the high (red) and medium (blue) resolution data. Typical spectroscopic uncertainties are shown in cyan.

spectroscopic $T_{\rm eff}$ upon which the final seismic $\log g$ values are based. In cyan we show the typical uncertainties for $T_{\rm eff}$ and $\log g$ when determined spectroscopically. Differences in spectroscopic $T_{\rm eff}$ greater than 500 K equate to less than a 0.1 difference in seismic $\log g$, which agrees with the discussion in Sect. 3.

While asteroseismology pinpoints the $\log g$, it does so from a large potential range in $T_{\rm eff}$. Therefore, complementary methods are needed, such as spectroscopy, to accurately converge on all stellar parameters.

The goal at this point was to combine the EPINARBO and Lumba Spec2 results to produce a final spectroscopic $T_{\rm eff}$ (and [Fe/H]) from which a final seismic $\log g$ could be calculated. However, prior to this, it was important to understand the differences between the node analyses, particularly with regard to stars for which there was large disagreement, as we did not want to blindly assume that a mean of the parameters from the two nodes was sufficient as a best final value. To assess the goodness of the results, ancillary information was compared to the differences in the parameters to ensure that the results that were selected were of the best quality possible.

Information that was considered was: (1) Node uncertainties on parameters; (2) Quality assessment reported by Nodes; (3) Microturbulence (ξ); (4) Normalised χ^2 between observed and synthetic spectra; and (5) Comparison to photometric $T_{\rm eff}$.

As stated above, there was no obvious trend with S/N so it was not considered in the following quality assessment. The IRFM and Node final parameters are given in Table C.2 for the UVES and GIRAFFE samples.

3.4.1. Uncertainties on parameters

Figure 8 shows the uncertainty distributions for the spectroscopic parameters $T_{\rm eff}$ and [Fe/H] for both EPINARBO and Lumba for the GIRAFFE and UVES analyses. There

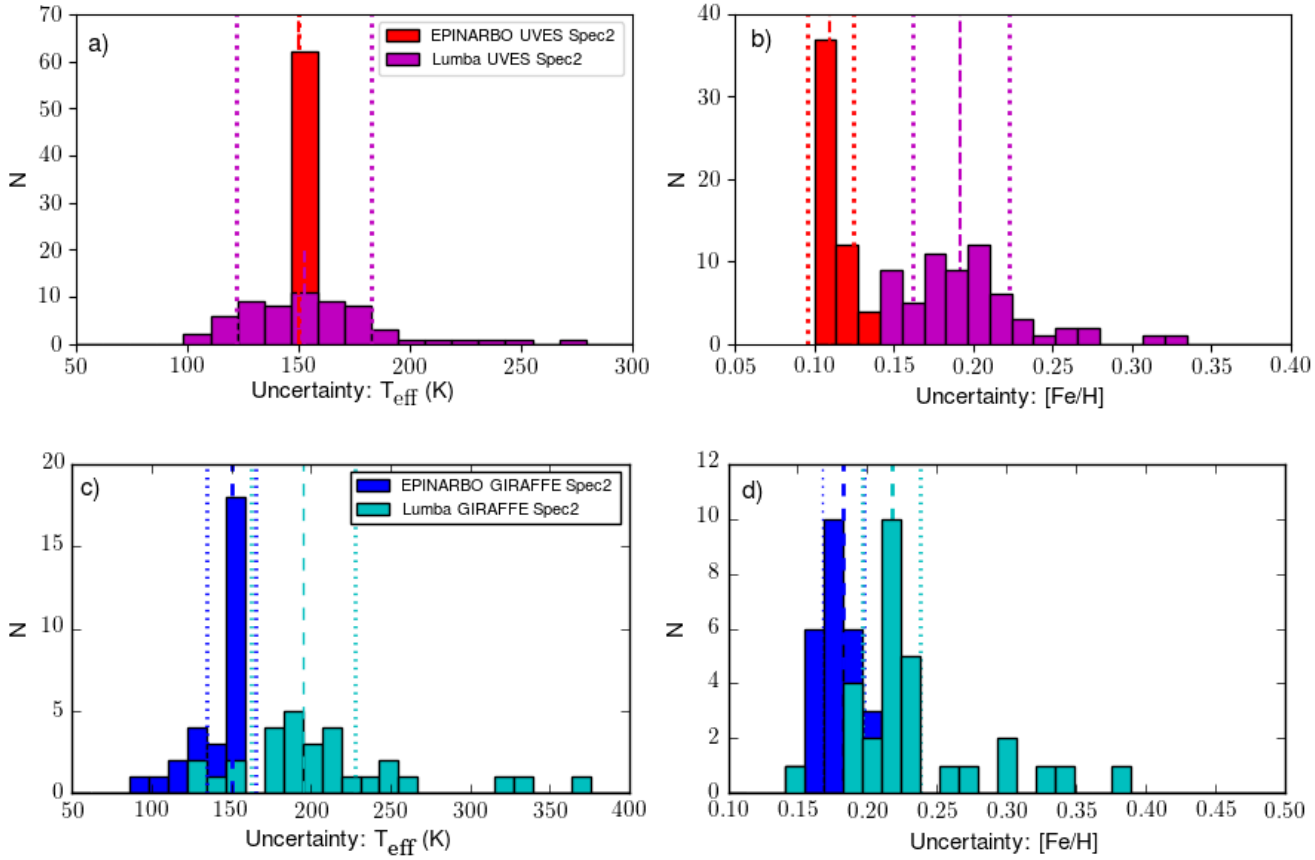

Fig. 8. Uncertainty distribution for $T_{\rm eff}$ and [Fe/H] for EPINARBO and Lumba for UVES (*a* and *b*), and GIRAFFE (*c* and *d*). The median for each distribution is shown as a dashed line with the respective colour, $\pm\sigma$ is shown as dotted lines.

is a systematic offset between the node distributions and EPINARBO reports a tighter distribution (with strict upper limit for $T_{\rm eff}$) than Lumba for both the UVES and GIRAFFE samples.

Each node has reported the uncertainties as best suits their analysis pipelines and, thus, they are internally consistent. However, the uncertainties are not calculated in the same way between the nodes. Due to this difference, they cannot be used to compare the node results (i.e. as a weight) to determine the best value for individual stars.

The difficulty of making comparisons between node results based on the respective uncertainty distributions, when the uncertainties are not defined in a standard way, has been a challenge throughout the lifetime of the *Gaia*-ESO Survey and for studies in Galactic Archeaology in general. Further discussions on uncertainty analyses can be found in Jofré et al. (2019).

3.4.2. Quality assessment

EPINARBO provided a list of stars for which the sample of Fe I and Fe II lines was inadequate for a robust analysis. These are indicated with a "*" in the CNAME column of Table C.2. There are eight of these stars within the GIRAFFE analysis and 1 star within the UVES analysis.

The uncertainty distribution of the Lumba results shows high tails inferring less confidence in the parameter determination for those stars. Objects with $T_{\rm eff}$ uncertainty > 294 K (244 K; median $T_{\rm eff}$ uncertainty + 3σ) and [Fe/H] uncertainty > 0.28 (0.28; the median [Fe/H] uncertainty + 3σ) were assumed to indicate lower confidence by Lumba in the parameters for the GIRAFFE (UVES) samples.

3.4.3. Microturbulence (ξ)

The ξ was provided by the nodes for both the GIRAFFE and UVES analyses. The ξ relation derived based on iDR1 was used often as a starting point for iterations or as a derived value depending on the respective node procedures. The difference between node ξ values were in some cases very high, particularly for the GIRAFFE analysis.

Figure 9 compares the node ξ values for both the (a) UVES and (b) GIRAFFE analyses directly with a colourmap of $\Delta T_{\rm eff,LM-EP}$. For UVES, there was one star with a large difference in ξ, but otherwise there was no strong evidence of $\Delta\xi$ correlating with $\Delta T_{\rm eff}$. For GIRAFFE the extreme differences in ξ typically were accompanied by other extremes in parameters which are described below. A difference of $\xi > 1\,{\rm km\,s^{-1}}$ was used as a threshold when considered alongside the other indicators of goodness of fit.

This comparison of the ξ values between the two nodes and the two resolutions for the K2@*Gaia*-ESO sample revealed an error in the microturbulence relation made available for iDR1. Thanks to this work, the relation was re-derived based on iDR5 values for the iDR6 analysis (see Worley et al., in prep.).

3.4.4. Normalised χ^2

It was necessary to independently assess the goodness of fit of the node solutions for the GIRAFFE analyses due to large differences between the reported node parameters. To this end, synthetic spectra for both HR10 and HR21 wavelength ranges were generated for each star using Turbospectrum (Plez 2012) and

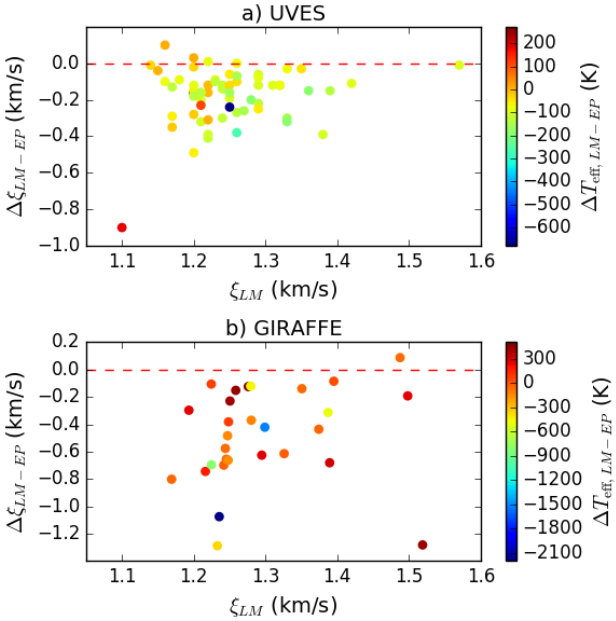

Fig. 9. $\Delta\xi_{\mathrm{LM-EP}}$ against ξ_{LM} with a colourmap of $\Delta T_{\mathrm{eff,LM-EP}}$ for (*a*) UVES; (*b*) GIRAFFE.

the MARCS stellar atmosphere models (Gustafsson et al. 2008). Interpolating between the models (Masseron 2006), the spectra were generated at the parameters derived by each node and then a normalised χ^2 was calculated between the synthetic spectrum and the observed spectrum. The observed spectrum was normalised to the synthetic spectrum in each case. In this way, the fit was optimised to the solution of each node. The goal was to look for obvious discrepancies in χ^2 to discard extreme outliers.

Two measures were used for assessing the goodness indication of the χ^2: (a) absolute difference between the EPINARBO χ^2 and the Lumba χ^2 ($|\Delta\chi^2|$); (b) absolute values of each node χ^2.

The set of parameters that represent the best-fit by χ^2_{BF} between EPINARBO and Lumba was used as the comparison set to avoid assuming that either EPINARBO or Lumba parameters were the best. Figure 10a compares $|\Delta\chi^2|$ with χ^2_{BF} also showing $\log|\Delta\chi^2|$ as a colourmap. This $\log|\Delta\chi^2|$ colourmap is used in Figs. 10b–d to explore the trend with other goodness of fit indicators. When considered in combination with other indicators of goodness of fit, typically all $|\Delta\chi^2| > 1.0$ indicated poor agreement between the nodes and so, in these cases, the node parameter set with the highest χ^2 value was rejected. This threshold is shown as a dashed line in Fig. 10a and the rejected points have a white dot at the centre.

Figure 10b compares the difference in [Fe/H] between the nodes with the difference in T_{eff} between the nodes. Typically, when one is large, the other is large, and the $\log|\Delta\chi^2|$ is also large, as expected. Figures 10c and d explore whether there is any trend of $\log|\Delta\chi^2|$ and $\Delta T_{\mathrm{eff,LM-EP}}$ with $T_{\mathrm{eff,LM}}$, and any trend of $\log|\Delta\chi^2|$ and $\Delta[\mathrm{Fe/H}]_{\mathrm{LM-EP}}$ with $[\mathrm{Fe/H}]_{\mathrm{LM}}$, in case a particular part of the parameter space was particularly susceptible. The Lumba T_{eff} and [Fe/H] were used as reference. There were no obvious trends in either case.

3.4.5. Photometric T_{eff}

The GIRAFFE sample showed, in particular, large disagreements between the two sets of node results. A comparison to the

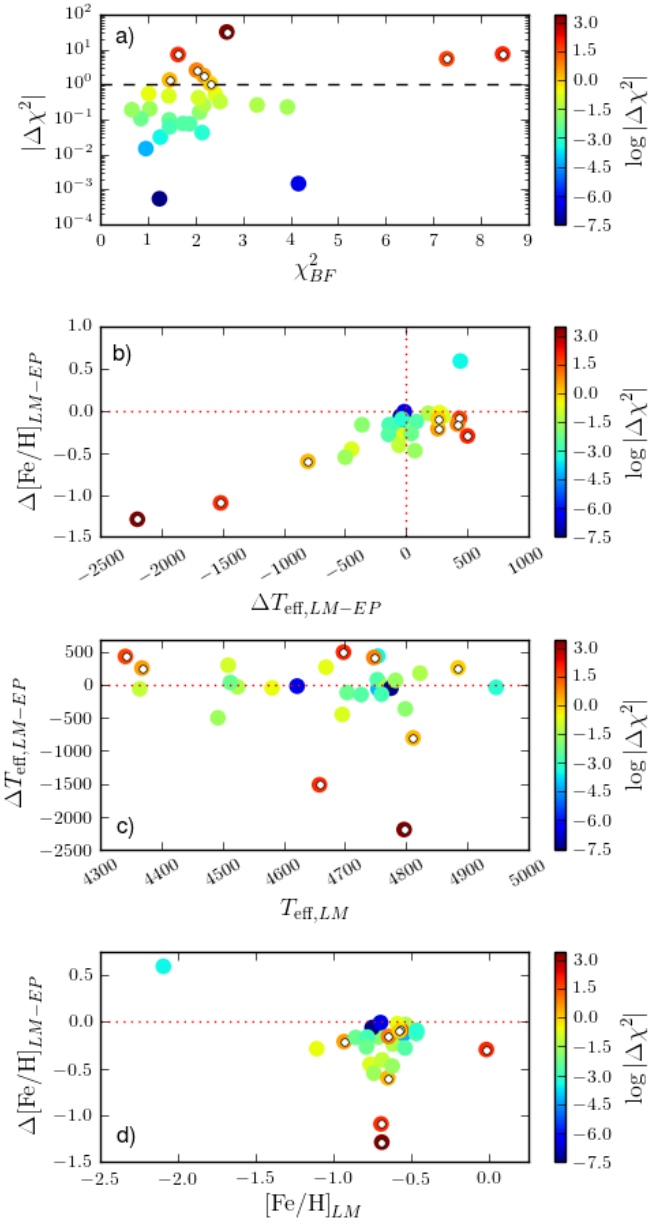

Fig. 10. Assessment of rejection criteria based on absolute difference of χ^2 between EPINARBO and Lumba. In each case the colourmap is $\log|\Delta\chi^2|$: (*a*) $|\Delta\chi^2|$ in a log scale against the best fit (BF) χ^2. Rejection limit at 1.0 is shown as a dashed line; (*b*) $\Delta[\mathrm{Fe/H}]_{\mathrm{LM-EP}}$ against $\Delta T_{\mathrm{effLM-EP}}$; (*c*) $\Delta T_{\mathrm{eff,LM-EP}}$ against $T_{\mathrm{eff,LM}}$; (*d*) $\Delta[\mathrm{Fe/H}]_{\mathrm{LM-EP}}$ against $[\mathrm{Fe/H}]_{\mathrm{LM}}$. The data points with a white centre are those rejected when $|\Delta\chi^2| > 1.0$.

photometric T_{eff} provided another useful indicator as the photometric and spectroscopic T_{eff} should be in relatively good agreement. Interstellar extinction is not expected to play a significant role in the photometric colours as these stars are towards the Galactic pole. When considered in combination with the other indicators, a difference of $T_{\mathrm{eff}} > 250$ K between the photometric and spectroscopic T_{eff} was empirically defined as being too great.

3.4.6. Final GIRAFFE spectroscopic parameters

The final spectroscopic stellar parameters (T_{eff}, [Fe/H], ξ) of the 28 stars in the GIRAFFE sample were defined by first inspecting

the node results using the criteria as described above to reject any poor parameter determinations (see Table C.2 for the photometric and node parameters, and the outlier assessment, as well as Table C.3 for the final spectroscopic parameters). In these cases, the remaining node parameter set was used as indicated in Col. 4 of Table C.3. There were 12 cases where only one of the node parameter sets was used. For eight of these cases, EPINARBO had reported large discrepancies between the Fe I and Fe II abundances, or a lack of suitable Fe II lines, for these stars. The χ^2 test confirms these as poor fits to the data, with the Lumba node providing significantly better fitting results.

The remaining four cases were considered as follows:

1. CNAME 22082566−1532383: The large discrepancies between the EPINARBO $T_{\rm eff}$ and the IRFM $T_{\rm eff}$ (−288 K), and also the Lumba $T_{\rm eff}$ (−360 K), considered with the large discrepancy between the EPINARBO ξ and the Lumba ξ ($-1.29\,{\rm km\,s^{-1}}$) indicated that there were issues with the EPINARBO result and so the Lumba result was taken as the final parameter set.
2. CNAME 22114679−1126477: Similarly, the large discrepancies between the EPINARBO $T_{\rm eff}$ and the IRFM $T_{\rm eff}$ (−455 K), and also the Lumba $T_{\rm eff}$ (−497 K), considered with the large discrepancy between the EPINARBO [Fe/H] and the Lumba [Fe/H] (−0.55) indicated that there were issues with the EPINARBO result and so, the Lumba result was taken as the final parameter set.
3. CNAME 22032304−0754111: The large discrepancy between the EPINARBO χ^2 and the Lumba χ^2 (−1.81) indicated an issue with the fit to the data; in this case, EPINARBO had the worst fit. This was borne out by inspecting the individual HR10 and HR21 χ^2 values, for which the HR21 χ^2 values were comparable between the nodes, but the EPINARBO χ^2 for HR10 was significantly worse. The difference in $T_{\rm eff}$ reflected this. The Lumba result was taken as the final parameter set.
4. CNAME 22154067−0627110: The discrepancy above the threshold of 1.0 between the EPINARBO χ^2 and the Lumba χ^2 (−1.06) indicated an issue with the fit to the data; also in this case EPINARBO had the worst fit. Inspection of the individual HR10 and HR21 χ^2 values also showed that the HR21 χ^2 values were comparable between the nodes, but the EPINARBO χ^2 for HR10 was significantly worse. The difference in $T_{\rm eff}$ reflected this. The Lumba result was therefore taken as the final parameter set.

3.4.7. Final UVES spectroscopic parameters

The final spectroscopic stellar parameters ($T_{\rm eff}$, [Fe/H], ξ) of the 62 stars in the UVES sample were defined also by first inspecting the node results using the criteria as described above to reject any poor parameter determinations. Overall, there was much better agreement between Lumba and EPINARBO for the UVES sample than for the GIRAFFE sample and so, it was not necessary to derive the independent χ^2 as an additional measure of goodness of fit. The difference in $T_{\rm eff}$ and [Fe/H] between nodes is seen in Fig. 6. While there is a mean difference that is comparable to the scatter, we are not in a position to favour one node over the other since we do not have reference values for stars of this sample. For *Gaia*-ESO, both nodes have been independently calibrated with the common set of reference parameters of the *Gaia* FGK benchmark stars. Therefore, it is not a straightforward task to decide which of the nodes in this particular case, where the pipelines were adapted to iterate with seismology, might be less accurate. In this light, the average of the node results were taken as the final spectroscopic parameters. See Table C.2 for the photometric and node parameters and the outlier assessment, as well as Table C.3 for the final spectroscopic parameters.

There are two remaining cases where the differences are significantly larger and are considered as follows:

1. CNAME 22000793−1203412: The large discrepancies between the Lumba $T_{\rm eff}$ and the IRFM $T_{\rm eff}$ (−263 K) considered with the large discrepancy between the EPINARBO ξ and the Lumba ξ ($-0.90\,{\rm km\,s^{-1}}$) and the very large uncertainty on the Lumba $T_{\rm eff}$ (512 K) and [Fe/H] (0.50) indicated that there were issues with the Lumba result and so the EPINARBO result was taken as the final parameter set.
2. CNAME 22032202−0829154: EPINARBO flagged this star as the only UVES star that they found to have a large discrepancy between the abundances derived from the Fe I and Fe II lines. The EPINARBO and Lumba $T_{\rm eff}$ disagree by $\Delta T_{\rm eff,LM-EP} = -679$ K. Both do not agree well with the IRFM $T_{\rm eff}$ with differences of −296 K and 383 K respectively. The initial spectroscopic $T_{\rm eff}$ derived from iSpec was 4643 K, which also does not agree with the IRFM $T_{\rm eff}$ nor EPINARBO. There is, however, no substantial difference between the seismic $\log g$ derived for each node (0.03). As EPINARBO flags an issue between the Fe I and Fe II, the Lumba parameters were taken as the final set. In the subsequent chemical analysis, the final Fe I and Fe II are in good agreement (Fe I−Fe II = 0.1), confirming this choice of parameters.

3.5. Final K2@Gaia-ESO stellar parameters

The homogenisation process carried out above resulted in the final catalogue of stellar parameters for the 90 K2@*Gaia*-ESO red giant stars. These are shown in Fig. 1, with the [Fe/H] as a colourmap. The final stellar parameters are list in Table C.3 and are provided in the final K2@*Gaia*-ESO catalogue of parameters and abundances which is available at the CDS. The columns of the full catalogue are listed in Table B.1.

4. K2@*Gaia*-ESO chemical abundances

The final phase of the analysis was the measurement of chemical abundances for those elements typically measured for *Gaia*-ESO by each node. Based on the final set of stellar parameters ($T_{\rm eff}$, $\log g$, [Fe/H], and ξ), each node determined their typical chemical abundances for the GIRAFFE and UVES spectra. The nodes provided abundances per star and also abundances per spectral line.

The homogenisation was undertaken using the line-by-line abundances in order for the results to be combined in a more informed way such that the effect of each spectral feature is considered separately. Even with the detailed work required to produce a refined, high-quality line list (Heiter et al. 2020), some of the spectral features used here are less well-modelled than others, which can be due to less robust line information or a strong influence coming from surrounding features, or less robust normalisation of the continuum about that feature. The larger pool of values for each spectral feature across the two nodes compared to a single global value from each node allows for the outlying spectral features to be identified and discarded, if needed, and for features that are in good agreement between the nodes to be more highly weighted.

Table 1. Elements measured for each element by EPINARBO and Lumba for the GIRAFFE and UVES K2 stars.

	UVES				GIRAFFE			
	EPINARBO		Lumba		EPINARBO		Lumba	
Element	Stars	Lines	Stars	Lines	Stars	Lines	Stars	Lines
Na I	61	2	62	1	–	–	–	–
Mg I	62	2	62	2	28	2	28	3
Al I	61	2	62	3	28	2	24	1
Si I	62	6	62	8	28	2	25	4
Si II	44	1	62	2	–	–	–	–
Ca I	62	6	62	19	21	1	–	–
Ca II	–	–	61	2	–	–	–	–
Sc I	61	4	62	4	–	–	–	–
Sc II	62	4	62	4	24	1	28	1
Ti I	62	17	62	39	28	10	–	–
Ti II	62	7	62	7	28	2	–	–
V I	62	14	62	24	20	2	–	–
Cr I	62	12	62	20	–	–	25	1
Cr II	–	–	45	1	–	–	–	–
Mn I	–	–	62	10	–	–	27	3
Fe I	62	64	62	14	28	9	28	34
Fe II	62	8	62	3	28	2	–	–
Co I	62	13	62	18	28	3	27	3
Ni I	62	13	62	24	28	2	22	2
Cu I	62	1	62	2	–	–	–	–
Zn I	61	2	62	1	–	–	–	–
Y II	62	6	62	5	27	1	–	–
Zr I	59	5	62	5	–	–	–	–
Zr II	34	1	–	–	–	–	–	–
Ba II	53	1	62	3	–	–	–	–
La II	60	3	–	–	–	–	–	–
Ce II	60	2	–	–	–	–	–	–
Nd II	–	–	62	8	–	–	–	–
Eu II	57	1	62	1	–	–	–	–

Notes. The number of stars per element and the median number of clean spectral lines measured per element are given.

This was carried out only for those elements for which at least one of the nodes measured more that 50% of the sample, that is, more than 14 stars for GIRAFFE and more than 31 stars for UVES. The threshold of 50% was chosen to meet the requirement for a reference set to be as complete as possible in the reported measurements across all the stars in the set. The node results for any element with less than these thresholds were discarded. The remaining elements and number of K2 stars that were measured by each node and the median number of spectral lines each node measured per element are listed in Table 1.

The compilation of spectral lines used for *Gaia*-ESO is described in Heiter et al. (2020) and the individual sources for the spectral lines for each element, summarised in Heiter et al. (2020), are as follows: Na I – Ralchenko et al. (2010); Mg I – Ralchenko et al. (2010); Al I – Wiese et al. (1969); Si I – Garz (1973), Kurucz (2007); Si II – Kurucz (2012); Ca I – Drozdowski et al. (1997), Kurucz (2007), Smith (1981), Smith & O'Neill (1975), Smith (1988), Smith & Raggett (1981); Ca II – Seaton et al. (1994); Sc I – Lawler & Dakin (1989); Sc II – Kurucz (2009), Lawler & Dakin (1989); Ti I – Kurucz (2010), Nitz et al. (1998), Lawler et al. (2013); Ti II – Wood et al. (2013), Kurucz (2010), Ryabchikova et al. (1994); V I – Kurucz (2009); Cr I – Wallace & Hinkle (2009), Kurucz (2010), Sobeck et al. (2007); Cr II – Sigut & Landstreet (1990), Kurucz (2010), Pinnington et al. (1993); Mn I – Kurucz (2007), Den Hartog et al. (2011); Fe I – Kurucz (2007), Fuhr et al. (1988), Bard et al. (1991), O'Brian et al. (1991), Bard & Kock (1994); Fe II – Blackwell et al. (1980), Kurucz (2013); Co I – Kurucz (2008); Ni I – Kurucz (2008), Wickliffe & Lawler (1997); Cu I – Kurucz (2012); Zn I – Lambert et al. (1969), Warner (1968); Y II – Biémont et al. (2011), Kurucz (2011), Pitts & Newsom (1986), Hannaford et al. (1982); Zr I – Biemont et al. (1981); Zr II – Ljung et al. (2006), Cowley & Corliss (1983); Ba II – Miles & Wiese (1969); La II – Lawler et al. (2001a); Ce II – Lawler et al. (2009); Nd II – Meggers et al. (1975), Den Hartog et al. (2003); Eu II – Lawler et al. (2001b).

4.1. Line-by-line cleaning

Lines were accepted or rejected following the rules outlined in Smiljanic et al. (2014), but with appropriate modifications as this project has results from only two nodes, rather than upward of three nodes for the full *Gaia*-ESO WG11 homogenisation. This meant *Rules 1, 2*, and *3* of the full *Gaia*-ESO WG11 homogenisation process were not applicable here. Also, we did not apply the weights based on the parameters used in Smiljanic et al. (2014) so *Rule 7* was also not applicable. The remaining rules (4, 5, 6, 8) were applied as follows:

- *Rule 4*: When information of the EWs was available, only lines with $5 \leq \mathrm{EW(m\AA)} \leq 120$ were used. Exceptions were sodium ($5 \leq \mathrm{EW(m\AA)} \leq 140$) and barium ($5 \leq \mathrm{EW(m\AA)} \leq 250$). This could only be applied for the EW node EPINARBO and no cases outside the limits were found for these stars.
- *Rule 5*: If, for a given species at a given star, abundances from 20 or more different spectral lines were available, we removed the ones that are flagged as blended in the *Gaia*-ESO line list (*U*). This was applied as specified.
- *Rule 6*: If [...] the total number of spectral lines with abundances (for a given species of a given star) is more than 20, a 2σ clipping from the mean value was applied. (The total number of lines is counted across all nodes, therefore if eight nodes provide abundances for five lines each, it counts as 40 lines for the clipping). This was adapted to the total lines from the two nodes.
- *Rule 8*: The median value of multiple lines is adopted as the recommended abundance. This was adapted to be the median of all lines from both nodes.

The reported spectral lines from each node were "cleaned" so to include only those lines flagged as *Y* or *U* in the two *Gaia*-ESO line list flags *gf_flag* and *synflag*, except in the case of *Rule 4* above. The definition of the *Gaia*-ESO line list flags are taken from Heiter et al. (2020) and are as follows:

1. *gf_flag*
   - *Y*: data which are considered highly accurate, or which were the most accurate ones available for the element under consideration at the time of compilation.
   - *U*: Data for which the quality is not decided
   - *N*: Data which are considered to have low accuracy.
2. *synthflag*
   - *Y*: Line is unblended or only blended with line of same species in both stars (Sun and Arcturus).
   - *U*: Line may be inappropriate in at least one of the stars.
   - *N*: Line is strongly blended with line(s) of different species in both stars.

The reported abundances are thus the median of the remaining line-by-line abundances once the above rules and cleaning were applied. The associated uncertainty was then the MAD

converted to a standard deviation by the scale factor of 1.48 ($\sigma = \mathrm{MAD} \times 1.48$).

In the cases of Cr II and Zr II for UVES, and Ca I, Cr I and Y II for GIRAFFE, only one node provided results for a sufficient number of stars and these were based on one spectral line only. This resulted in an associated uncertainty of zero by the above prescription. In these cases, the uncertainty reported by the node on the spectral line was taken as the uncertainty.

Also, in some cases, the associated uncertainty for a particular star for an element was calculated to be zero while the remaining stars for that element had a non-zero associated uncertainty by the above prescription. In those cases, the median non-zero uncertainty and the MAD converted to sigma on the non-zero uncertainty was calculated from the rest of the sample. A lower threshold was set as the median non-zero uncertainty minus twice the sigma. All associated uncertainties lower than this were set instead to this threshold.

4.2. Intra-node corrections

There were seven elements (Mg I, Al I, Si I, Ca I, Ti II, Ni I, Y II), for which combining the results proved difficult due to systematic offsets between the GIRAFFE and UVES datasets of each node. The seven sets of per instrument and per node results are shown in Fig. A.1.

As there were no stars in common between the GIRAFFE and UVES datasets the way to assess an offset was to look at the overlapping region in [Fe/H] [−0.8 to −0.4] between the two datasets per node. Two assumptions were made to assess the magnitude and direction of the corrections: (1) results from a single node should be continuous in [Fe/H] between the UVES and GIRAFFE results; (2) the Node abundance values around solar metallicity should be similar to the solar abundance.

These allowed the assessment of an offset (difference of the medians across the [Fe/H] range) and the direction of the correction. For instance, for Mg I the EPINARBO GIRAFFE and UVES medians disagree by 0.3 in the overlapping [Fe/H] region. However, we expect solar Mg I at solar [Fe/H], hence the correction was applied to the EPINARBO UVES results. This assessment was carried out resulting in the offsets in Table 2 which were then applied at the per-line level.

Table 2. Node systematic offsets calculated between GIRAFFE and UVES medians across the [Fe/H] range for seven elements and the node-instrument dataset to which they were applied.

Element	Node	Instrument	Offset
Mg I	EPINARBO	UVES	−0.30
Al I	EPINARBO	UVES	−0.37
Si I	Lumba	GIRAFFE	−0.37
Ca I	EPINARBO	GIRAFFE	−0.165
Ti II	EPINARBO	GIRAFFE	−0.215
Ni I	Lumba	GIRAFFE	−0.18
Ni I	EPINARBO	GIRAFFE	−0.41
Y II	EPINARBO	UVES	+0.185
Y II	Lumba	UVES	+0.41

4.3. Comparison of chemical species

Seven of the elements considered here have measurements for both the neutral and ionised species: Ca, Cr, Fe, Sc, Si, Ti, and Zr. A comparison between species is shown in Figs. 11 and 12. GIRAFFE values (blue points) were only available for Ti and Fe.

In most cases, there is an offset between species on the order of the scatter on the difference. For Zr, for which the median offset is 0.31 ± 0.11, the largest uncertainties correspond to the stars with the greatest disagreement. Typically for all elements the individual stars with largest difference have a large uncertainty on one of the species measurements. There are no obvious trends with any of the parameters.

Figure 12 compares Fe I with Fe II, then the difference of these against [Fe/H], $T_{\rm eff}$ and $\log g$. These are the abundances derived for each species of Fe using the final set of stellar parameters. They are distinct from, but based on, the stellar parameter [Fe/H] which is the global metallicity determined in the parameter round. There is excellent agreement between Fe I and [Fe/H] for both the UVES (-0.03 ± 0.02) and GIRAFFE (0.03 ± 0.05) samples. The agreement for Fe II is less good, showing a larger offset with [Fe/H] for UVES (-0.11 ± 0.04), as well as a large offset and much larger scatter for GIRAFFE (0.13 ± 0.14).

In particular, for GIRAFFE, 10 of the 28 stars have a Fe I−Fe II > 0.2, which is the median combined error on the abundance differences of the species for the GIRAFFE spectra. Two of these have a difference greater than 0.5.

At the parameter determination stage, EPINARBO flagged stars for which the Fe I and Fe II abundances were inconsistent. These are indicated with white dots for GIRAFFE and as a yellow triangle for the single UVES spectrum in Fig. 12. While some of these are still outliers, some have been reclaimed as now being consistent between Fe I and Fe II.

Of the two with Fe I and Fe II abundance differences greater than 0.5, only CNAME 22063424−1530038 was flagged by EPINARBO in the parameter round as having inconsistent Fe I and Fe II abundances. There was also a difference in Spec2 $T_{\rm eff}$ between the nodes of 504 K. Consequently only the Lumba parameters were used for the final parameters (see Table C.3). This star has an outlying rotational velocity which is discussed further in Sect. 6.2.

CNAME 22071427−1431390, also with Fe I−Fe II > 0.5, was not flagged as an outlier during the parameter stage, although there is a difference in the Spec2 [Fe/H] values between Lumba and EPINARBO of −0.24. It has, however, been flagged as a potential binary (see Sect. 6). Two other spectra with Fe I−Fe II > 0.5 were also flagged as potential binaries: CNAMEs 22003290−0808595, 22031541−0753433.

To further understand the possible source of inconsistencies for the remaining seven GIRAFFE stars, for GIRAFFE, the Fe II value is based on a maximum of two spectral lines and only comes from the EPINARBO analysis, compared to at least nine lines for the Fe I value from both EPINARBO and Lumba (see Table 1). Additionally, the Fe II lines are also typically weaker and thus more difficult to measure in medium- compared to high-resolution spectra, resulting in less certain values as indicated by the larger uncertainty bars.

For UVES, 3 of the 62 stars have a Fe I−Fe II > 0.16, which is the median combined error on the abundance differences of the species for the UVES spectra, although none of these have a difference greater than 0.3. None of these three (CNAMEs 22065112−1504580, 22195215−1234594, 22021848−1139147) were identified as an outlier in the parameter homogenisation. CNAME 22065112−1504580 has the largest difference between Fe I and Fe II of −0.28 and it is the only one of these three to be flagged as a potential binary (see Sect. 6).

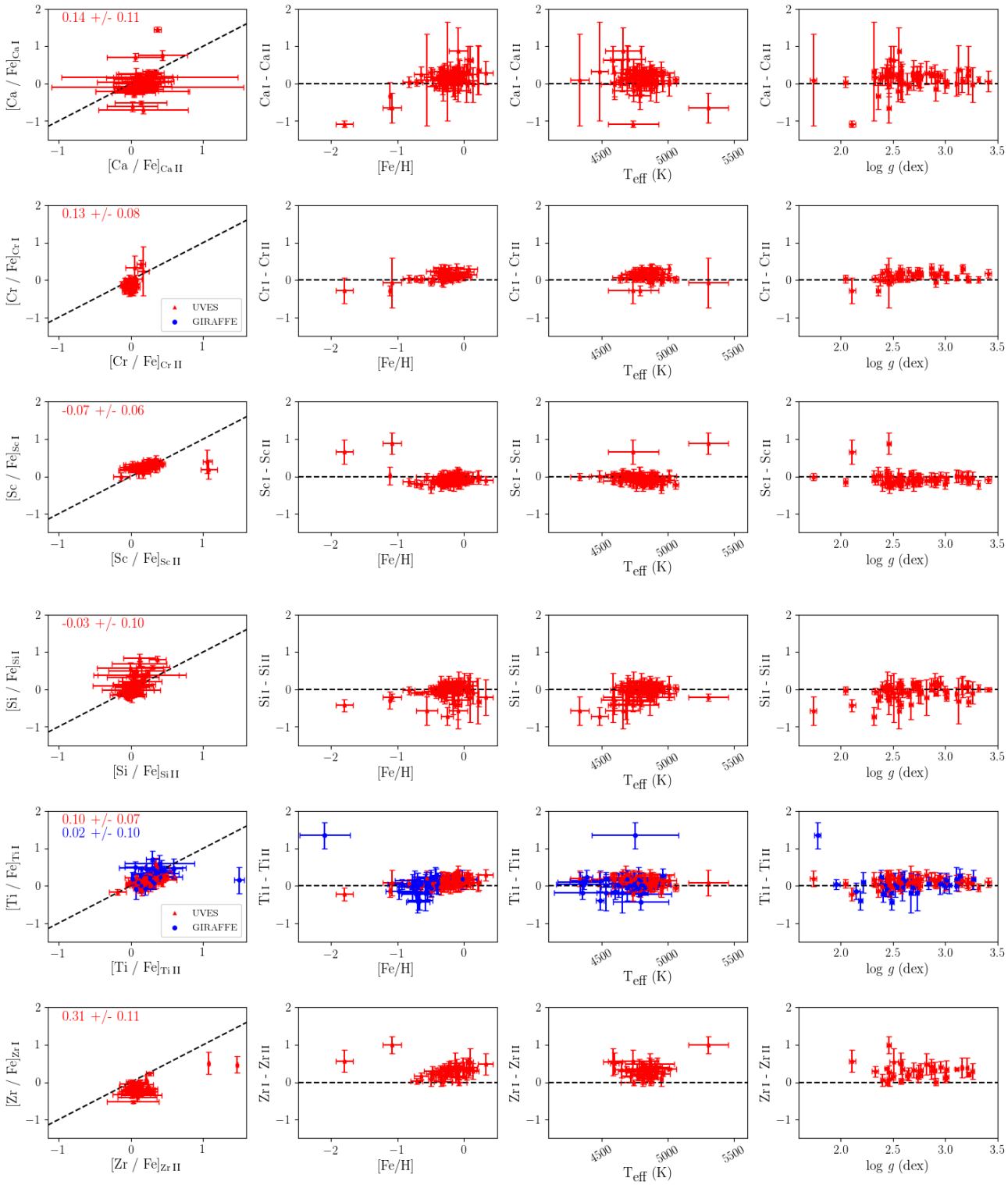

Fig. 11. Comparing neutral and ionised species of Ca, Cr, Sc, Si, Ti, and Zr as [X I/Fe] against [X II/Fe], and X I–X II against [Fe/H], $T_{\rm eff}$, and log g. Median and MAD of the difference between species of the same element are shown. Red displays the UVES sample, blue displays the GIRAFFE sample.

We note that the ionisation equilibrium (consistent abundance values between neutral and ionised species) may not have been achieved in these cases because the log g value was constrained by non-spectroscopic data, which may reflect shortcomings of the atmospheric models used in the spectroscopic analysis, such as the LTE and 1D prescriptions.

4.4. K2@Gaia-ESO final chemical abundances

The final chemical abundances for the K2@*Gaia*-ESO stars with the above corrections applied are shown in full in Fig. C.1. The full catalogue table is available at the CDS but the columns are provided in Table B.1. The UVES (high-resolution) and

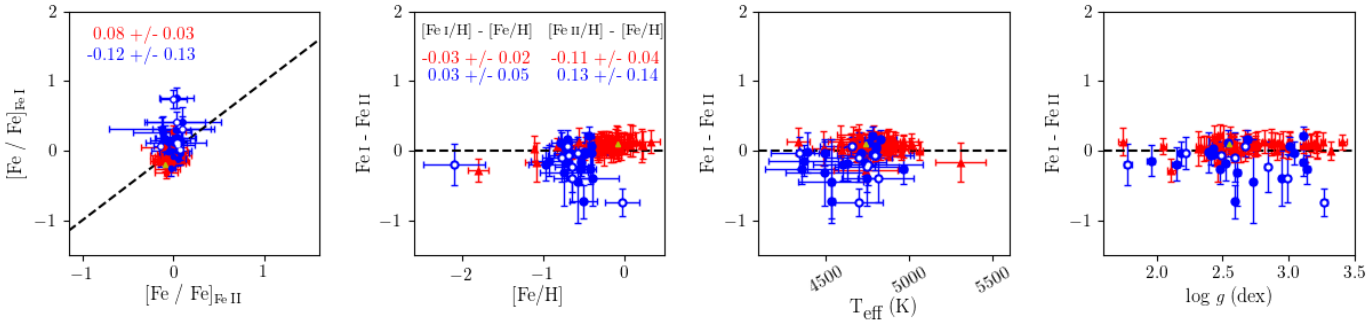

Fig. 12. Comparing neutral and ionised species of Fe as [Fe I/Fe] against [Fe II/Fe], and Fe I−Fe II against [Fe/H], $T_{\rm eff}$, and log g. Median and MAD of the difference between species of the same element are shown. Red displays the UVES sample, blue displays the GIRAFFE sample. Stars flagged by EPINARBO in the parameter round as having inconsistent Fe I and Fe II are indicated as white dots for GIRAFFE and a yellow triangle for UVES.

GIRAFFE (medium-resolution) measurements are shown separately. In general the two resolutions track each other for each element distribution, with the improvements due to the corrections applied above. Overall, there appears to be greater scatter in the GIRAFFE datasets, which is not unexpected, particularly for those elements where the measured spectral lines are weak or more blended at lower resolutions (see figures in e.g. Jofré et al. 2019).

The final stage of this work is focussed on the derivation of ages and masses within the greater K2 Galactic Caps Project (see Paper I). Specifically for this paper, the ages of the K2@*Gaia*-ESO sample were derived, shown as a colour map on the chemical distribution of key elements in Fig. 13.

This set of elements is arranged in five key nucleosynthetic channels: Light odd-*Z*, α, Fe-Peak, *s*-process and *r*-process. Each of these channels reflect different nucleosynthetic origins in stellar evolution. Elements created in the same channel show similar behaviour in chemical distribution morphology. These are interpreted in consideration of the recent release of the GALAH DR2 abundances presented in Buder et al. (2019) which used a pipeline which was developed based on the experience with the Lumba pipelines. We note that this is a qualitative comparison only. On the one hand, there are no stars in common between this sample and GALAH DR2. In fact, *Gaia*-ESO and GALAH only have a small overlap in observed targets (the *Gaia* benchmark stars, some targets in M67 and the CoRoT fields). On the other hand, our methodology differs from the standard *Gaia*-ESO parameters so direct comparison between surveys is not the aim here.

Considering the two Light odd-*Z* elements, Na I shows the expected trend of depleted Na at low metallicity increasing to ~0.15 at super-solar metallicity. Its distribution is similar to Ni I and Cu I as expected from previous studies (Buder et al. 2019). On the other hand, Al I shows enhanced Al at low metallicity, although no non-LTE corrections have been applied contrary to Buder et al. (2019). Al behaves similarly to Mg and the other α elements, also noted in Buder et al. (2019). The α elements presented here (Mg I, Ca I, Ti I[1]) all bear the same morphology of showing enhancement at low metallicity decreasing to solar at solar metallicity, which is the typical chemical distribution of α elements (Buder et al. 2019).

The Fe-peak elements (V I, Mn I, Co I, Ni I, Cu I) show at least four types of morphology. V I is unique in that it stays generally constant with a large scatter over the presented metallicity range, which is consistent with other studies. Mn I also is consistent with other studies showing a clear trend of increasing Mn I with metallicity. Co I, Ni I and Cu I can be grouped with similar if not the same morphology of slightly increasing at the metal-poor end, then slightly decreasing then slightly increasing again at solar. This is also not dissimilar to Na I as noted above. The overall increasing trend with metallicity follows that presented in other studies (Buder et al. 2019) although the behaviour around solar begs further investigation.

The *s*-process is separated into the light (Y II and Zr II) and Heavy (Ba II, La II, Nd II) *s*-process peaks. Y II shows a large scatter with there being enhancements and depletions for both old and young stars. This was similarly found in Buder et al. (2019). There are fewer measurements for Zr II, particularly at the metal-poor end, but a similarly large spread is indicated.

For the heavy *s*-process, there are only few measurements at the metal-poor end but these mostly indicate enhanced levels for metal-poor stars for Ba II, La II and Na II. Despite showing a larger scatter for Ba II, all are fairly constant around solar. Finally, the single *r*-process element, Eu II, shows enhancements at low metallicity, decreasing to a constant solar values at solar and super-solar metallicities, not unlike the α distributions. Although the sample is small compared to other samples where spectroscopy and seismology is available (e.g. Pinsonneault et al. 2018), even for this sample of 90 stars, the morphology of the different nucleosynthetic channels can be seen.

The key outliers in this sample are the two most metal-poor stars which appear to be quite young (~2 Gyr). This is discussed further in Sect. 6.

5. K2@*Gaia*-ESO@*Gaia*: Parallaxes

The iterative determination of the seismic log g and spectroscopic $T_{\rm eff}$ and [Fe/H] was completed prior to the release of *Gaia* DR2 in April 2018. However, the parallaxes from *Gaia* DR2 provide a useful check on the robustness of the final K2@*Gaia*-ESO surface gravities.

The log g based on the *Gaia* parallax was calculated using the following additional inputs: the final K2@*Gaia*-ESO $T_{\rm eff}$ and [Fe/H]; the reddening, $E(B-V)$, assigned to each target as part of the *Gaia*-ESO dataset was taken from Schlegel et al. (1998); and the 2MASS K band photometry (Skrutskie et al. 2006). Of the 90 stars, only 58 are compared here due to the *Gaia* parallax either not being available or not good enough (parallax uncertainty was greater than 15%).

An iterative procedure using isochrones to determine the optimal stellar mass and surface gravity based on the *Gaia* parallaxes was carried out (log $g_{\rm iso}$). Further details on the calculation

[1] Ti behaves observationally like the rest of the α elements.

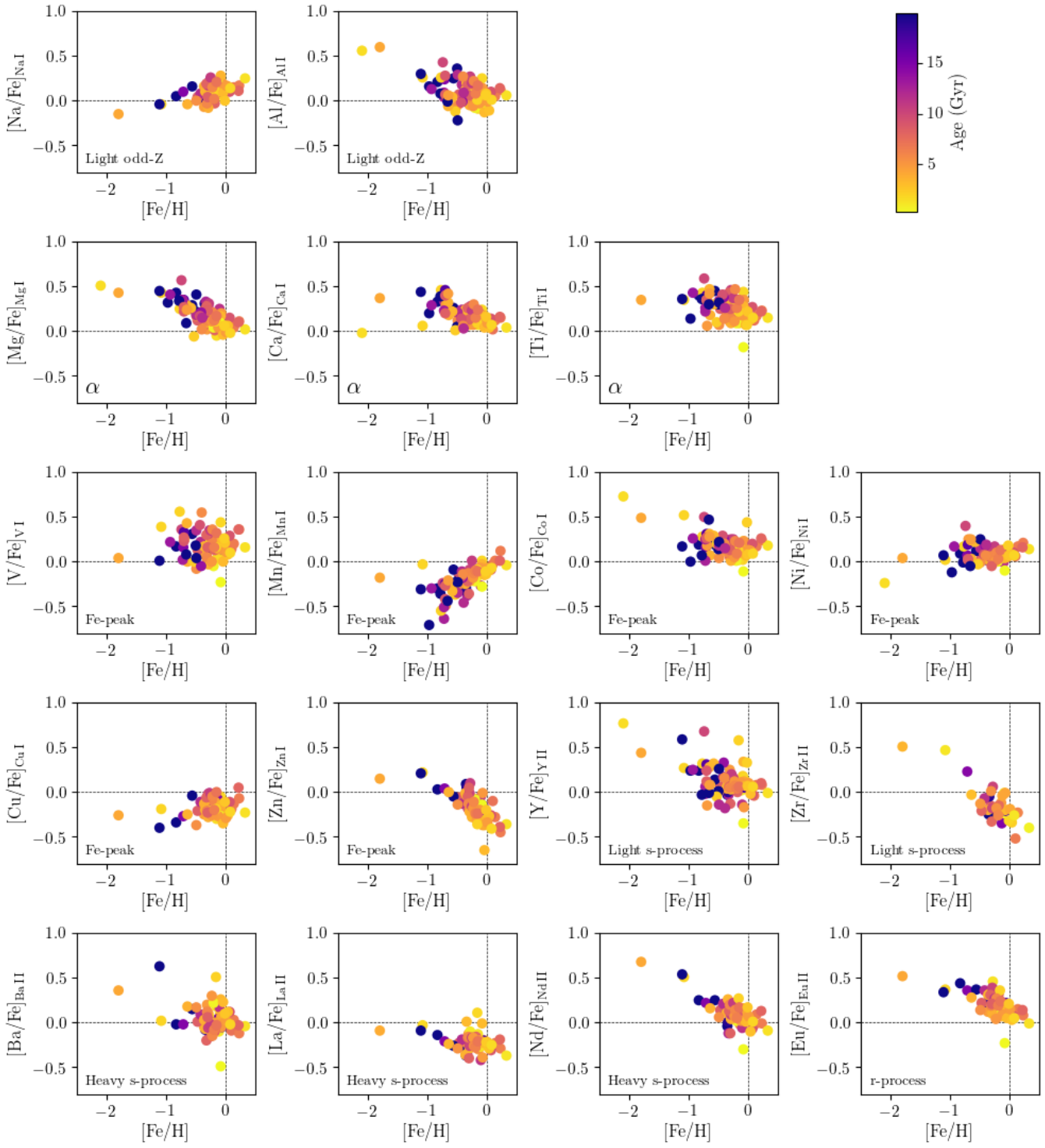

Fig. 13. Chemical abundances of [X/Fe] against [Fe/H] for the K2@*Gaia*-ESO stars with a colourmap of Age. [Fe/H] = 0 and [X/Fe] = 0 are indicated as dashed lines.

are provided in Appendix D. For comparison, the surface gravity based on the *Gaia* parallax assuming only solar mass was also calculated ($\log g_{M_\odot}$).

Figure 14a compares $\log g_{M_\odot}$ with the final K2@*Gaia*-ESO $\log g$ and Fig. 14b compares $\log g_{\rm iso}$ with the final K2@*Gaia*-ESO $\log g$. The mean offset for each are $\Delta \log g_{M_\odot - {\rm K2}} - 0.20 \pm 0.14$ and $\Delta \log g_{\rm iso - K2} - 0.08 \pm 0.08$ respectively. Overall $\log g_{\rm iso}$ are in better agreement with the K2@*Gaia*-ESO $\log g$ than $\log g_{M_\odot}$. The typical reported $\log g$ uncertainties of K2 are 0.02 and for the *Gaia* analysis are 0.13. Spectroscopic $\log g$ typical uncertainties are 0.10 to 0.25 for the *Gaia*-ESO high-resolution UVES spectra (Smiljanic et al. 2014) and 0.15 to 0.40 for the *Gaia*-ESO medium-resolution GIRAFFE spectra (Worley et al., in prep.).

It is known that the parallaxes provided by *Gaia* DR2 are affected by systematics (Lindegren et al. 2018; Zinn et al. 2019). A comparison of *Gaia* parallaxes and K2 seismic parallaxes for stars in the C3 field in Khan et al. (2019) found an offset

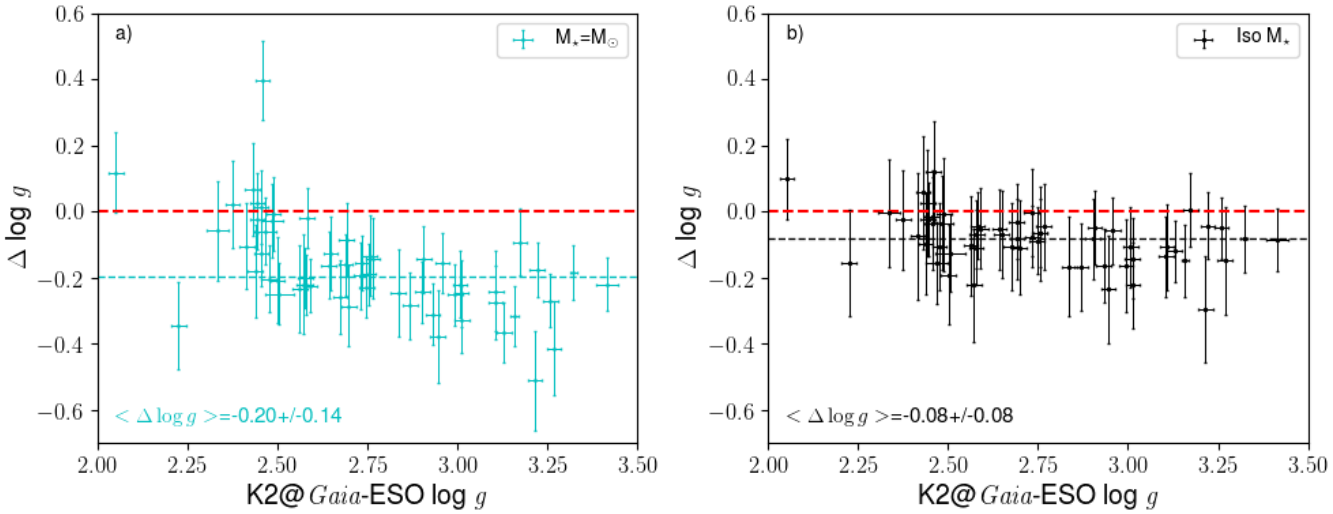

Fig. 14. Comparison of $\log g$ determined using *Gaia* parallax with the final K2@*Gaia*-ESO seismic $\log g$. Cyan points are derived from an initial mass equal to solar, black points are derived from masses based on isochrones. The dashed red line shows the zero difference and the dotted black and cyan lines shows the mean of the differences respectively.

ranging between −45 and −55 μas. The authors found that the correction in the parallax between *Gaia* and seismic values seems to depend, to varying degrees, on the position on the sky, the magnitude, and, potentially, the colour. Also, specifically for the K2, C3 and C6 fields, the correction seems to be smaller than in the *Kepler* field. Following the recommendation in Khan et al. (2019), no ad hoc correction was attempted here but the possible systematics are noted as follows.

Using the equations in Appendix D, the possible range in offsets in parallax corresponds to a range in offsets in $\log g_{Gaia-\mathrm{K2}}$ of −0.05 to −0.07. This is in the same direction and of similar magnitude to that measured here, showing the offset between parallaxes from *Gaia* DR2 and asteroseismology found in this study is in agreement with the previous studies (Zinn et al. 2019; Khan et al. 2019).

The main outlier is CNAME 22235003−1422417 with $\Delta \log g_{Gaia-\mathrm{K2}} = -0.30 \pm 0.16$. This star was observed with UVES and had not been flagged as particularly peculiar otherwise. The seismic $\log g$ values for each node were in good agreement which is not unexpected as shown above. The difference between the node $T_{\rm eff}$ values is LM-EP = −130 K and [Fe/H] values is LM-EP = −0.39. These are within the acceptable limits imposed in this study for classifying outliers. Three other stars have $|\Delta \log g_{Gaia-\mathrm{K2}}| > 0.20$.

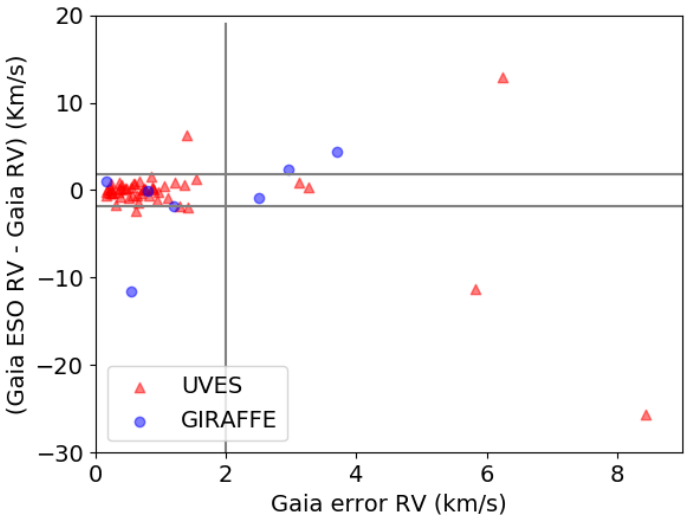

Fig. 15. Comparison of radial velocities of *Gaia*-DR2 and *Gaia*-ESO as a function of the uncertainty reported by *Gaia*. Stars that have larger uncertainties than the vertical line at 2 km s^{-1}, or a larger RV difference than the horizontal lines at 2 km s^{-1}, are classified as binaries in this work.

6. K2@*Gaia*-ESO@*Gaia*: binary stars

Both the spectra of *Gaia*-ESO and the astrometric measurements of *Gaia* offer important information about a star's movement. These can be combined to study potential binary stars in the sample. This information is given in Table C.4.

We compared the radial velocities (RV) of *Gaia*-ESO with those from *Gaia* (Sartoretti et al. 2018; Katz et al. 2019) from the *Gaia* Radial Velocity Spectrometer (RVS: Cropper et al. 2018). We generally find a very good agreement, with a zero point offset of −0.44 km s^{-1} for UVES and of −0.95 km s^{-1} for GIRAFFE, based on which we infer that *Gaia*-ESO provides systematically lower velocities. The offset is determined from the mean of the RV differences between *Gaia* and *Gaia*-ESO. We note the relatively large offset for the GIRAFFE case is based on very few measurements. Indeed, the faint magnitudes of the GIRAFFE sample make the overlap with *Gaia* RVS very small.

Individual comparisons are shown in Fig. 15, in which we plot the difference of the reported velocities from *Gaia*-ESO and *Gaia* as a function of the *Gaia* uncertainty for all stars that are contained in both datasets. While the majority of the stars have uncertainties in *Gaia* that are below 1 km s^{-1}, there are a few stars that are more uncertain. There is, however, no relation between *Gaia* RV uncertainty and apparent magnitude. The values used for the figure can be found in Table C.4.

In addition, by taking a conservative cut of (1) an uncertainty reported by *Gaia* larger than 1.8 km s^{-1} or (2) a difference in radial velocities between *Gaia* and *Gaia*-ESO larger than 1.8 km s^{-1}, we can select potential binaries. In Fig. 15, lines marking an uncertainty or difference of 1.8 km s^{-1} are shown vertically and horizontally. It is clear that some stars do not agree

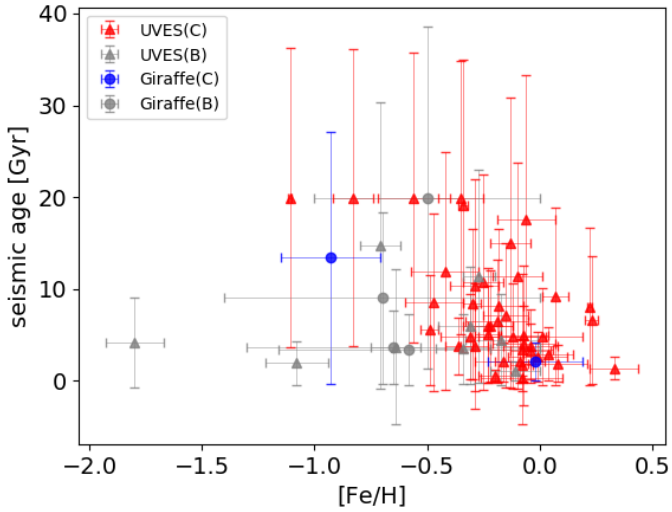

Fig. 16. Age-metallicity relation of the stars in our sample. Grey indicates the stars that are binaries (B) and coloured symbols indicate stars that are constant (C) according to our classification (see text). Error bars in age represent the mean between upper and lower age uncertainty estimate (see Paper I).

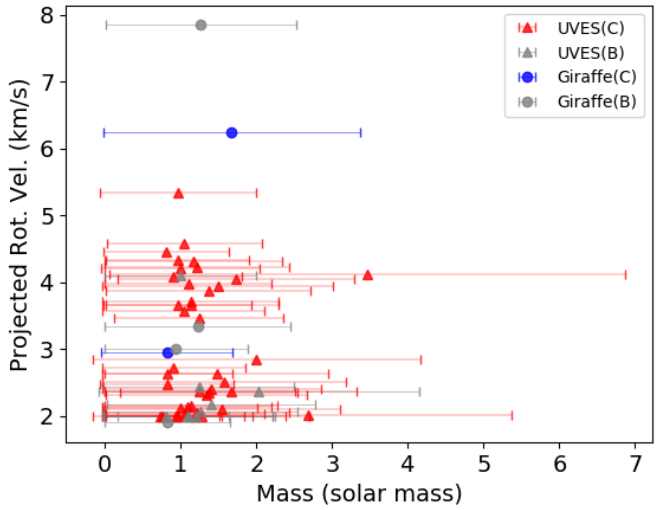

Fig. 17. Mass and projected rotational velocity ($v \sin i$) for those stars which have *Gaia* RV measurements. Error bars in mass represent the mean between upper and lower mass uncertainty estimate (see Paper I).

that well, falling outside the box marked by the lines within 1.8 km s^{-1}. These measurements might be attributed to binary stars. We note that the reported *Gaia* RV corresponds to the median of each of various RV measurements at different epochs and its uncertainty may be attributed as the variability in RV for each target. The number of transits varies a lot between each *Gaia* target, as indicated in Table C.4. A large uncertainty might be related to a large variability, which can be an indication of binary systems (see e.g. recent paper on comparisons of RV of *Gaia* and RAVE by Birko et al. 2019).

We selected our binaries as those with differences in RV of at least 1.8 km s^{-1} to account for the intrinsic variation in RV due to jitter, time-variable winds, spot visibility, and so forth, which can have a notable effect in evolved giant stars (see e.g. Carney et al. 2003, for a reference about jitter on metal-poor giants), and for differences of zero point between *Gaia*-ESO and *Gaia*, which in our case is for both datasets below 1 km s^{-1}. This gives a total of 14 potential binaries in our sample, corresponding to 15%. This value agrees with the estimate of 17% for metal-poor giants found by Carney et al. (2003) but the comparison should be taken as a reference only since both samples are selected entirely differently. Indeed, the fact that we have been able to provide parameters for the stars implies that no peculiarity in the spectra has been found. It is important to remark that this comparison is also not fully representative as *Gaia*-DR2 delivered RVs only for stars that are not double-lined spectroscopic binaries. *Gaia*-ESO, on the other hand, determines RVs for every star, regardless of their binary status. Indeed, a special working group within *Gaia*-ESO (WG14) analyses double-line spectroscopic binaries and peculiar stars, flagging every target prior to the spectral analysis (Merle et al. 2017, 2020). None of the stars in this sample have been flagged as a double-line spectroscopic binary or as a peculiar star by WG14.

It is worth commenting here that we aimed to identify and investigate the potential binaries that this sample might contain. Yet, variable RV is not the only indication that the star may be a binary. If stars have relatively small RV variation and are binaries at the same time, the companion is likely to be less massive and, so, it exhibits larger RV excursions. As a result, the lines from the companion fall in the wings of the lines of the primary star so that the spectrum appears to be that of a fast rotator, even though in reality it is a set of blended lines. This is seen also in RAVE where the spectrum of a cool dwarf appeared to be a fast rotator, but was ultimately found to be a binary. A similar effect might exist for giants.

In Fig. 16, we plot the ages and metallicities of the stars, coloured according to the respective instrument and indicating in grey the stars that are binaries according to our classification. In general, the expected age-metallicity relation is found, in which metal-poor stars are old and metal-rich stars, can have a wide range of ages. We note that the oldest stars in our sample show ages older than the Universe. As discussed in Paper I, this reflects that the prior used for the age determination was set to a maximum of 20 Gyr. When uncertainties of the results are taken into account, the oldest stars in our sample have ages within the age of the Universe. Here we plot the absolute values with the intention to study their distribution but full details can be found in Paper I.

We see that two metal-poor stars show notably young ages. For one of them, we have further RV information from *Gaia* and we note that this star is classified as a possible binary. This star, along with other binary candidates that stand out, are discussed further below.

6.1. EPIC 206101493: potentially an evolved blue straggler

As in several other recent works, some metal-poor (and alpha-enhanced) stars show unexpectedly young ages. The case of EPIC 206101493 is one example found in this K2@*Gaia*-ESO sample. Its CNAME is 22000793−1203412 and has been observed with UVES.

Such apparently young stars have been reported by Chiappini et al. (2015), and were called "young alpha-rich stars" (YAR). The observation that their high masses might imply they are young (Martig et al. 2015) and their chemical composition is more consistent with that of thick disk stars (Matsuno et al. 2018) challenges our belief that the thick disk formed a long time ago and very rapidly. It is thus very important to first test if they are (or were) binaries, as this determines whether we can or can not apply stellar models of isolated objects to constrain the

age of YAR stars. This is discussed in Jofré et al. (2016) with the help of RV monitoring of the YAR stars listed by Martig et al. (2015), and then studied in Izzard et al. (2018) with the help of stellar synthesis models which include the interaction of binary stars. It is thus interesting to see that in our K2@*Gaia*-ESO sample, EPIC 206101493, as another identified YAR star, is flagged as a binary due to its RV inconsistencies between *Gaia*-ESO and *Gaia*.

EPIC 206101493 has a UVES spectrum but since it is one of the faintest stars in our sample, its spectrum has a very low S/N (~29), this does not allow us to perform a very detailed chemical analysis to investigate its properties further, like Matsuno et al. (2018) did for a sample of these stars. In any case, at a first glance, its parameters are well-determined and its abundances are consistent with a thick disk star. It presents no evident enhancements of *s*-process or Li. This means that EPIC 206101493 is as typical a thick disk star as the other YAR stars studied in Matsuno et al. (2018), and its high mass agrees with what has been postulated by Jofré et al. (2016), namely, that it is likely a product of mass transfer.

6.2. EPIC 206322094 and EPIC 205977363: induced rotation

In Fig. 17, we show the mass and the projected rotational velocity ($v \sin i$) for our stars, following the same symbols as in previous figures. The projected rotational velocity is determined by *Gaia*-ESO alongside the radial velocity through the cross-correlation with templates. This is similar to the procedure reported by Carney et al. (2008) for their study of line broadening and rotation of metal-poor giants.

We can see that the giants in our sample have typical $v \sin i$ of 2−4 km s^{-1}, regardless of their binary status or stellar mass. There are however two stars that stand out, with $v \sin i > 6$ km s^{-1} (EPIC 206322094 $v \sin i = 7.85$ km s^{-1}; EPIC 205977363 $v \sin i = 6.25$ km s^{-1}). We note there are other stars in our sample with even higher $v \sin i$ but they are excluded from this discussion since they do not have RVs from *Gaia* DR2. While this value is higher than the rest of the stars in the sample, an abundance analysis is still possible and could be done safely.

Giants with these values of rotation have been classified as "anomalous rotators" by Tayar et al. (2015) in the APOKASC sample. They are attributed to be the cause of a recent interaction. As extensively discussed by Carney et al. (2008), the higher broadening of these stars is not likely to be due to macroturbulence. There is a trend for macroturbulence with stellar parameters which is not followed for the outlier cases. This suggests that something else might be causing the broadening. Carney et al. (2003) offer other interesting explanations for outstanding line broadening which are worthy of note.

EPIC 206322094 (CNAME 22031541−0753433) is marked as a binary, and its line broadening might be reflecting an induced rotation due to tidal interactions. *Gaia* reports an uncertainty in RV of 2.5 km s^{-1}. If the star is tidally interacting with a companion, then its orbit must be circular, which can be tested with individual RV measurements. Unfortunately, this information is still not available from *Gaia*, but a follow-up campaign on this star is ongoing and will be reported on in a separate paper.

The other star with outlying rotational velocity is EPIC 205977363 (CNAME 22063424−1530038), however, this star does not show indication of having a binary companion from its radial velocity behavior. The star could be the result of a merger (Tayar et al. 2015). Another interesting possibility for its increase in $v_{\rm rot}$ is the capture of a giant planet of few Jupiter masses due to which the star grew in size and became a red giant. It has been shown in the literature that this process can spin up giants a few km s^{-1} depending on the planet mass and the stellar radius (Privitera et al. 2016).

Siess & Livio (1999) have studied this scenario extensively, discussing possible effects that can be observed. One effect of planet capture is mass loss, which can be detected by the presence of an emission feature or asymmetry in the Hα line. Alternatively, recent discussion in the literature connects Li-rich giants to planet engulfment, where the Li abundance now unexpectedly present in the star was initially material from the planet (see e.g. discussions in Casey et al. 2016, using *Gaia* ESO data, and references therein). Although it is not entirely clear that engulfment might explain all Li-rich stars (see e.g. Aguilera-Gómez et al. 2016). Since this star is observed with the GIRAFFE setup, we do not have information about the Li abundance or the Hα profile unless a spectrum covering this wavelength domain is undertaken in the future.

6.3. EPIC 206070270 and its unseen companion

In our sample, we have one star (EPIC 206070270 – CNAME 22182719−1252466) with a notably large uncertainty in RV as determined by *Gaia* (above 8 km s^{-1}). The radial velocities measured by *Gaia*-ESO and *Gaia* differ by 25 km s^{-1}, which is consistent with the large RV uncertainty. While this is probably due to it being a binary system, without single RV measurements it is difficult to know for sure. However it is possible that this star is similar to the binaries identified in APOGEE by Price-Whelan et al. (2018). In their catalogue, they use the RV variation (and single epoch RV visit) of APOGEE giants to find the properties of possible binaries. The spectrum is further used to determine the stellar parameters and hence the mass of the giant. The stellar masses they determined cover a range that encompasses the mass of EPIC 206070270 as determined by seismology. Furthermore, they show examples of giants with high variations in RV, in some cases reaching the 25 km s^{-1} we find here. This value is also a typical value for giants found by the study of mutiplicity of giants in APOGEE by Badenes et al. (2018). If we consider that this difference is the maximum amplitude of the RV variation, and that the giant has a mass of 1.2 $M_\odot$ (see Paper I), we can use the information in Table 5 of Price-Whelan et al. (2018) to estimate that the companion of EPIC 206070270 must be a star with approximately half a solar mass.

The fact that we can constrain the mass and age of the primary with asteroseismology makes this system a potentially interesting target for follow-up studies of RV to constrain the orbits and masses of the secondary. This campaign is taking place already with the HERMES telescope in La Palma and the results will be presented elsewhere once enough RV measurements and a sufficient time span has been achieved to robustly determine the parameters of the binary system.

7. Discussion and conclusion

This work presents a detailed study to determine the stellar parameters of 90 red giant stars by combining results from spectroscopy and asteroseismology. The spectroscopy comes from data taken as part of the *Gaia*-ESO Survey in a project designed to expand the available set of calibration samples. The asteroseismology comes from data taken by K2 in the C3 field. The parameters could therefore be determined with higher accuracy due to the iterative procedure of deriving $T_{\rm eff}$ from the spectra

to be used as input for deriving $\log g$ from oscillation frequencies which is then used to re-derive $T_{\rm eff}$. A substantial change in $T_{\rm eff}$ results in just a small change in the seismic $\log g$ and so both methods are required to ensure the required accuracy in parameters.

Understanding the origin of the Galactic disks is based on a fundamental question and the answer is sought in the exploitation of stellar surveys. However, there are underlying challenges due to the inaccuracy of the stellar parameters and abundances derived for metal-poor and ancient stars. Having as many reference stars as possible in this regime is key to finding the answer.

The C3 field was chosen as it points towards the South Galactic Pole, thus favouring the inclusion of thick disk and metal-poor stars. These stars are under-represented in other seismic fields, notably the *Kepler* field (see Rendle et al. 2019 for the space distribution of the stars of K2C3 and *Kepler*). In addition, a study of chemical abundance evolution and binary detection was performed given the additional information pertaining to the masses and ages from K2, as well as the information of *Gaia* DR2.

The spectroscopic analysis was based on the combination of two distinct methods, both of which are part of the analysis procedure of the *Gaia*-ESO data. One method was based on spectrum synthesis and the other one was based on equivalent widths. Together, they allowed us to assess systematic uncertainties and reliability of results, thus providing a catalogue of spectral parameters and abundances that is accurate and not biased towards a given methodology. However, based on the intra-node abundance assessment and the corrections that were needed for seven of the elements, some possible systematic offsets in individual element abundances may remain.

The combination of seismology and spectroscopy allows us to analyse trends of abundances as a function of age, finding, as expected, that more metal-poor and α-capture element-enhanced stars are older. The addition of the *Gaia* DR2 data also allows us to identify possible binary stars: the ones that are suspiciously more massive for their metal-content, those rotating unusually faster, or those having differences in radial velocities that are larger than expected.

Catalogues of parameters and abundances for which both seismology and spectroscopy are available are few. Pioneering works in this direction are the APOKASC sample (Pinsonneault et al. 2014, 2018) and the CoRoGEE sample (Anders et al. 2017). Hawkins et al. (2016) published a catalogue with abundances for this sample considering the infrared APOGEE spectra based on temperatures determined photometrically and surface gravities from scaling relations of *Kepler*.

Another group at the forefront of this work is led by Valentini et al. (2017), who published a study similar to the one presented here (i.e. iterating between spectroscopy and seismology to reach to consistent parameters). They analysed 87 giants observed by RAVE. The spectra are of intermediate resolution ($R \sim 7000$) and cover a short wavelength range around the Ca II triplet, equivalent to *Gaia* RVS. In Valentini et al. (2017) it is possible to see how the overall stellar parameters improve when seismology is available. The group further performed a follow-up, detailed, high-resolution study of four metal-poor stars of their sample, which is presented in Valentini et al. (2019). The full RAVE catalogue will soon become public (Steinmetz et al. 2020). Targets with seismology have proven to be fundamental for the calibration of surface gravities of RAVE (Kunder et al. 2017). Similarly, *Gaia*-ESO is in the process of using CoRoT data as part of the calibration plan (Pancino et al. 2017), with the intention to publish the CoRoT@*Gaia*-ESO catalogue (Masseron et al., in prep.). In Valentini et al. (2016), the UVES and GIRAFFE stars were analysed following the same procedure as for the RAVE study.

Recently, Sharma et al. (2019) presented a study of the age and metallicity gradient of a large sample of K2 stars observed in GALAH. The study includes the same fields we analyse here, but GALAH spectra are currently not public to the entire community. The parameters and abundances are part of GALAH DR2 (Buder et al. 2018), although they were not derived using the seismic parameters as a prior.

In addition, Nissen et al. (2017) published a catalogue of parameters and abundances derived self consistently with seismology using high-resolution optical spectra of HARPS-N for a sample of solar twins in *Kepler*. Finally, Morel et al. (2014) presents the study of high resolution optical spectra of 20 red giants that were targeted by CoRoT.

Our work is a novel contribution as the largest high-resolution optical catalogue with parameters and abundances derived homogeneously. We have taken advantage of forefront spectroscopic and astereoseismic methodologies, along with the sample targets of the outer regions of the disk to capture sought-after old and metal-poor stars. Our catalogue of parameters and abundances is available at the CDS, including the results at a line-by-line and method-by-method level to ensure reproducibility (see Tables B.1 and B.2 for list of columns). The spectra are public via the ESO archives. In addition, the chosen field of K2 was selected so that our catalogue would include more thick disk stars than other samples for which spectroscopy and astereoseismology are available.

While the interior of stars gives us clues as to their evolutionary phase (based on mass and age), the exterior of stars tell us about their formation site (chemistry), and stellar motion (radial velocities). Individually, these latter two types of data can provide the means to calibrate the analysis of large samples of stars, however, the combination of both provides an even more powerful basis upon which to make a more effective and robust analysis that is key to constraining models of galactic formation and evolution.

Acknowledgements. The authors thank the International Space Science Institute in Bern (ISSI) and Beijing (ISSI-BJ) for supporting and hosting the meetings of the International Team on "AsteroStep" and "Libraries of 2020", respectively, during which the discussions leading and contributing to this publication were initiated and held. PJ acknowledges support of FONDECYT Iniciación Grant Number 11170174. RS acknowledges support from the National Science Centre (2014/15/B/ST9/03981). A.G., A.K. and U.H. acknowledge support from the Swedish National Space Agency (SNSA/Rymdstyrelsen). T.B. was funded by the project grant "The New Milky Way" from the Knut and Alice Wallenberg Foundation. This work is based on data products from observations made with ESO Telescopes at the La Silla Paranal Observatory under programme ID 188.B-3002. These data products have been processed by the Cambridge Astronomy Survey Unit (CASU) at the Institute of Astronomy, University of Cambridge, and by the FLAMES/UVES reduction team at INAF/Osservatorio Astrofisico di Arcetri. These data have been obtained from the *Gaia*-ESO Survey Data Archive, prepared and hosted by the Wide Field Astronomy Unit, Institute for Astronomy, University of Edinburgh, which is funded by the UK Science and Technology Facilities Council. This work was partly supported by the European Union FP7 programme through ERC grant number 320360 and by the Leverhulme Trust through grant RPG-2012-541. We acknowledge the support from INAF and Ministero dell' Istruzione, dell' Università' e della Ricerca (MIUR) in the form of the grant "Premiale VLT 2012". The results presented here benefit from discussions held during the *Gaia*-ESO workshops and conferences supported by the ESF (European Science Foundation) through the GREAT Research Network Programme. The authors thank the anonymous referee for the useful comments that improved the manuscript.

References

Aguilera-Gómez, C., Chanamé, J., Pinsonneault, M. H., & Carlberg, J. K. 2016, ApJ, 829, 127
Anders, F., Chiappini, C., Rodrigues, T. S., et al. 2017, A&A, 597, A30
Badenes, C., Mazzola, C., Thompson, T. A., et al. 2018, ApJ, 854, 147
Baglin, A., Auvergne, M., Barge, P., et al. 2006, in The CoRoT Mission Pre-Launch Status – Stellar Seismology and Planet Finding, eds. M. Fridlund, A. Baglin, J. Lochard, & L. Conroy, ESA Spec. Publ., 1306, 33
Bard, A., & Kock, M. 1994, A&A, 282, 1014
Bard, A., Kock, A., & Kock, M. 1991, A&A, 248, 315
Biemont, E., Grevesse, N., Hannaford, P., & Lowe, R. M. 1981, ApJ, 248, 867
Biémont, É., Blagoev, K., Engström, L., et al. 2011, MNRAS, 414, 3350
Birko, D., Zwitter, T., Grebel, E. K., et al. 2019, AJ, 158, 155
Blackwell, D. E., Shallis, M. J., & Simmons, G. J. 1980, A&A, 81, 340
Blanco-Cuaresma, S., Soubiran, C., Heiter, U., & Jofré, P. 2014, A&A, 569, A111
Borucki, W. J., Koch, D., Basri, G., et al. 2010, Science, 327, 977
Bressan, A., Marigo, P., Girardi, L., et al. 2012, MNRAS, 427, 127
Buder, S., Asplund, M., Duong, L., et al. 2018, MNRAS, 478, 4513
Buder, S., Lind, K., Ness, M. K., et al. 2019, A&A, 624, A19
Cantat-Gaudin, T., Donati, P., Pancino, E., et al. 2014, A&A, 562, A10
Carney, B. W., Latham, D. W., Stefanik, R. P., Laird, J. B., & Morse, J. A. 2003, AJ, 125, 293
Carney, B. W., Latham, D. W., Stefanik, R. P., & Laird, J. B. 2008, AJ, 135, 196
Carpenter, J. M. 2001, AJ, 121, 2851
Casey, A. R., Ruchti, G., Masseron, T., et al. 2016, MNRAS, 461, 3336
Chiappini, C., Anders, F., Rodrigues, T. S., et al. 2015, A&A, 576, L12
Cirasuolo, M., & MOONS Consortium 2016, in Multi-Object Spectroscopy in the Next Decade: Big Questions, Large Surveys, and Wide Fields, eds. I. Skillen, M. Balcells, & S. Trager, ASP Conf. Ser., 507, 109
Cowley, C. R., & Corliss, C. H. 1983, MNRAS, 203, 651
Cropper, M., Katz, D., Sartoretti, P., et al. 2018, A&A, 616, A5
Dalton, G., Trager, S. C., Abrams, D. C., et al. 2012, in Ground-based and Airborne Instrumentation for Astronomy IV, Proc. SPIE, 8446, 84460P
de Jong, R. S., Agertz, O., Berbel, A. A., et al. 2019, The Messenger, 175, 3
Den Hartog, E. A., Lawler, J. E., Sneden, C., & Cowan, J. J. 2003, ApJS, 148, 543
Den Hartog, E. A., Lawler, J. E., Sobeck, J. S., Sneden, C., & Cowan, J. J. 2011, ApJS, 194, 35
De Silva, G. M., Freeman, K. C., Bland-Hawthorn, J., et al. 2015, MNRAS, 449, 2604
Drozdowski, R., Ignaciuk, M., Kwela, J., & Heldt, J. 1997, Z. Phys. D At. Mol. Clust., 41, 125
Elias, J. H., Frogel, J. A., Matthews, K., & Neugebauer, G. 1982, AJ, 87, 1029
Fuhr, J. R., Martin, G. A., & Wiese, W. L. 1988, Journal of Physical and Chemical Reference Data (New York: American Institute of Physics (AIP) and American Chemical Society), 17
Gaia Collaboration (Brown, A. G. A., et al.) 2018, A&A, 616, A1
Garz, T. 1973, A&A, 26, 471
Gavel, A., Gruyters, P., Korn, A., Lind, K., & Nordlander, T. 2020, A&A, 629, A74
Gilmore, G., Randich, S., Asplund, M., et al. 2012, The Messenger, 147, 25
Gustafsson, B., Edvardsson, B., Eriksson, K., et al. 2008, A&A, 486, 951
Hannaford, P., Lowe, R. M., Grevesse, N., Biemont, E., & Whaling, W. 1982, ApJ, 261, 736
Hawkins, K., Masseron, T., Jofré, P., et al. 2016, A&A, 594, A43
Heiter, U., Jofré, P., Gustafsson, B., et al. 2015, A&A, 582, A49
Heiter, U., Lind, K., Bergemann, M., et al. 2020, A&A, submitted
Houdashelt, M. L., Bell, R. A., & Sweigart, A. V. 2000, AJ, 119, 1448
Howell, S. B., Sobeck, C., Haas, M., et al. 2014, PASP, 126, 398
Izzard, R. G., Preece, H., Jofre, P., et al. 2018, MNRAS, 473, 2984
Jofré, P., Heiter, U., Soubiran, C., et al. 2014, A&A, 564, A133
Jofré, P., Jorissen, A., Van Eck, S., et al. 2016, A&A, 595, A60
Jofré, P., Heiter, U., Tucci Maia, M., et al. 2018, Res. Notes Am. Astron. Soc., 2, 152
Jofré, P., Heiter, U., & Soubiran, C. 2019, ARA&A, 57, 571
Katz, D., Sartoretti, P., Cropper, M., et al. 2019, A&A, 622, A205
Khan, S., Miglio, A., Mosser, B., et al. 2019, The Gaia Universe, 13
Kunder, A., Kordopatis, G., Steinmetz, M., et al. 2017, AJ, 153, 75
Kurucz, R. L. 2007, Robert L. Kurucz On-line Database of Observed and Predicted Atomic Transitions
Kurucz, R. L. 2008, Robert L. Kurucz On-line Database of Observed and Predicted Atomic Transitions
Kurucz, R. L. 2009, Robert L. Kurucz On-line Database of Observed and Predicted Atomic Transitions
Kurucz, R. L. 2010, Robert L. Kurucz On-line Database of Observed and Predicted Atomic Transitions
Kurucz, R. L. 2011, Robert L. Kurucz On-line Database of Observed and Predicted Atomic Transitions
Kurucz, R. L. 2012, Robert L. Kurucz On-line Database of Observed and Predicted Atomic Transitions
Kurucz, R. L. 2013, Robert L. Kurucz On-line Database of Observed and Predicted Atomic Transitions
Lambert, D. L., Mallia, E. A., & Warner, B. 1969, MNRAS, 142, 71
Lawler, J. E., & Dakin, J. T. 1989, J. Opt. Soc. Am. B Opt. Phys., 6, 1457
Lawler, J. E., Bonvallet, G., & Sneden, C. 2001a, ApJ, 556, 452
Lawler, J. E., Wickliffe, M. E., den Hartog, E. A., & Sneden, C. 2001b, ApJ, 563, 1075
Lawler, J. E., Sneden, C., Cowan, J. J., Ivans, I. I., & Den Hartog, E. A. 2009, ApJS, 182, 51
Lawler, J. E., Guzman, A., Wood, M. P., Sneden, C., & Cowan, J. J. 2013, ApJS, 205, 11
Lindegren, L., Hernández, J., Bombrun, A., et al. 2018, A&A, 616, A2
Ljung, G., Nilsson, H., Asplund, M., & Johansson, S. 2006, A&A, 456, 1181
Magrini, L., Randich, S., Friel, E., et al. 2014, FAMA: Fast Automatic MOOG Analysis
Majewski, S. R., Schiavon, R. P., Frinchaboy, P. M., et al. 2017, AJ, 154, 94
Martig, M., Rix, H.-W., Silva Aguirre, V., et al. 2015, MNRAS, 451, 2230
Masseron, T. 2006, PhD Thesis, Observatoire de Paris, France
Matsuno, T., Yong, D., Aoki, W., & Ishigaki, M. N. 2018, ApJ, 860, 49
McCall, M. L. 2004, AJ, 128, 2144
Meggers, W. F., Corliss, C. H., & Scribner, B. F. 1975, Tables of Spectral-line Intensities. Part I, II_- Arranged by Elements, 145
Merle, T., Van Eck, S., Jorissen, A., et al. 2017, A&A, 608, A95
Merle, T., Van der Swaelmen, M., Van Eck, S., et al. 2020, A&A, 635, A155
Miglio, A., Chiappini, C., Mosser, B., et al. 2017, Astron. Nachr., 338, 644
Miles, B. M., & Wiese, W. L. 1969, At. Data, 1, 1
Mints, A., & Hekker, S. 2017, A&A, 604, A108
Morel, T., & Miglio, A. 2012, MNRAS, 419, L34
Morel, T., Miglio, A., Lagarde, N., et al. 2014, A&A, 564, A119
Nissen, P. E., Silva Aguirre, V., Christensen-Dalsgaard, J., et al. 2017, A&A, 608, A112
Nitz, D. E., Wickliffe, M. E., & Lawler, J. E. 1998, ApJS, 117, 313
O'Brian, T. R., Wickliffe, M. E., Lawler, J. E., Whaling, W., & Brault, J. W. 1991, J. Opt. Soc. Am. B Opt. Phys., 8, 1185
Pancino, E., Lardo, C., Altavilla, G., et al. 2017, A&A, 598, A5
Pinnington, E. H., Ji, Q., Guo, B., et al. 1993, Can. J. Phys., 71, 470
Pinsonneault, M. H., Elsworth, Y., Epstein, C., et al. 2014, ApJS, 215, 19
Pinsonneault, M. H., Elsworth, Y. P., Tayar, J., et al. 2018, ApJS, 239, 32
Piskunov, N., & Valenti, J. A. 2017, A&A, 597, A16
Pitts, R. E., & Newsom, G. H. 1986, J. Quant. Spectr. Radiat. Transf., 35, 383
Plez, B. 2012, Astrophysics Source Code Library [record ascl:1205.004]
Price-Whelan, A. M., Hogg, D. W., Rix, H.-W., et al. 2018, AJ, 156, 18
Privitera, G., Meynet, G., Eggenberger, P., et al. 2016, A&A, 593, A128
Prugniel, P., & Soubiran, C. 2001, A&A, 369, 1048
Ralchenko, Y., Kramida, A., Reader, J., & NIST ASD Team 2010, NIST Atomic Spectra Database (ver. 4.0.0) [Online]
Ramírez, I., & Meléndez, J. 2005, ApJ, 626, 465
Rendle, B. M., Miglio, A., Chiappini, C., et al. 2019, MNRAS, 490, 4465
Ryabchikova, T. A., Hill, G. M., Landstreet, J. D., Piskunov, N., & Sigut, T. A. A. 1994, MNRAS, 267, 697
Sartoretti, P., Katz, D., Cropper, M., et al. 2018, A&A, 616, A6
Schlegel, D. J., Finkbeiner, D. P., & Davis, M. 1998, ApJ, 500, 525
Seaton, M. J., Yan, Y., Mihalas, D., & Pradhan, A. K. 1994, MNRAS, 266, 805
Sharma, S., Stello, D., Bland-Hawthorn, J., et al. 2019, MNRAS, 490, 5335
Siess, L., & Livio, M. 1999, MNRAS, 308, 1133
Sigut, T. A. A., & Landstreet, J. D. 1990, MNRAS, 247, 611
Skrutskie, M. F., Cutri, R. M., Stiening, R., et al. 2006, AJ, 131, 1163
Smiljanic, R., Korn, A. J., Bergemann, M., et al. 2014, A&A, 570, A122
Smith, G. 1981, A&A, 103, 351
Smith, G. 1988, J. Phys. B At. Mol. Phys., 21, 2827
Smith, G., & O'Neill, J. A. 1975, A&A, 38, 1
Smith, G., & Raggett, D. S. J. 1981, J. Phys. B At. Mol. Phys., 14, 4015
Sneden, C., Bean, J., Ivans, I., Lucatello, S., & Sobeck, J. 2012, Astrophysics Source Code Library [record ascl:1202.009]
Sobeck, J. S., Lawler, J. E., & Sneden, C. 2007, ApJ, 667, 1267
Soubiran, C., Le Campion, J.-F., Brouillet, N., & Chemin, L. 2016, A&A, 591, A118
Steinmetz, M., Matijevic, G., Enke, H., et al. 2020, AJ, 160, 82
Stetson, P. B., & Pancino, E. 2008, PASP, 120, 1332
Szeto, K., Simons, D., Bauman, S., et al. 2018, in Society of Photo-Optical Instrumentation Engineers (SPIE) Conference Series, Proc. SPIE, 10700, 107001N
Tayar, J., Ceillier, T., García-Hernández, D. A., et al. 2015, ApJ, 807, 82

Valenti, J. A., & Piskunov, N. 1996, A&AS, 118, 595
Valentini, M., Chiappini, C., Miglio, A., et al. 2016, Astron. Nachr., 337, 970
Valentini, M., Chiappini, C., Davies, G. R., et al. 2017, A&A, 600, A66
Valentini, M., Chiappini, C., Bossini, D., et al. 2019, A&A, 627, A173
Wallace, L., & Hinkle, K. 2009, ApJ, 700, 720
Warner, B. 1968, MNRAS, 140, 53
Wickliffe, M. E., & Lawler, J. E. 1997, ApJS, 110, 163
Wiese, W. L., Smith, M. W., & Miles, B. M. 1969, Atomic Transition Probabilities. Vol. 2: Sodium Through Calcium. A Critical Data Compilation (US Government Printing Office)
Wood, M. P., Lawler, J. E., Sneden, C., & Cowan, J. J. 2013, ApJS, 208, 27
Worley, C. C., de Laverny, P., Recio-Blanco, A., Hill, V., & Bijaoui, A. 2016, A&A, 591, A81
Zinn, J. C., Pinsonneault, M. H., Huber, D., & Stello, D. 2019, ApJ, 878, 136

[1] Institute of Astronomy, University of Cambridge, Madingley Road, Cambridge CB3 0HA, UK
e-mail: ccworley@ast.cam.ac.uk
[2] Núcleo de Astronomía, Universidad Diego Portales, Av. Ejército 441, Santiago de Chile, Chile
e-mail: paula.jofre@mail.udp.cl
[3] School of Physics and Astronomy, University of Birmingham, Birmingham B15 2TT, UK
[4] INAF – Osservatorio Astrofisico di Arcetri, Largo E. Fermi 5, 50125 Florence, Italy
[5] Max-Planck Institut für Astronomie, Königstuhl 17, 69117 Heidelberg, Germany
[6] Observational Astrophysics, Division of Astronomy and Space Physics, Department of Physics and Astronomy, Uppsala University, Box 516, 751 20 Uppsala, Sweden
[7] Nicolaus Copernicus Astronomical Center, Polish Academy of Sciences, ul. Bartycka 18, 00-716 Warsaw, Poland
[8] GEPI, Observatoire de Paris, CNRS, Université Paris Diderot, 5 Place Jules Janssen, 92190 Meudon, France
[9] INAF – Padova Observatory, Vicolo dell'Osservatorio 5, 35122 Padova, Italy
[10] Dipartimento di Fisica e Astronomia, Sezione Astrofisica, Universitá di Catania, Via S. Sofia 78, 95123 Catania, Italy
[11] INAF – Osservatorio di Astrofisica e Scienza dello Spazio di Bologna, Via Gobetti 93/3, 40129 Bologna, Italy
[12] Lund Observatory, Department of Astronomy and Theoretical Physics, Box 43, 221 00 Lund, Sweden
[13] Instituto de Astrofísica de Andalucía-CSIC, Apdo. 3004, 18080 Granada, Spain
[14] Instituto de Astrofísica e Ciências do Espaço, Universidade do Porto, CAUP, Rua das Estrelas, 4150-762 Porto, Portugal
[15] Departamento de Ciencias Fisicas, Universidad Andres Bello, Fernandez Concha 700, Las Condes, Santiago, Chile
[16] Dipartimento di Fisica e Astronomia, Università di Padova, Vicolo dell'Osservatorio 3, 35122 Padova, Italy
[17] European Southern Observatory, Alonso de Cordova, 3107 Vitacura, Santiago de Chile, Chile
[18] Faculty of Mathematics and Physics, University of Ljubljana, Jadranska 19, 1000 Ljubljana, Slovenia
[19] Instituto de Física y Astronomía, Facultad de Ciencias, Universidad de Valparaíso, Av. Gran Bretaña 1111, 5030 Casilla, Valparaíso, Chile
[20] Laboratoire d'astrophysique, Ecole Polytechnique Fédérale de Lausanne (EPFL), Observatoire de Sauverny, 1290 Versoix, Switzerland
[21] Department of Astronomy, Stockholm University, AlbaNova, Roslagstullbacken 21, 10691 Stockholm, Sweden
[22] Núcleo Milenio de Formación Planetaria – NPF, Universidad de Valparaíso, Av. Gran Bretaña 1111, Valparaíso, Chile

Appendix A: Intra-node chemical species corrections

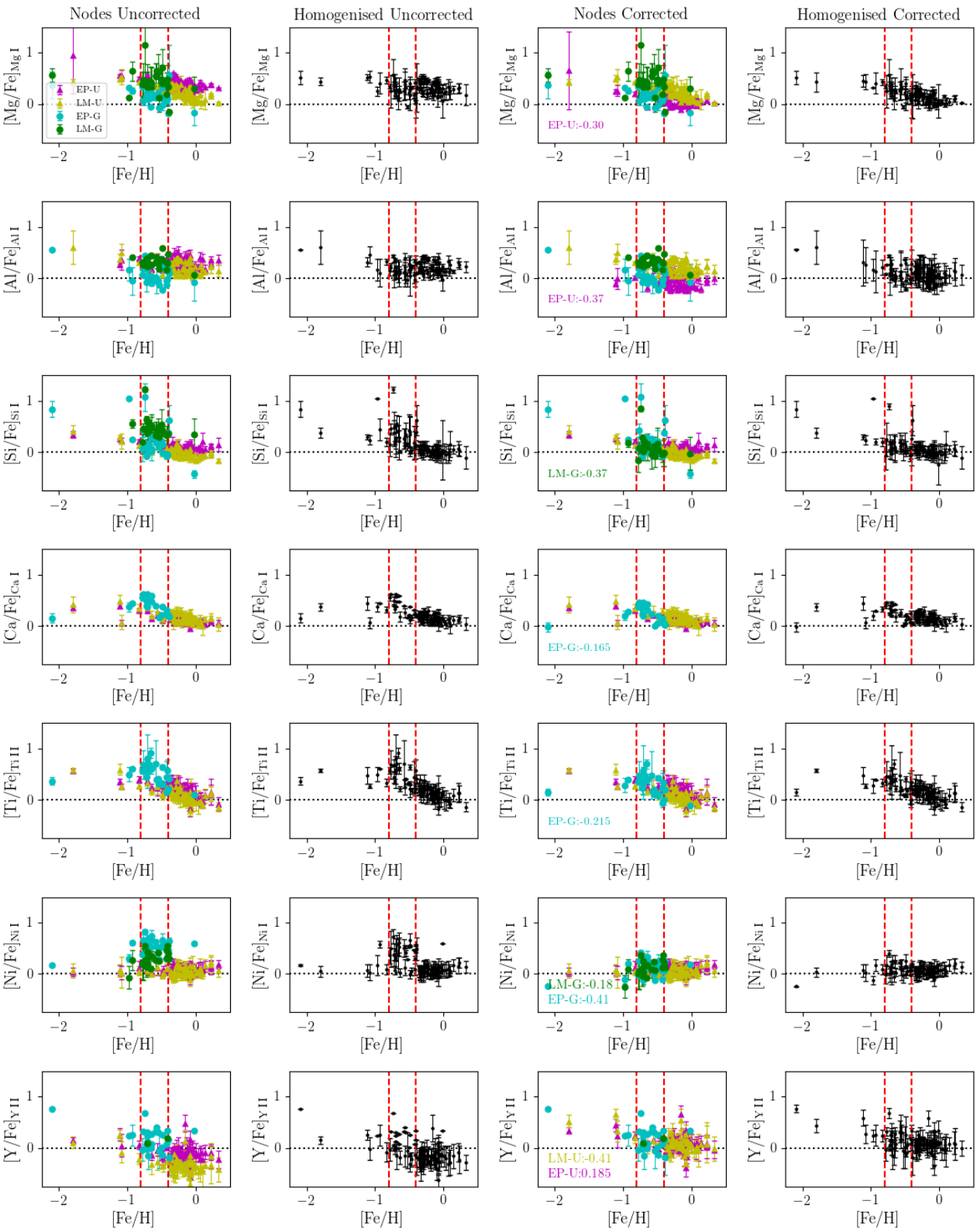

Fig. A.1. Chemical abundances of [X/Fe] against [Fe/H] for Mg I, Al I, Si I, Ca I, Ti II, Ni I, and Y II for the K2@*Gaia*-ESO stars derived based on the final stellar parameters. *First column*: node (EP,LM) and instrument (U, G) results as specified in the legend. The [Fe/H] overlap is bounded by dashed red lines. The errorbars are the line-by-line values per star per node uncertainties. *Second column*: homogenised abundances without per node corrections. *Third column*: node values with corrections applied. *Fourth column*: final homogenised values.

Appendix B: K2@*Gaia*-ESO catalogue columns

Table B.1. Columns contained in the K2@*Gaia*-ESO Catalogue.

Column name	Description
CNAME	*Gaia*-ESO object name from coordinates
EPIC_ID	K2 unique identifier
INSTRUMENT	Instrument used for spectroscopic observation
SNR	Signal-to-noise ratio of *Gaia*-ESO spectrum
GAIADR2_ID	*Gaia* DR2 Source Identifier
GAIADR2_MAGG	*Gaia* DR2 G band magnitude [Vega]
GAIADR2_PARAL	*Gaia* DR2 Parallax
GAIADR2_PARAL_ERR	Uncertainty on GAIADR2_PARAL
TEFF	Spectroscopic effective temperature
TEFF_ERR	Error on TEFF
LOGG	Seismic surface gravity
LOGG_ERR	Error on LOGG
FEH	Spectroscopic metallicity
FEH_ERR	Error on FEH
XI	Spectroscopic microturbulence
XI_ERR	Uncertainty on XI
NODE_RES	Node results used for final parameters
GAIADR2_VRAD	*Gaia* DR2 radial velocity
GAIADR2_VRAD_ERR	Uncertainty on GAIADR2_VRAD
VRAD	Radial Velocity from *Gaia*-ESO
VRAD_ERR	Uncertainty on VRAD
VSINI	Rotational Velocity from *Gaia*-ESO
BIN_FLAG	Binary detected? 0 = no; 1 = potential, −1 = NA
NA1	Neutral Sodium Abundance [Na/Fe]
NA1_ERR	Uncertainty on NA1
MG1	Neutral Magnesium Abundance [Mg/Fe]
MG1_ERR	Uncertainty on MG1
AL1	Neutral Aluminium Abundance [Al/Fe]
AL1_ERR	Uncertainty on AL1
SI1	Neutral Silicon Abundance [Si/Fe]
SI1_ERR	Uncertainty on SI1
SI2	Ionised Silicon Abundance [Si/Fe]
SI2_ERR	Uncertainty on SI2
CA1	Neutral Calcium Abundance [Ca/Fe]
CA1_ERR	Uncertainty on CA1
CA2	Ionised Calcium Abundance [Ca/Fe]
CA2_ERR	Uncertainty on CA2
SC1	Neutral Scandium Abundance [Sc/Fe]
SC1_ERR	Uncertainty on SC1
SC2	Ionised Scandium Abundance [Sc/Fe]
SC2_ERR	Uncertainty on SC2
TI1	Neutral Titanium Abundance [Ti/Fe]
TI1_ERR	Uncertainty on TI1
TI2	Ionised Titanium Abundance [Ti/Fe]
TI2_ERR	Uncertainty on TI2
V1	Neutral Vanadium Abundance [V/Fe]
V1_ERR	Uncertainty on V1
CR1	Neutral Chromium Abundance [Cr/Fe]
CR1_ERR	Uncertainty on CR1
CR2	Ionised Chromium Abundance [Cr/Fe]
CR2_ERR	Uncertainty on CR2
MN1	Neutral Manganese Abundance [Mn/Fe]
MN1_ERR	Uncertainty on MN1
FE1	Neutral Iron Abundance [Fe/H]
FE1_ERR	Uncertainty on FE1
FE2	Ionised Iron Abundance [Fe/H]
FE2_ERR	Uncertainty on FE2
CO1	Neutral Cobalt Abundance [Co/Fe]
CO1_ERR	Uncertainty on CO1
NI1	Neutral Nickel Abundance [Ni/Fe]
NI1_ERR	Uncertainty on NI1
CU1	Neutral Copper Abundance [Cu/Fe]
CU1_ERR	Uncertainty on CU1
ZN1	Neutral Zinc Abundance [Zn/Fe]
ZN1_ERR	Uncertainty on ZN1
Y2	Ionised Yttrium Abundance [Y/Fe]
Y2_ERR	Uncertainty on Y2
ZR1	Neutral Zirconium Abundance [Zr/Fe]
ZR1_ERR	Uncertainty on ZR1
ZR2	Ionised Zirconium Abundance [Zr/Fe]
ZR2_ERR	Uncertainty on ZR2
BA2	Ionised Barium Abundance [Ba/Fe]
BA2_ERR	Uncertainty on BA2
LA2	Ionised Lanthanum Abundance [La/Fe]
LA2_ERR	Uncertainty on LA2
CE2	Ionised Cerium Abundance [Ce/Fe]
CE2_ERR	Uncertainty on CE2
ND2	Ionised Neodymium Abundance [Nd/Fe]
ND2_ERR	Uncertainty on ND2
EU2	Ionised Europium Abundance [Eu/Fe]
EU2_ERR	Uncertainty on EU2
MASS	Seismic stellar mass
MASS_ERR	Error on MASS
AGE	Seismic stellar age
AGE_ERR	Error on AGE

Notes. Full table is available at the CDS.

Table B.2. Columns for line-by-line per node per CNAME abundance analysis.

Column name	Description
NODE	*Gaia*-ESO node name
CNAME	*Gaia*-ESO object name from coordinates
INSTRUMENT	Spectroscopic instrument
LAMBDA	Wavelength of spectral line
ELEMENT	Atomic element name
ION	Species: 1 = neutral, 2 = ionised
EXC_POT	Excitation potential
LOG_GF	Oscillator strength
REFERENCE	Atomic information reference
EW	Measured equivalent width
ABUND	Measured abundance as log(eps)
ABUND_ERR	Error on ABUND
ABUND_UPPER	Limit flag: 0 = Detection; 1 = Upper limit
MEAS_TYPE	SS: Spectrum Synthesis; EW: Equivalent Widths

Notes. Full table is available at the CDS.

Appendix C: K2@*Gaia*-ESO chemical abundance distributions

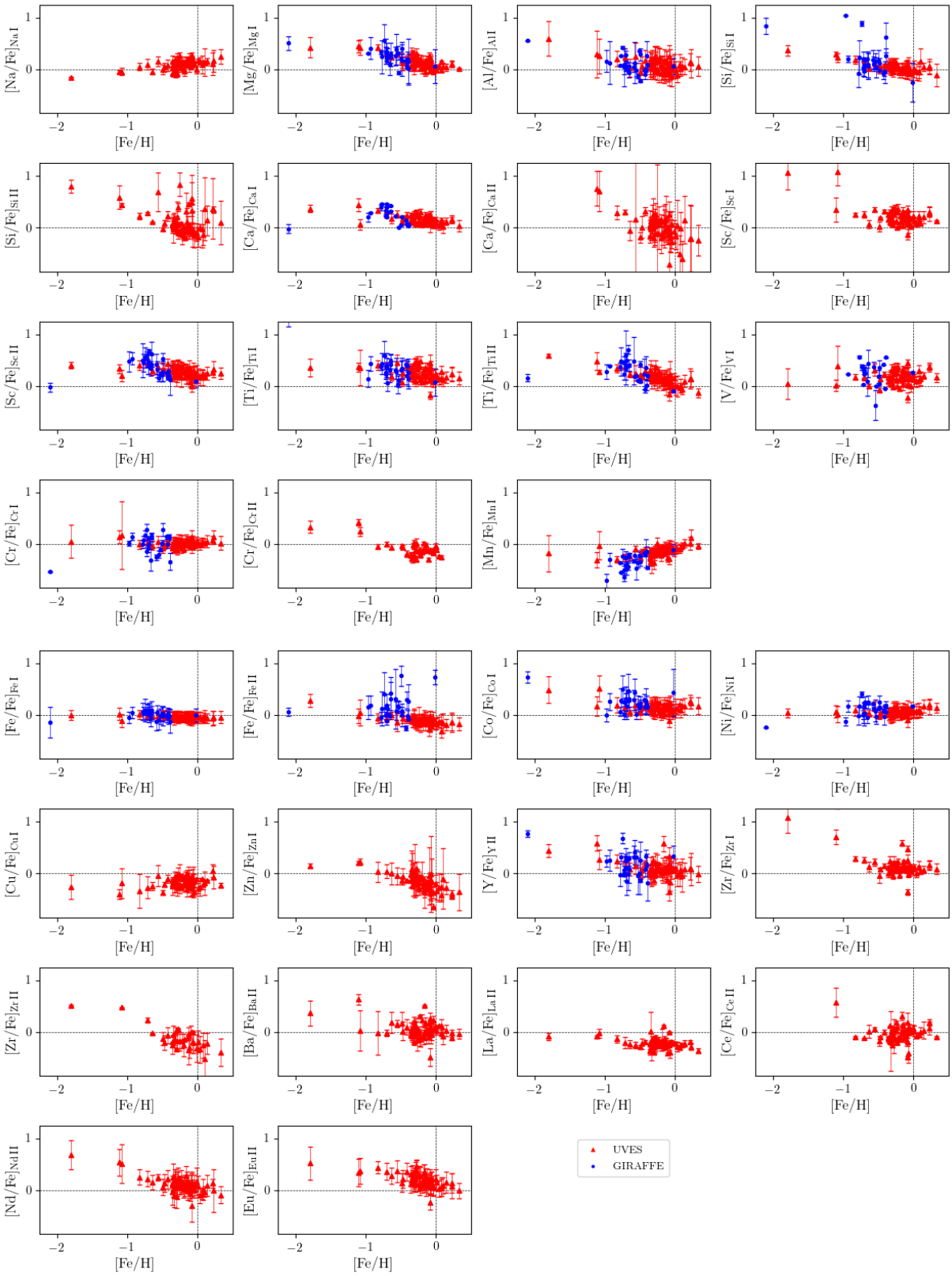

Fig. C.1. Chemical abundances of [X/Fe] against [Fe/H] for the K2@*Gaia*-ESO stars derived based on the final stellar parameters. The UVES stars are red triangles, the GIRAFFE stars are blue circles. [Fe/H] = 0 and [X/Fe] = 0 are indicated as dashed lines.

Table C.1. 90 stars analysed in the K2 *Gaia*-ESO special project.

			IRFM	Prelim. spec.			Prelim. seis.	Initial spec. (iSpec)		Initial seis.
CNAME	EPIC ID	Instrument	$T_{\rm eff}$ [K]	$T_{\rm eff}$ [K]	$\log g$ [log(cm s^{-2})]	[Fe/H]	$\log g$ [log(cm s^{-2})]	$T_{\rm eff}$ [K]	[Fe/H]	$\log g$ [log(cm s^{-2})]
22013945−0909229	K2_206238956	UVES*	4541	4607	3.15	0.18	2.98	4721	0.25	3.04
22032202−0829154	K2_206283732	UVES*	5125	5089	3.84	0.23	2.45	5421	0.29	2.49
22050764−0840472	K2_206270701	UVES*	4892	4935	3.31	−0.26	3.07	4992	−0.24	3.11
22052114−0848002	K2_206262569	UVES*	4697	4762	2.66	−0.32	2.41	4820	−0.32	2.46
22052550−0854435	K2_206255139	UVES*	4756	4776	2.43	−0.29	2.31	4876	−0.28	2.36
22055148−0840028	K2_206271510	UVES*	4593	4689	3.00	−0.29	2.63	4800	−0.21	2.68
22065112−1504580	K2_205991117	UVES*	4798	4899	1.96	−1.68	1.99	4602	−1.89	2.01
22071748−1455524	K2_205996255	UVES*	4641	4707	2.74	−0.26	2.51	4795	−0.22	2.56
22072959−1530438	K2_205977024	UVES*	4884	4950	3.33	−0.05	3.01	5051	−0.05	3.05
22075605−1535081	K2_205974551	UVES*	4669	4757	3.06	0.00	2.81	4882	0.05	2.85
22122727−0719010	K2_206357934	UVES*	4358	4412	2.43	−0.16	2.14	4531	−0.18	2.20
22172260−1346134	K2_206037023	UVES*	4682	4783	2.74	−0.66	2.46	4774	−0.62	2.50
22174405−1338287	K2_206041863	UVES*	4706	4736	2.89	−0.28	2.63	4853	−0.27	2.68
22175268−1344270	K2_206038132	UVES*	4719	4739	2.44	−0.31	2.27	4808	−0.32	2.32
22182719−1252466	K2_206070270	UVES*	4637	4637	2.82	−0.09	2.55	4731	−0.06	2.60
22185037−1257588	K2_206066993	UVES*	4477	4543	2.74	−0.08	2.42	4620	−0.06	2.48
22250508−1341415	K2_206039882	UVES*	4708	4689	2.67	−0.06	2.57	4781	−0.07	2.62
22254071−1431281	K2_206010465	UVES*	4736	4763	2.81	−0.29	2.25	4914	−0.29	2.30
22271794−0747334	K2_206328599	UVES*	4776	4850	3.11	−0.19	2.79	4890	−0.21	2.83
22291753−0806290	K2_206308617	UVES*	4577	4698	2.91	−0.27	2.60	4768	−0.25	2.65
22292970−0713347	K2_206363486	UVES*	4716	4771	2.51	−0.21	2.36	4928	−0.18	2.41
21563608−1202424	K2_206102116	UVES	4682	4668	2.76	−0.48	2.88	4842	−0.21	2.93
21590887−1159078	K2_206104478	UVES	4592	4503	2.23	−0.34	2.30	4756	−0.02	2.37
22000793−1203412	K2_206101493	UVES	5228	5317	2.40	−1.31	2.40	5309	−1.08	2.42
22013369−1141245	K2_206115828	UVES	4555	4552	2.21	−0.66	2.18	4719	−0.37	2.24
22015504−1153022	K2_206108556	UVES	4668	4603	2.22	−0.51	2.43	4848	−0.21	2.49
22021848−1139147	K2_206117168	UVES	4511	4428	2.06	−0.24	2.31	4787	0.11	2.39
22033684−1449366	K2_205999925	UVES	4741	4727	2.37	−0.56	2.33	4937	−0.29	2.38
22035226−1457037	K2_205995590	UVES	4954	4880	3.09	−0.50	3.22	5077	−0.20	3.26
22062074−0809079	K2_206305769	UVES	4611	4564	2.51	−0.25	2.59	4771	−0.01	2.65
22072768−1440392	K2_206005223	UVES	...	4468	2.41	−0.24	2.54	4690	0.03	2.60
22074607−1055493	K2_206144769	UVES	4720	4706	2.20	−1.32	2.22	4731	−1.12	2.27
22074730−1059405	K2_206142277	UVES	4678	4657	2.59	−0.31	2.73	4898	0.03	2.79
22083624−0948555	K2_206196672	UVES	4754	4563	2.35	0.11	2.68	4992	0.41	2.75
22085850−0608204	K2_206429616	UVES	4727	4758	2.41	−0.53	2.32	4891	−0.26	2.37
22091180−0944335	K2_206201030	UVES	4859	4753	3.17	−0.46	3.30	4955	−0.15	3.35
22092416−0610474	K2_206427237	UVES	...	4707	2.28	−0.31	2.45	4766	0.02	2.50
22092886−0617515	K2_206420120	UVES	4631	4584	2.69	−0.45	2.82	4928	−0.14	2.88
22094505−1051031	K2_206147901	UVES	4219	4165	1.38	−0.80	1.53	4380	−0.48	1.61
22102197−0923157	K2_206223471	UVES	4855	4824	2.34	−0.42	2.47	4983	−0.15	2.51
22104061−1125284	K2_206125783	UVES	4499	4406	2.08	−0.35	2.40	4702	0.03	2.47
22105372−0956597	K2_206188891	UVES	4665	4576	2.43	−0.63	2.50	4811	−0.31	2.57
22114557−0957433	K2_206188223	UVES	4871	4804	3.06	−0.38	3.11	4981	−0.11	3.16
22130580−0658576	K2_206378264	UVES	4462	4345	1.94	−0.42	2.29	4661	−0.07	2.37
22153043−0617291	K2_206420485	UVES	4896	4880	2.38	−0.62	2.36	4960	−0.46	2.40
22154837−0628154	K2_206409829	UVES	4737	4786	2.49	−0.83	2.38	4904	−0.56	2.43
22172723−1633039	K2_205944548	UVES	4482	4532	1.98	−0.98	1.90	4649	−0.76	1.95
22195215−1234594	K2_206081428	UVES	4641	4570	2.28	−0.40	2.30	4873	−0.02	2.36
22204635−1245072	K2_206075005	UVES	4794	4688	2.92	−0.18	3.13	4955	0.20	3.19
22235003−1422417	K2_206015475	UVES	4673	4567	3.07	0.17	3.07	4868	0.25	3.14
22235672−1428420	K2_206012087	UVES	4713	4634	2.48	−0.46	2.62	4883	−0.15	2.68
22243423−1430033	K2_206011263	UVES	4526	4365	2.05	0.01	2.35	4622	0.16	2.42
22342069−0520353	K2_206476223	UVES	4678	4686	2.99	−0.26	3.08	4899	0.08	3.14
22342769−0522505	K2_206474257	UVES	4548	4494	2.46	−0.30	2.59	4718	−0.09	2.66
22344800−0516214	K2_206480011	UVES	4735	4736	2.85	−0.18	3.04	4981	0.17	3.09
22354169−0543252	K2_206454848	UVES	4654	4588	2.54	−0.23	2.76	4878	0.13	2.82
22362945−0540124	K2_206457928	UVES	4710	4738	2.86	−0.38	2.88	4970	−0.10	2.94
22370810−1514265	K2_205985980	UVES	4507	4442	2.21	−0.51	2.42	4689	−0.22	2.49

Notes. Listed are: the *Gaia*-ESO CNAME; EPIC identifier; the spectroscopic instrument used; the IRFM $T_{\rm eff}$; the preliminary set of spectroscopic parameters (Prelim. spec.) sourced from the iDR5 recommended parameters where available (noted as *) or otherwise parameters from the Nice Node analysis or the GIRAFFE reduction pipeline radial velocity determination; the preliminary seismic $\log g$; the initial spectroscopic $T_{\rm eff}$ and [Fe/H] from iSpec; the initial seismic $\log g$. $^{(a)}$indicates the star with substituted [Fe/H] as described in Sect. 2.3.3.

Table C.1. continued.

CNAME	EPIC ID	Instrument	IRFM	Prelim. spec.			Prelim. seis.	Initial spec. (iSpec)		Initial seis.
			$T_{\rm eff}$ [K]	$T_{\rm eff}$ [K]	$\log g$ [log(cm s^{-2})]	[Fe/H]	$\log g$ [log(cm s^{-2})]	$T_{\rm eff}$ [K]	[Fe/H]	$\log g$ [log(cm s^{-2})]
22373392−1521214	K2_205982135	UVES	4747	4643	2.59	−0.33	2.74	4924	−0.03	2.80
22375413−0604257	K2_206433696	UVES	4615	4602	2.34	−0.16	2.45	4720	0.10	2.50
22390396−1500420	K2_205993475	UVES	4499	4387	2.30	−0.28	2.51	4543	0.01	2.58
22391293−1502196	K2_205992539	UVES	4805	4786	2.74	−0.30	2.88	4854	0.02	2.92
22014046−0900081	K2_206249125	GIRAFFE*	4709	4822	3.05	−0.33	2.99	4791	−0.38	3.03
22025754−0911548	K2_206236189	GIRAFFE*	4608	4742	2.63	−0.57	2.54	6176	0.40	2.64
22031541−0753433	K2_206322094	GIRAFFE*	4596	4732	2.64	−0.47	2.59	4394	−0.57	2.62
22032210−0755475	K2_206319951	GIRAFFE*	4827	4929	2.58	−0.62	2.32	4820	−0.66	2.35
22032304−0754111	K2_206321619	GIRAFFE*	4334	4424	1.74	−0.83	1.78	4106	−0.72	1.82
22034179−0815421	K2_206298620	GIRAFFE*	4733	4783	1.27	−2.08[(a)]	1.66	4309	−2.69	1.67
22063424−1530038	K2_205977363	GIRAFFE*	4692	4756	3.14	0.18	3.14	4194	0.30	3.15
22082566−1532383	K2_205975970	GIRAFFE*	4871	4939	2.52	−0.62	2.33	5159	−0.55	2.37
22114091−0727543	K2_206348972	GIRAFFE*	4679	4816	2.52	−0.75	2.42	4816	−0.69	2.46
22120711−0719225	K2_206357578	GIRAFFE*	4704	4846	2.61	−0.70	2.57	4897	−0.62	2.62
22261862−1430583	K2_206010721	GIRAFFE*	4469	4547	2.29	−0.48	2.32	4204	−0.52	2.35
22265063−1426015	K2_206013596	GIRAFFE*	4841	4889	3.04	−0.40	2.99	4730	−0.46	3.02
22274690−0825377	K2_206287865	GIRAFFE*	4347	4383	2.08	−0.42	2.04	4052	−0.49	2.08
22292445−0714431	K2_206362356	GIRAFFE*	4551	4673	2.37	−0.61	2.37	4635	−0.69	2.42
21585236−1201297	K2_206102910	GIRAFFE	4716	4833	1.54	−0.81	2.32	4808	−0.42	2.35
22003290−0808595	K2_206305916	GIRAFFE	4674	4692	2.00	−0.94	2.70	4415	−0.50	2.73
22013286−1140363	K2_206116318	GIRAFFE	4655	4715	2.00	−1.06	2.46	5141	−0.31	2.52
22070831−1050225	K2_206148291	GIRAFFE	4662	4679	2.07	−0.78	2.91	4668	−0.31	2.95
22071427−1431390	K2_206010346	GIRAFFE	4526	4604	1.69	−0.79	2.44	4549	−0.38	2.49
22105015−1119135	K2_206129788	GIRAFFE	...	4915	1.89	−1.08	2.02	4622	−0.82	2.05
22114679−1126477	K2_206124932	GIRAFFE	4534	4569	1.66	−0.84	2.45	4989	−0.19	2.52
22125740−0647498	K2_206389784	GIRAFFE	4366	4380	1.50	−0.90	2.21	4420	−0.28	2.27
22132023−0656012	K2_206381260	GIRAFFE	4708	4756	2.15	−0.71	2.89	4869	−0.26	2.93
22223274−0404320	K2_206537893	GIRAFFE	4830	4735	2.08	−0.87	2.81	4710	−0.15	2.86
22251246−1411451	K2_206021755	GIRAFFE	4892	4941	1.85	−0.86	2.38	6997	0.60	2.49
22291348−0626009	K2_206412084	GIRAFFE	4883	4946	2.23	−0.73	3.03	4980	−0.37	3.07
22351270−0519473	K2_206476915	GIRAFFE	4738	4752	2.00	−0.95	2.87	5615	−0.05	2.95
22370723−0605462	K2_206432278	GIRAFFE	4412	4472	1.53	−1.17	2.03	4470	−0.52	2.08

Table C.2. Parameters determined by IRFM, the final parameters from each node, the outlier assessment from uncertainties, and the final parameters for the 62 UVES and 28 GIRAFFE stars.

	IRFM	EPINARBO (EP)							Lumba (LM)							$\Delta T_{\rm eff}$		LM-EP				
CNAME	$T_{\rm eff}$ [K]	log g [log(cm s^{-2})]	$T_{\rm eff}$ [K]	σ [K]	[Fe/H]	σ	ξ [km s^{-1}]	χ^2 [log(cm s^{-2})]	log g [log(cm s^{-2})]	$T_{\rm eff}$ [K]	σ [K]	[Fe/H]	σ	ξ [km s^{-1}]	χ^2 [log(cm s^{-2})]	IRFM-EP [K]	IRFM-LM [K]	Δ log g [log(cm s^{-2})]	$\Delta T_{\rm eff}$ [K]	Δ[Fe/H]	$\Delta\xi$ [km s^{-1}]	$\Delta\chi^2$ [log(cm s^{-2})]
UVES																						
22172723−1633039	4482	1.95	4653	150	−0.76	0.09	1.44	…	1.95	4631	168	−0.89	0.21	1.32	…	−171	−149	0.00	−22	−0.13	−0.12	…
22075605−1535081	4669	2.85	4882	150	0.05	0.11	1.36	…	2.85	4762	116	−0.12	0.16	1.24	…	−213	−93	−0.01	−120	−0.17	−0.12	…
22072959−1530438	4884	3.05	5051	150	−0.05	0.10	1.26	…	3.04	4974	166	−0.22	0.21	1.16	…	−167	−90	0.00	−77	−0.17	−0.10	…
22373392−1521214	4736	2.80	4924	150	−0.03	0.11	1.41	…	2.80	4827	131	−0.18	0.16	1.21	…	−188	−91	0.00	−97	−0.15	−0.20	…
22370810−1514265	4458	2.49	4697	150	−0.22	0.11	1.44	…	2.48	4623	137	−0.32	0.19	1.32	…	−239	−165	0.00	−74	−0.10	−0.12	…
22065112−1504580	4798	2.01	4604	150	−1.89	0.11	1.36	…	2.02	4875	233	−1.70	0.26	1.20	…	194	−77	0.01	271	0.19	−0.16	…
22391293−1502196	4795	2.92	4914	150	−0.01	0.10	1.35	…	2.92	4856	125	−0.17	0.15	1.20	…	−119	−61	0.00	−58	−0.16	−0.15	…
22390396−1500420	4489	2.58	4761	150	−0.04	0.12	1.63	…	2.58	4605	218	−0.11	0.28	1.33	…	−272	−116	0.00	−156	−0.07	−0.30	…
22035226−1457037	4930	3.26	5077	150	−0.21	0.09	1.15	…	3.26	5044	115	−0.40	0.14	1.14	…	−147	−114	0.00	−33	−0.19	−0.01	…
22071748−1455524	4641	2.56	4795	150	−0.22	0.11	1.31	…	2.56	4745	149	−0.42	0.19	1.25	…	−154	−104	0.00	−50	−0.20	−0.06	…
22033684−1449366	4705	2.38	4955	150	−0.28	0.10	1.53	…	2.38	4848	193	−0.42	0.22	1.21	…	−250	−143	0.00	−107	−0.14	−0.32	…
22072768−1440392	…	2.60	4690	150	0.03	0.12	1.36	…	2.60	4617	140	−0.15	0.19	1.33	…	…	…	0.00	−73	−0.18	−0.03	…
22254071−1431281	4736	2.30	4914	150	−0.29	0.13	1.69	…	2.30	4858	180	−0.36	0.19	1.20	…	−178	−122	0.00	−56	−0.07	−0.49	…
22243423−1430033	4526	2.42	4638	150	0.12	0.11	1.77	…	2.42	4535	129	0.07	0.17	1.38	…	−112	−9	0.00	−103	−0.05	−0.39	…
22235672−1428420	4698	2.68	4885	150	−0.15	0.09	1.38	…	2.67	4765	103	−0.35	0.14	1.24	…	−187	−67	−0.01	−120	−0.20	−0.14	…
22235003−1422417	4681	3.14	4868	150	0.25	0.13	1.53	…	3.13	4738	174	0.21	0.24	1.26	…	−187	−57	−0.01	−130	−0.04	−0.27	…
22172260−1346134	4682	2.50	4816	150	−0.64	0.10	1.34	…	2.50	4811	172	−0.77	0.20	1.22	…	−134	−129	0.00	−5	−0.13	−0.12	…
22175268−1344270	4719	2.32	4810	150	−0.32	0.10	1.53	…	2.32	4817	181	−0.35	0.22	1.22	…	−91	−98	0.00	7	−0.03	−0.31	…
22250508−1341415	4708	2.62	4783	150	−0.07	0.10	1.37	…	2.61	4749	118	−0.23	0.15	1.25	…	−75	−41	0.00	−34	−0.16	−0.12	…
22174405−1338287	4706	2.68	4883	150	−0.26	0.10	1.32	…	2.68	4801	174	−0.46	0.21	1.23	…	−177	−95	0.00	−82	−0.20	−0.09	…
22185037−1257588	4477	2.48	4620	150	−0.06	0.12	1.38	…	2.48	4578	147	−0.19	0.19	1.35	…	−143	−101	0.00	−42	−0.13	−0.03	…
22182719−1252466	4637	2.60	4769	150	−0.05	0.11	1.35	…	2.60	4668	132	−0.28	0.18	1.29	…	−132	−31	0.00	−101	−0.23	−0.06	…
22204635−1245072	4787	3.19	4955	150	0.20	0.12	1.32	…	3.19	4873	184	0.07	0.22	1.20	…	−168	−86	0.00	−82	−0.13	−0.12	…
22195215−1234594	4628	2.36	4881	150	−0.02	0.12	1.48	…	2.35	4693	171	−0.17	0.21	1.28	…	−253	−65	−0.01	−188	−0.15	−0.20	…
22000793−1203412	5230	2.42	5309	150	−1.08	0.14	2.00	…	2.43	5493	***512***$^{(a)}$	−1.03	***0.50***$^{(b)}$	1.10	…	−79	−263	0.01	184	0.05	***−0.90***	…
21563608−1202424	4667	2.93	4842	150	−0.21	0.11	1.17	…	2.93	4857	226	−0.35	0.26	1.20	…	−175	−190	0.00	15	−0.14	0.03	…
21590887−1159078	4581	2.37	4806	150	0.01	0.12	1.51	…	2.36	4675	254$^{(a)}$	−0.14	0.33$^{(b)}$	1.29	…	−225	−94	0.00	−131	−0.15	−0.22	…
22015504−1153022	4629	2.49	4848	150	−0.21	0.11	1.44	…	2.49	4755	130	−0.35	0.18	1.25	…	−219	−126	0.00	−93	−0.14	−0.19	…
22013369−1141245	4506	2.24	4731	150	−0.37	0.10	1.43	…	2.24	4644	158	−0.56	0.20	1.31	…	−225	−138	0.00	−87	−0.19	−0.12	…
22021848−1139147	4503	2.39	4793	150	0.11	0.11	1.65	…	2.38	4606	125	0.03	0.15	1.33	…	−290	−103	−0.01	−187	−0.08	−0.32	…
22104061−1125284	4488	2.47	4754	150	0.02	0.12	1.51	…	2.46	4568	148	−0.18	0.18	1.36	…	−266	−80	−0.01	−186	−0.20	−0.15	…
22074730−1059405	4667	2.79	4900	150	0.03	0.11	1.41	…	2.78	4743	128	−0.17	0.17	1.25	…	−233	−76	−0.01	−157	−0.20	−0.16	…
22074607−1055493	4720	2.27	4731	150	−1.12	0.12	1.44	…	2.27	4850	271$^{(a)}$	−1.10	0.32$^{(b)}$	1.21	…	−11	−130	0.01	119	0.02	−0.23	…
22094505−1051031	4148	1.61	4384	150	−0.45	0.12	1.58	…	1.61	4288	155	−0.67	0.27	1.57	…	−236	−140	0.00	−96	−0.22	−0.01	…
22114557−0957433	4858	3.16	5003	150	−0.10	0.09	1.27	…	3.15	4925	146	−0.26	0.17	1.18	…	−145	−67	0.00	−78	−0.16	−0.09	…
22105372−0956597	4623	2.57	4819	150	−0.31	0.10	1.26	…	2.56	4744	151	−0.52	0.20	1.26	…	−196	−121	0.00	−75	−0.21	0.00	…
22083624−0948555	4759	2.75	4996	150	0.40	0.12	1.64	…	2.74	4735	154	0.25	0.16	1.26	…	−237	24	−0.01	−261	−0.15	−0.38	…
22091180−0944335	4844	3.35	4957	150	−0.15	0.10	1.06	…	3.35	4969	146	−0.31	0.19	1.16	…	−113	−125	0.00	12	−0.16	0.10	…
22102197−0923157	4841	2.51	4983	150	−0.15	0.08	1.46	…	2.51	4925	152	−0.25	0.18	1.17	…	−142	−84	0.00	−58	−0.10	−0.29	…
22013945−0909229	4541	3.04	4721	150	0.23	0.12	1.54	…	3.04	4669	140	0.21	0.19	1.29	…	−180	−128	0.00	−52	−0.02	−0.25	…
22052550−0854435	4756	2.36	4942	150	−0.25	0.09	1.63	…	2.35	4817	168	−0.33	0.19	1.22	…	−186	−61	0.00	−125	−0.08	−0.41	…
22052114−0848002	4697	2.46	4820	150	−0.32	0.09	1.38	…	2.46	4818	153	−0.40	0.17	1.22	…	−123	−121	0.00	−2	−0.08	−0.16	…
22050764−0840472	4892	3.11	5006	150	−0.25	0.10	1.19	…	3.11	5014	182	−0.42	0.23	1.15	…	−114	−122	0.00	8	−0.17	−0.04	…
22055148−0840028	4593	2.68	4800	150	−0.21	0.11	1.33	…	2.68	4740	165	−0.36	0.22	1.26	…	−207	−147	0.00	−60	−0.15	−0.07	…

Notes. Values in bold indicate extreme disagreements. * = EP flags this analysis as lacking sufficient Fe I and Fe II lines. $^{(a)}$ = LM $T_{\rm eff}$ error is greater than (median error + 3*σ error) = (244 K). $^{(b)}$ = LM [Fe/H] error is greater than (median error + 3*σ error) = (0.28). $^{(c)}$ = LM $T_{\rm eff}$ error is greater than (median error + 3*σ error) = (294 K).

Table C.2. continued.

CNAME	IRFM	EPINARBO (EP)							Lumba (LM)							$\Delta T_{\rm eff}$		LM-EP				
	$T_{\rm eff}$ [K]	$\log g$ [log(cm s^{-2})]	$T_{\rm eff}$ [K]	σ [K]	[Fe/H]	σ	ξ [km s^{-1}]	χ^2 [log(cm s^{-2})]	$\log g$ [log(cm s^{-2})]	$T_{\rm eff}$ [K]	σ [K]	[Fe/H]	σ	ξ [km s^{-1}]	χ^2 [log(cm s^{-2})]	IRFM-EP [K]	IRFM-LM [K]	$\Delta \log g$ [log(cm s^{-2})]	$\Delta T_{\rm eff}$ [K]	Δ[Fe/H]	$\Delta\xi$ [km s^{-1}]	$\Delta\chi^2$ [log(cm s^{-2})]
22032202−0829154*	5125	2.49	5421	150	0.29	0.10	1.49	…	2.47	4742	159	−0.08	0.18	1.25	…	−296	383	−0.03	***−679***	−0.37	−0.24	…
22062074−0809079	4602	2.65	4771	150	−0.01	0.11	1.41	…	2.65	4674	129	−0.22	0.16	1.29	…	−169	−72	0.00	−97	−0.21	−0.12	…
22291753−0806290	4577	2.65	4772	150	−0.25	0.10	1.36	…	2.65	4734	106	−0.39	0.15	1.26	…	−195	−157	0.00	−38	−0.14	−0.10	…
22271794−0747334	4776	2.83	4890	150	−0.21	0.10	1.22	…	2.83	4860	173	−0.41	0.20	1.20	…	−114	−84	0.00	−30	−0.20	−0.02	…
22122727−0719010	4358	2.20	4531	150	−0.18	0.13	1.53	…	2.20	4439	143	−0.31	0.24	1.42	…	−173	−81	0.00	−92	−0.13	−0.11	…
22292970−0713347	4716	2.41	4928	150	−0.18	0.09	1.61	…	2.41	4823	145	−0.27	0.17	1.22	…	−212	−107	0.00	−105	−0.09	−0.39	…
22130580−0658576	4449	2.37	4667	150	−0.06	0.12	1.54	…	2.36	4526	142	−0.25	0.21	1.39	…	−218	−77	−0.01	−141	−0.19	−0.15	…
22154837−0628154	4738	2.43	4904	150	−0.56	0.09	1.37	…	2.42	4834	192	−0.72	0.22	1.21	…	−166	−96	0.00	−70	−0.16	−0.16	…
22152258−0623152	4869	3.20	5083	150	−0.04	0.10	1.30	…	3.20	4955	168	−0.25	0.20	1.17	…	−214	−86	0.00	−128	−0.21	−0.13	…
22092886−0617515	4617	2.88	4930	150	−0.15	0.10	1.33	…	2.88	4807	167	−0.29	0.21	1.23	…	−313	−190	−0.01	−123	−0.14	−0.10	…
22153043−0617291	4866	2.40	4962	140	−0.46	0.09	1.52	…	2.40	4946	172	−0.51	0.20	1.17	…	−96	−80	0.00	−16	−0.05	−0.35	…
22092416−0610474	…	2.50	4886	150	0.03	0.10	1.54	…	2.49	4765	114	−0.10	0.14	1.24	…	…	…	0.00	−121	−0.13	−0.30	…
22085850−0608204	4690	2.37	4891	150	−0.27	0.11	1.48	…	2.37	4870	205	−0.33	0.24	1.20	…	−201	−180	0.00	−21	−0.06	−0.28	…
22375413−0604257	4609	2.50	4860	150	0.12	0.10	1.53	…	2.50	4710	112	−0.04	0.15	1.27	…	−251	−101	0.00	−150	−0.16	−0.26	…
22354169−0543252	4646	2.82	4878	150	0.13	0.11	1.33	…	2.82	4728	112	−0.12	0.16	1.26	…	−232	−82	−0.01	−150	−0.25	−0.07	…
22362945−0540124	4698	2.94	4972	150	−0.09	0.10	1.37	…	2.93	4836	150	−0.29	0.18	1.21	…	−274	−138	−0.01	−136	−0.20	−0.16	…
22342769−0522505	4539	2.66	4750	150	−0.08	0.11	1.37	…	2.65	4668	129	−0.22	0.17	1.29	…	−211	−129	0.00	−82	−0.14	−0.08	…
22342069−0520353	4669	3.14	4899	150	0.08	0.11	1.21	…	3.14	4821	164	−0.10	0.20	1.22	…	−230	−152	0.00	−78	−0.18	0.01	…
22344800−0516214	4728	3.09	4985	150	0.17	0.10	1.38	…	3.08	4851	148	−0.02	0.17	1.20	…	−257	−123	−0.01	−134	−0.19	−0.18	…
GIRAFFE																						
22082566−1532383	4871	2.37	5159	150	−0.55	0.16	2.52	2.24	2.36	4799	229	−0.72	0.22	1.23	2.08	***−288***	72	−0.02	***−360***	−0.17	***−1.29***	0.16
22063424−1530038	4692	3.15	4194	125	0.28	0.18	1.40	15.89*	3.18	4698	146	−0.02	0.21	1.28	8.46	***498***	−6	0.02	***504***	−0.30	−0.12	***7.42***
22071427−1431390	4526	2.49	4549	150	−0.38	0.19	1.81	2.17	2.49	4524	158	−0.62	0.21	1.37	2.42	−23	2	0.00	−25	−0.24	−0.44	−0.26
22261862−1430583	4469	2.35	4204	117	−0.52	0.19	2.07	2.47	2.37	4509	247	−0.58	0.26	1.39	2.06	265	−40	0.02	305	−0.06	−0.68	0.42
22265063−1426015	4841	3.02	4640	139	−0.51	0.17	1.96	3.55	3.02	4823	152	−0.54	0.16	1.22	3.29	201	18	0.00	183	−0.03	−0.74	0.26
22251246−1411451	4892	2.49	6997	150	0.60	0.19	2.31	34.25*	2.41	4797	210	−0.69	0.18	1.24	2.66	***−2105***	95	−0.08	***−2200***	−1.29	***−1.07***	***31.60***
21585236−1201297	4716	2.35	4808	150	−0.42	0.17	1.82	0.97	2.35	4754	322$^{(c)}$	−0.55	0.30$^{(b)}$	1.24	0.95	−92	−38	0.00	−54	−0.13	−0.58	0.01
22013286−1140363	4655	2.52	5141	117	−0.31	0.16	1.40	1.90*	2.50	4696	198	−0.77	0.24	1.28	1.43	***−486***	−41	−0.02	***−445***	***−0.46***	−0.12	0.47
22114679−1126477	4534	2.52	4989	139	−0.19	0.18	1.70	1.23	2.50	4492	232	−0.74	0.30$^{(b)}$	1.39	1.03	***−455***	42	−0.02	***−497***	***−0.55***	−0.31	0.20
22105015−1119135	…	2.05	4622	127	−0.82	0.18	1.49	1.55	2.04	4581	207	−1.11	0.27	1.35	1.01	…	…	0.00	−41	−0.29	−0.14	0.54
22070831−1050225	4662	2.95	4668	126	−0.34	0.17	1.63	1.87	2.96	4753	185	−0.47	0.23	1.25	1.95	−6	−91	0.00	85	−0.13	−0.38	−0.07
22025754−0911548	4608	2.64	6176	150	0.40	0.16	1.72	8.80*	2.58	4658	195	−0.70	0.23	1.30	1.63	***−1568***	−50	−0.06	***−1518***	−1.10	−0.42	***7.17***
22014046−0900081	4709	3.03	4791	150	−0.38	0.21	1.94	3.93	3.03	4767	174	−0.47	0.2	1.24	4.16	−82	−58	0.00	−24	−0.09	−0.70	−0.23
22274690−0825377	4347	2.08	3902	125	−0.48	0.21	2.80	12.72*	2.10	4341	171	−0.57	0.22	1.52	7.29	***445***	6	0.01	***439***	−0.09	***−1.28***	***5.43***
22034179−0815421	4733	1.67	4309	149	−2.69	0.16	1.41	1.25*	1.69	4754	329$^{(c)}$	−2.10	0.38$^{(b)}$	1.26	1.29	***424***	−21	0.02	***445***	***0.59***	−0.15	−0.03
22003290−0808595	4674	2.73	4325	149	−0.49	0.18	1.48	4.57*	2.75	4747	192	−0.65	0.21	1.25	2.02	***349***	−73	0.02	***422***	−0.16	−0.23	***2.56***
22032210−0755475	4827	2.35	4820	150	−0.69	0.19	1.90	1.24	2.35	4775	261	−0.75	0.23	1.25	1.24	7	52	0.00	−45	−0.06	−0.65	0.00
22032304−0754111	4334	1.82	4106	150	−0.72	0.16	1.69	3.97	1.83	4368	209	−0.93	0.22	1.50	2.17	228	−34	0.01	262	−0.21	−0.19	***1.81***
22031541−0753433	4596	2.62	4394	95	−0.57	0.20	1.92	2.94	2.63	4669	194	−0.59	0.23	1.29	2.41	202	−73	0.01	275	−0.02	−0.63	0.52
22114091−0727543	4679	2.46	4816	150	−0.69	0.18	1.65	1.54	2.45	4704	190	−0.86	0.22	1.28	1.44	−137	−25	−0.01	−112	−0.17	−0.37	0.10
22120711−0719225	4704	2.62	4897	150	−0.62	0.18	1.73	1.51	2.61	4760	204	−0.78	0.21	1.25	1.45	−193	−56	−0.01	−137	−0.16	−0.48	0.06
22292445−0714431	4551	2.42	4635	150	−0.69	0.21	1.94	4.16	2.42	4622	194	−0.70	0.19	1.33	4.17	−84	−71	0.00	−13	−0.01	−0.61	0.00
22132023−0656012	4708	2.93	4869	150	−0.26	0.18	1.91	1.73	2.93	4727	130	−0.54	0.19	1.25	1.81	−161	−19	−0.01	−142	−0.28	−0.66	−0.08
22125740−0647498	4366	2.27	4420	150	−0.28	0.19	1.40	2.51	2.27	4364	130	−0.69	0.21	1.49	2.83	−54	2	0.00	−56	***−0.41***	0.09	−0.32
22154067−0627110	4876	3.13	4621	100	−0.48	0.15	1.49	3.37	3.14	4885	180	−0.58	0.21	1.19	2.31	***255***	−9	0.01	***264***	−0.10	−0.30	***1.07***
22291348−0626009	4883	3.07	4980	150	−0.37	0.20	1.97	2.14	3.07	4948	173	−0.47	0.19	1.17	2.18	−97	−65	0.00	−32	−0.10	−0.80	−0.04
22370723−0605462	4412	2.08	4470	150	−0.52	0.21	1.48	0.95	2.08	4512	371$^{(c)}$	−0.79	0.35$^{(b)}$	1.40	0.85	−58	−100	0.00	42	−0.27	−0.08	0.11
22351270−0519473	4738	2.95	5615	137	−0.05	0.16	1.92	2.79*	2.91	4812	213	−0.65	0.22	1.22	1.45	***−877***	−74	−0.03	***−803***	−0.60	−0.70	1.34
22223274−0404320	4830	2.86	4710	150	−0.15	0.18	1.33	0.85	2.86	4783	245	−0.62	0.32$^{(b)}$	1.22	0.66	120	47	0.00	73	***−0.47***	−0.11	0.19

Table C.3. Final stellar parameters for the 90 K2@*Gaia*-ESO stars.

CNAME	EPIC ID	Instrument	Node SP	$T_{\rm eff}$ [K]	σ [K]	$\log g$ [log(cm s^{-2})]	σ [log(cm s^{-2})]	[Fe/H]	σ	ξ [km s^{-1}]	σ [km s^{-1}]
21563608−1202424	K2_206102116	UVES	Both	4850	11	3.01	0.02	−0.28	0.10	1.18	0.02
21590887−1159078	K2_206104478	UVES	Both	4741	93	2.45	0.02	−0.07	0.11	1.40	0.11
22000793−1203412	K2_206101493	UVES	EP	5309	150	2.46	0.02	−1.08	0.14	2.00	0.15
22013369−1141245	K2_206115828	UVES	Both	4688	62	2.33	0.03	−0.47	0.13	1.37	0.06
22013945−0909229	K2_206238956	UVES	Both	4695	37	3.13	0.02	0.22	0.01	1.41	0.12
22015504−1153022	K2_206108556	UVES	Both	4802	66	2.57	0.02	−0.28	0.10	1.35	0.10
22021848−1139147	K2_206117168	UVES	Both	4700	132	2.48	0.02	0.07	0.06	1.49	0.16
22032202−0829154	K2_206283732	UVES	LM	4742	159	2.55	0.02	−0.08	0.18	1.25	0.07
22033684−1449366	K2_205999925	UVES	Both	4902	76	2.46	0.02	−0.35	0.10	1.37	0.16
22035226−1457037	K2_205995590	UVES	Both	5061	23	3.32	0.01	−0.31	0.13	1.14	0.07
22050764−0840472	K2_206270701	UVES	Both	5010	6	3.17	0.02	−0.34	0.12	1.17	0.02
22052114−0848002	K2_206262569	UVES	Both	4819	1	2.54	0.02	−0.36	0.06	1.30	0.08
22052550−0854435	K2_206255139	UVES	Both	4880	88	2.43	0.02	−0.29	0.06	1.42	0.20
22055148−0840028	K2_206271510	UVES	Both	4770	42	2.77	0.02	−0.29	0.11	1.30	0.04
22062074−0809079	K2_206305769	UVES	Both	4723	69	2.74	0.02	−0.12	0.15	1.35	0.06
22065112−1504580	K2_205991117	UVES	Both	4740	192	2.11	0.03	−1.80	0.13	1.28	0.08
22071748−1455524	K2_205996255	UVES	Both	4770	35	2.64	0.02	−0.32	0.14	1.28	0.03
22072768−1440392	K2_206005223	UVES	Both	4654	52	2.70	0.02	−0.06	0.13	1.35	0.02
22072959−1530438	K2_205977024	UVES	Both	5013	54	3.11	0.02	−0.14	0.12	1.21	0.05
22074607−1055493	K2_206144769	UVES	Both	4791	84	2.36	0.02	−1.11	0.01	1.33	0.12
22074730−1059405	K2_206142277	UVES	Both	4822	111	2.87	0.02	−0.07	0.14	1.33	0.08
22075605−1535081	K2_205974551	UVES	Both	4822	85	2.93	0.02	−0.04	0.12	1.30	0.06
22083624−0948555	K2_206196672	UVES	Both	4866	185	2.82	0.02	0.33	0.11	1.45	0.19
22085850−0608204	K2_206429616	UVES	Both	4881	15	2.44	0.02	−0.30	0.04	1.34	0.14
22091180−0944335	K2_206201030	UVES	Both	4963	8	3.41	0.03	−0.23	0.11	1.11	0.05
22092416−0610474	K2_206427237	UVES	Both	4826	86	2.58	0.02	−0.04	0.09	1.39	0.15
22092886−0617515	K2_206420120	UVES	Both	4869	87	2.96	0.02	−0.22	0.10	1.28	0.05
22094505−1051031	K2_206147901	UVES	Both	4336	68	1.74	0.03	−0.56	0.16	1.58	0.07
22102197−0923157	K2_206223471	UVES	Both	4954	41	2.58	0.02	−0.20	0.07	1.32	0.15
22104061−1125284	K2_206125783	UVES	Both	4661	132	2.56	0.02	−0.08	0.14	1.43	0.07
22105372−0956597	K2_206188891	UVES	Both	4782	53	2.65	0.02	−0.42	0.15	1.26	0.07
22114557−0957433	K2_206188223	UVES	Both	4964	55	3.22	0.02	−0.18	0.11	1.22	0.04
22122727−0719010	K2_206357934	UVES	Both	4485	65	2.32	0.02	−0.25	0.09	1.47	0.05
22130580−0658576	K2_206378264	UVES	Both	4597	100	2.46	0.02	−0.16	0.13	1.46	0.07
22153043−0617291	K2_206420485	UVES	Both	4954	11	2.47	0.03	−0.49	0.04	1.34	0.17
22154837−0628154	K2_206409829	UVES	Both	4869	49	2.50	0.02	−0.64	0.11	1.29	0.08
22172260−1346134	K2_206037023	UVES	Both	4814	4	2.58	0.02	−0.71	0.09	1.28	0.06
22172723−1633039	K2_205944548	UVES	Both	4642	16	2.05	0.02	−0.83	0.09	1.38	0.06
22174405−1338287	K2_206041863	UVES	Both	4842	58	2.76	0.02	−0.36	0.14	1.28	0.05
22175268−1344270	K2_206038132	UVES	Both	4814	5	2.40	0.02	−0.34	0.02	1.37	0.15
22182719−1252466	K2_206070270	UVES	Both	4719	71	2.69	0.02	−0.17	0.16	1.32	0.03
22185037−1257588	K2_206066993	UVES	Both	4599	30	2.58	0.02	−0.13	0.09	1.36	0.01
22195215−1234594	K2_206081428	UVES	Both	4787	133	2.44	0.02	−0.10	0.11	1.38	0.10
22204635−1245072	K2_206075005	UVES	Both	4914	58	3.26	0.02	0.14	0.09	1.26	0.06
22235003−1422417	K2_206015475	UVES	Both	4803	92	3.22	0.02	0.23	0.03	1.39	0.13
22235672−1428420	K2_206012087	UVES	Both	4825	85	2.75	0.02	−0.25	0.14	1.31	0.07
22243423−1430033	K2_206011263	UVES	Both	4587	73	2.51	0.04	0.10	0.04	1.57	0.19
22250508−1341415	K2_206039882	UVES	Both	4766	24	2.70	0.02	−0.15	0.11	1.31	0.06
22254071−1431281	K2_206010465	UVES	Both	4886	40	2.38	0.02	−0.33	0.05	1.45	0.25
22271794−0747334	K2_206328599	UVES	Both	4875	21	2.91	0.02	−0.31	0.14	1.21	0.01
22291753−0806290	K2_206308617	UVES	Both	4753	27	2.73	0.02	−0.32	0.10	1.31	0.05
22292970−0713347	K2_206363486	UVES	Both	4876	74	2.48	0.03	−0.23	0.06	1.42	0.20
22342069−0520353	K2_206476223	UVES	Both	4860	55	3.21	0.01	−0.01	0.13	1.22	0.07
22342769−0522505	K2_206474257	UVES	Both	4709	58	2.75	0.02	−0.15	0.10	1.33	0.04
22344800−0516214	K2_206480011	UVES	Both	4918	95	3.16	0.01	0.08	0.13	1.29	0.09
22354169−0543252	K2_206454848	UVES	Both	4803	106	2.90	0.02	0.01	0.18	1.3	0.04
22362945−0540124	K2_206457928	UVES	Both	4904	96	3.01	0.02	−0.19	0.14	1.29	0.08

Table C.3. continued.

CNAME	EPIC ID	Instrument	Node SP	$T_{\rm eff}$ [K]	σ [K]	$\log g$ [log(cm s^{-2})]	σ [log(cm s^{-2})]	[Fe/H]	σ	ξ [km s^{-1}]	σ [km s^{-1}]
22370810−1514265	K2_205985980	UVES	Both	4660	52	2.58	0.02	−0.27	0.07	1.38	0.06
22373392−1521214	K2_205982135	UVES	Both	4876	69	2.87	0.02	−0.11	0.11	1.31	0.10
22375413−0604257	K2_206433696	UVES	Both	4785	106	2.59	0.02	0.04	0.11	1.40	0.13
22390396−1500420	K2_205993475	UVES	Both	4683	110	2.67	0.02	−0.08	0.05	1.48	0.15
22391293−1502196	K2_205992539	UVES	Both	4885	41	3.00	0.02	−0.09	0.11	1.28	0.08
21585236−1201297	K2_206102910	GIRAFFE	Both	4781	38	2.44	0.02	−0.49	0.09	1.53	0.29
22003290−0808595	K2_206305916	GIRAFFE	LM	4747	192	2.84	0.02	−0.65	0.21	1.25	0.29
22013286−1140363	K2_206116318	GIRAFFE	LM	4696	198	2.59	0.02	−0.77	0.24	1.28	0.29
22014046−0900081	K2_206249125	GIRAFFE	Both	4779	17	3.11	0.02	−0.43	0.06	1.59	0.35
22025754−0911548	K2_206236189	GIRAFFE	LM	4658	195	2.67	0.02	−0.70	0.23	1.30	0.29
22031541−0753433	K2_206322094	GIRAFFE	Both	4532	194	2.73	0.02	−0.58	0.01	1.61	0.31
22032210−0755475	K2_206319951	GIRAFFE	Both	4798	32	2.43	0.02	−0.72	0.04	1.57	0.33
22032304−0754111	K2_206321619	GIRAFFE	LM	4368	209	1.96	0.03	−0.93	0.22	1.50	0.29
22034179−0815421	K2_206298620	GIRAFFE	LM	4754	329	1.78	0.03	−2.10	0.38	1.26	0.29
22063424−1530038	K2_205977363	GIRAFFE	LM	4698	146	3.27	0.02	−0.02	0.21	1.28	0.29
22070831−1050225	K2_206148291	GIRAFFE	Both	4711	60	3.04	0.02	−0.41	0.09	1.44	0.19
22071427−1431390	K2_206010346	GIRAFFE	Both	4537	18	2.59	0.01	−0.50	0.17	1.59	0.22
22082566−1532383	K2_205975970	GIRAFFE	LM	4799	229	2.41	0.02	−0.72	0.22	1.23	0.29
22105015−1119135	K2_206129788	GIRAFFE	Both	4602	29	2.15	0.03	−0.97	0.21	1.42	0.07
22114091−0727543	K2_206348972	GIRAFFE	Both	4760	79	2.54	0.02	−0.78	0.12	1.47	0.18
22114679−1126477	K2_206124932	GIRAFFE	LM	4492	232	2.61	0.03	−0.74	0.30	1.39	0.29
22120711−0719225	K2_206357578	GIRAFFE	Both	4829	97	2.69	0.02	−0.70	0.11	1.49	0.24
22125740−0647498	K2_206389784	GIRAFFE	Both	4392	40	2.39	0.02	−0.49	0.29	1.44	0.04
22132023−0656012	K2_206381260	GIRAFFE	Both	4798	100	3.01	0.02	−0.40	0.20	1.58	0.33
22223274−0404320	K2_206537893	GIRAFFE	Both	4747	52	2.95	0.02	−0.39	0.33	1.28	0.05
22251246−1411451	K2_206021755	GIRAFFE	LM	4797	210	2.49	0.02	−0.69	0.18	1.24	0.29
22261862−1430583	K2_206010721	GIRAFFE	Both	4357	216	2.48	0.02	−0.55	0.04	1.73	0.34
22265063−1426015	K2_206013596	GIRAFFE	Both	4732	129	3.11	0.02	−0.53	0.02	1.59	0.37
22274690−0825377	K2_206287865	GIRAFFE	LM	4341	171	2.22	0.02	−0.57	0.22	1.52	0.29
22291348−0626009	K2_206412084	GIRAFFE	Both	4964	23	3.14	0.02	−0.42	0.07	1.57	0.4
22292445−0714431	K2_206362356	GIRAFFE	Both	4629	9	2.52	0.02	−0.70	0.01	1.63	0.31
22351270−0519473	K2_206476915	GIRAFFE	LM	4812	213	2.99	0.02	−0.65	0.22	1.22	0.29
22370723−0605462	K2_206432278	GIRAFFE	Both	4491	30	2.19	0.02	−0.66	0.19	1.44	0.04

Table C.4. Radial (RV) and rotational velocities ($v \sin i$) of the K2@*Gaia*-ESO stars measured by *Gaia*-ESO and from the *Gaia* Data Release 2 (GDR2).

CNAME	GDR2_ID	*Gaia*-ESO			GDR2			BIN_FLAG
		RV [km s^{-1}]	σ_{RV} [km s^{-1}]	$v \sin i$ [km s^{-1}]	RV [km s^{-1}]	σ_{RV} [km s^{-1}]	NT	
21563608−1202424	2613587930052748544	21.66	0.13	3.48	…	…	0	…
21585236−1201297	2613577385908074240	−67.49	0.17	3.00	…	…	0	…
21590887−1159078	2613600956688590592	16.67	0.13	3.46	16.38	0.54	7	0
22000793−1203412	2613550340498556544	−0.03	0.13	2.18	1.90	1.42	6	1
22003290−0808595	2618490072580174720	−2.53	0.15	3.35	−4.84	2.95	5	1
22013286−1140363	2613657547177899648	−139.72	0.15	2.80	…	…	0	…
22013369−1141245	2613657439802765952	19.69	0.13	2.00	20.04	0.22	3	0
22013945−0909229	2617607955016992512	−33.49	0.13	4.32	−33.32	0.34	6	0
22014046−0900081	2617658562616240512	21.54	0.14	2.95	…	…	0	…
22015504−1153022	2613637996486748544	14.76	0.13	2.14	…	…	0	…
22021848−1139147	2613652668095035904	−44.21	0.13	4.59	−44.95	0.23	6	0
22025754−0911548	2617616162699618304	−59.21	0.15	2.00	…	…	0	…
22031541−0753433	2620011178197806464	35.23	0.15	7.85	36.10	2.50	3	1
22032202−0829154	2619201868920270720	21.16	0.13	4.12	21.06	0.18	7	0
22032210−0755475	2620007948382396544	−23.11	0.15	5.20	…	…	0	…
22032304−0754111	2620011006399112064	−142.62	0.15	2.95	−143.61	0.17	2	0
22033684−1449366	6839442021074270848	−10.83	0.13	2.48	−11.50	0.60	6	0
22034179−0815421	2619223854857324544	11.36	0.16	5.95	…	…	0	…
22035226−1457037	6839343447280471680	16.54	0.13	2.00	16.50	0.76	6	0
22050764−0840472	2619138784440607744	−62.66	0.13	2.06	−63.55	3.13	5	1
22052114−0848002	2619133767918800896	−41.18	0.13	2.00	−41.30	0.73	7	0
22052550−0854435	2618938638964627840	−32.39	0.13	2.11	−32.43	0.24	4	0
22055148−0840028	2619136688496602880	27.89	0.13	3.67	28.09	0.97	4	0
22062074−0809079	2619193622583116800	11.16	0.13	2.05	10.81	0.87	4	0
22063424−1530038	6827335058023087744	−18.22	0.14	6.25	−18.13	0.80	6	0
22065112−1504580	6827402093872328448	−227.09	0.13	2.00	−225.21	1.29	9	1
22070831−1050225	2614104704812671104	−18.87	0.15	2.75	…	…	0	…
22071427−1431390	6839466038531200768	−40.31	0.15	1.90	−38.45	1.20	4	1
22071748−1455524	6827427215136331264	43.76	0.13	2.05	…	…	0	…
22072768−1440392	6827450201801303552	−7.97	0.13	2.72	−7.32	0.57	3	0
22072959−1530438	6827323306992566016	19.57	0.13	2.01	…	…	0	…
22074607−1055493	2613912698299751552	43.99	0.13	2.00	42.74	1.54	4	0
22074730−1059405	2613911083392048384	−28.24	0.13	2.31	−29.01	0.58	5	0
22075605−1535081	6827318741442243712	46.88	0.13	3.88	46.43	1.05	3	0
22082566−1532383	6827137523887097728	−13.64	0.15	7.85	…	…	0	…
22083624−0948555	2615818774720916992	−34.20	0.13	2.84	−34.42	0.87	4	0
22085850−0608204	2620746717116934144	−31.98	0.13	5.34	−32.15	0.24	6	0
22091180−0944335	2615820797649945600	49.38	0.13	3.71	48.47	0.37	4	0
22092416−0610474	2620698544763739136	6.60	0.13	2.41	6.38	0.37	5	0
22092886−0617515	2620695349308068096	−34.32	0.13	3.66	−34.91	1.36	4	0
22094505−1051031	2613998357127036032	−19.86	0.13	4.45	−20.04	0.74	6	0
22102197−0923157	2615859559730415744	−8.29	0.13	2.02	−7.62	0.17	4	0
22104061−1125284	2613165824961766400	−13.93	0.13	2.35	−12.47	0.66	3	0
22105015−1119135	2613169089136874240	−101.57	0.58	3.40	…	…	0	…
22105372−0956597	2615757300853446912	62.53	0.13	2.00	62.43	0.89	6	0
22114091−0727543	2619722865633187328	14.22	0.15	2.90	…	…	0	…
22114557−0957433	2615570525611215488	42.26	0.13	3.57	41.60	0.40	9	0
22114679−1126477	2613151806188434688	−114.88	0.23	2.45	…	…	0	…
22120711−0719225	2619725889290212096	−12.74	0.15	3.00	−17.19	3.70	3	1
22122727−0719010	2619731627366513024	−37.14	0.13	4.20	−36.03	0.95	2	0
22125740−0647498	2619856250137446272	−47.38	0.16	2.85	…	…	0	…
22130580−0658576	2619835359416507904	−28.92	0.13	2.51	−30.42	0.85	5	0
22132023−0656012	2619835939236632448	17.83	0.19	2.80	…	…	0	…
22153043−0617291	2625901085893901312	−1.70	0.13	2.02	−2.74	0.67	4	0
22154837−0628154	2625882050598847360	28.95	0.13	2.00	40.22	5.83	4	1
22172260−1346134	2600364275503466880	−69.60	0.13	2.00	−67.16	0.62	4	1
22172723−1633039	2598648384529477376	−140.15	0.13	2.00	−139.22	0.50	7	0
22174405−1338287	2600366955563057792	57.20	0.13	2.00	…	…	0	…
22175268−1344270	2600365340655364096	51.01	0.13	2.64	52.70	0.31	6	0
22182719−1252466	2600709938766944640	−25.36	0.13	2.45	0.35	8.44	2	1
22185037−1257588	2600696538468974080	23.24	0.13	4.09	23.86	0.64	3	0

Notes. NT refers to the number of transits *Gaia* considered for the RV measurement. A BIN_FLAG of 1 indicates a possible binary based on the GDR2 and *Gaia*-ESO measurements (see Sect. 6).

Table C.4. continued.

CNAME	GDR2_ID	*Gaia*-ESO			GDR2			BIN_FLAG
		RV [km s^{-1}]	σ_{RV} [km s^{-1}]	$v \sin i$ [km s^{-1}]	RV [km s^{-1}]	σ_{RV} [km s^{-1}]	NT	
22195215−1234594	2600745118843546752	−2.15	0.13	4.33	−2.34	0.48	4	0
22204635−1245072	2600732302661139328	−15.20	0.13	3.85	…	…	0	…
22223274−0404320	2626685179418707328	39.55	0.60	3.05	…	…	0	…
22235003−1422417	2599473018250149888	−24.12	0.13	4.23	−23.29	1.10	4	0
22235672−1428420	2599468860721809408	19.45	0.13	2.03	…	…	0	…
22243423−1430033	2599374165283135872	−33.90	0.13	2.92	…	…	0	…
22250508−1341415	2599676496620789632	−31.46	0.13	2.20	…	…	0	…
22251246−1411451	2599574310758896768	−57.96	0.15	4.85	…	…	0	…
22254071−1431281	2599359562394330112	41.16	0.13	12.42	…	…	0	…
22261862−1430583	2599361830137062144	22.73	0.15	1.95	…	…	0	…
22265063−1426015	2599364097879793280	−21.74	0.14	3.00	…	…	0	…
22271794−0747334	2621610928961244544	31.49	0.13	2.00	25.20	1.39	7	1
22274690−0825377	2621431227529840896	−61.04	0.14	1.70	−49.43	0.55	4	1
22291348−0626009	2622883480526606208	29.83	0.15	3.10	…	…	0	…
22291753−0806290	2621536849365338752	9.56	0.13	2.32	…	…	0	…
22292445−0714431	2622406528702960768	−27.84	0.14	3.60	…	…	0	…
22292970−0713347	2622406666141913728	19.65	0.13	2.15	20.34	0.38	5	0
22342069−0520353	2624569611672100352	−24.03	0.13	3.94	−23.35	0.81	4	0
22342769−0522505	2624557555699371392	27.06	0.13	3.98	27.37	0.69	2	0
22344800−0516214	2624560441917415296	−6.82	0.13	2.38	−6.42	0.26	4	0
22351270−0519473	2624556078230641408	−71.19	0.15	3.00	…	…	0	…
22354169−0543252	2624481066626339968	20.38	0.13	2.36	20.75	0.26	3	0
22362945−0540124	2624485194090351360	−16.90	0.13	2.14	−17.12	0.45	6	0
22370723−0605462	2623705365468400000	−144.60	0.17	3.00	…	…	0	…
22370810−1514265	2597489945950043904	−51.26	0.13	4.10	−64.23	6.25	6	1
22373392−1521214	2596737502040057088	19.38	0.13	2.36	18.99	3.26	3	1
22375413−0604257	2623708045527985664	−18.47	0.13	2.63	−19.40	1.22	2	0
22390396−1500420	2596843295674302208	−33.40	0.13	4.05	−33.43	0.40	7	0
22391293−1502196	…	−40.85	0.13	2.11	−40.70	0.16	2	0

Appendix D: *Gaia* surface gravity

Bolometric corrections were interpolated from the tables of Houdashelt et al. (2000). These corrections are tabulated for the K magnitude in the CIT/CTIO system (Elias et al. 1982). Thus, first the Ks magnitude of 2MASS were converted to $K_{CIT/CTIO}$ using the relations provided by Carpenter (2001).

The bolometric corrections (BC) are mostly independent of $\log g$. First the two tables of metallicity values closest to the metallicity of the star (usually [Fe/H] = 0.00 and [Fe/H] = −0.50) are found. These tables are used to linearly interpolate the corrections to the $T_{\rm eff}$ of the star. Then a second linear interpolation is carried out to the metallicity of the star.

The $E(B-V)$ is converted to A_{Ks} using the coefficients of McCall (2004). In this case, $A_{Ks}/E(B-V) = 0.350$.

The absolute magnitude (Mabs) is then:

$$M_{\rm abs} = (K_{\rm 2MASS} - A_{Ks}) + 0.024 + 5 + 5\log_{10}(0.001\pi), \quad \text{(D.1)}$$

where +0.024 is the conversion to $K_{CIT/CTIO}$ and the parallax (π) has to be in arcsec (hence the 0.001)

This implicitly assumes that distance = 1/parallax which is only then calculated if the relative uncertainty of the parallax is better than 15%.

Then the bolometric magnitude (Mbol) and luminosity of the star relative to the Sun $\log(L_*/L_\odot)$ are:

$$M_{\rm bol} = M_{\rm abs} + {\rm BC} \quad \text{(D.2)}$$

$$\log(L_*/L_\odot) = -0.4\,(M_{\rm bol} - 4.75), \quad \text{(D.3)}$$

where 4.75 is the bolometric magnitude of the Sun.

And finally:

$$\log g = 4.44 + 4\log_{10}(T_{\rm eff}/5771) - \log_{10}(L_*/L_\odot) + \log_{10}(M_*/M_\odot). \quad \text{(D.4)}$$

The stellar masses were then estimated using the UniDAM code[2] (Mints & Hekker 2017). It interpolates masses from PARSEC isochrones (Bressan et al. 2012) using a Bayesian scheme. A first estimate of mass was computed with this code using the spectroscopic parameters ($T_{\rm eff}$, $\log g$, [Fe/H]), 2MASS magnitudes, parallaxes, and extinction.

With this first mass estimate, we compute a first estimate of $\log g$ using Eq. (D.4). The new $\log g$ values are then given again to UniDAM, to recompute the mass estimates. These iterations were repeated (a total of four iterations was sufficient) until the estimated mass was consistent with the estimated $\log g$.

UniDAM gives an estimate of the error of the mass, and this was also used in the computation of the total error budget in $\log g$. Uncertainties are from 10 000 Monte Carlo simulations, assuming Gaussian uncertainties in π, $K_{\rm 2MASS}$, stellar mass (with error coming from UniDAM), and ±0.02 mag for the bolometric correction. No uncertainty was assumed in $E(B-V)$, nor for $T_{\rm eff\odot}$, or $\log g_\odot$.

[2] See http://www2.mps.mpg.de/homes/mints/unidam.html